

Wearable Antennas and Systems

Guest Editors: Paul R. Young, C. K. Aanandan,
Thomaskutty Mathew, and Deepti Das Krishna





Wearable Antennas and Systems

International Journal of Antennas and Propagation

Wearable Antennas and Systems

Guest Editors: Paul R. Young, C. K. Aanandan,
Thomaskutty Mathew, and Deepti Das Krishna



Copyright © 2012 Hindawi Publishing Corporation. All rights reserved.

This is a special issue published in “International Journal of Antennas and Propagation.” All articles are open access articles distributed under the Creative Commons Attribution License, which permits unrestricted use, distribution, and reproduction in any medium, provided the original work is properly cited.

Editorial Board

M. Ali, USA
Charles Bunting, USA
Felipe Catedra, Spain
Dau-Chyrh Chang, Taiwan
Deb Chatterjee, USA
Z. N. Chen, Singapore
Michael Yan Wah Chia, Singapore
Christos Christodoulou, USA
Shyh-Jong Chung, Taiwan
Lorenzo Crocco, Italy
Tayeb A. Denidni, Canada
Antonije R. Djordjevic, Serbia
Karu P. Esselle, Australia
Francisco Falcone, Spain
Miguel Ferrando, Spain
Vincenzo Galdi, Italy
Wei Hong, China
Hon Tat Hui, Singapore
Tamer S. Ibrahim, USA
Nemai Karmakar, Australia

Se-Yun Kim, Republic of Korea
Ahmed A. Kishk, Canada
Tribikram Kundu, USA
Byungje Lee, Republic of Korea
Ju-Hong Lee, Taiwan
L. Li, Singapore
Yilong Lu, Singapore
Atsushi Mase, Japan
Andrea Massa, Italy
Giuseppe Mazarella, Italy
Derek McNamara, Canada
C. F. Mecklenbräuker, Austria
Michele Midrio, Italy
Mark Mirotznik, USA
Ananda S. Mohan, Australia
P. Mohanan, India
Pavel Nikitin, USA
A. D. Panagopoulos, Greece
Matteo Pastorino, Italy
Massimiliano Pieraccini, Italy

Sadasiva M. Rao, USA
Sembiam R. Rengarajan, USA
Ahmad Safaai-Jazi, USA
Safieddin Safavi-Naeini, Canada
Magdalena Salazar-Palma, Spain
Stefano Selleri, Italy
Krishnasamy T. Selvan, India
Zhongxiang Q. Shen, Singapore
John J. Shynk, USA
Mandeep S. Jit Singh, Malaysia
Seong-Youp Suh, USA
Parveen Wahid, USA
Yuanxun Ethan Wang, USA
Daniel S. Weile, USA
Quan Xue, Hong Kong
Tat Soon Yeo, Singapore
Young Joong Yoon, Korea
Wenhua Yu, USA
Jong Won Yu, Republic of Korea
Anping Zhao, China

Contents

Wearable Antennas and Systems, Paul R. Young, C. K. Aanandan, Thomaskutty Mathew, and Deepti Das Krishna

Volume 2012, Article ID 573202, 2 pages

Effect of Earth Ground and Environment on Body-Centric Communications in the MHz Band,

Katsuyuki Fujii and Yasuyuki Okumura

Volume 2012, Article ID 243191, 10 pages

Metamaterial Embedded Wearable Rectangular Microstrip Patch Antenna, J. G. Joshi, Shyam S. Pattnaik, and S. Devi

Volume 2012, Article ID 974315, 9 pages

Improved Successive Interference Cancellation for MIMO/UWB-Based Wireless Body Area Network,

M. Jayasheela and A. Rajeswari

Volume 2012, Article ID 781434, 9 pages

Design of a Wearable, Low-Cost, Through-Wall Doppler Radar System, Sam Agneessens,

Patrick Van Torre, Frederick Declercq, Bart Spinnewyn, Gert-Jan Stockman, Hendrik Rogier, and Dries Vande Ginste

Volume 2012, Article ID 840924, 9 pages

Performance of Ultrawideband Wireless Tags for On-Body Radio Channel Characterisation,

Mohammad Monirujjaman Khan, Qammer H. Abbasi, Akram Alomainy, and Yang Hao

Volume 2012, Article ID 232564, 10 pages

Analysis of Circular Polarization of Cylindrically Bent Microstrip Antennas, Tiiti Kellomäki

Volume 2012, Article ID 858031, 8 pages

Editorial

Wearable Antennas and Systems

Paul R. Young,¹ C. K. Aanandan,² Thomaskutty Mathew,³ and Deepti Das Krishna⁴

¹ School of Engineering and Digital Arts, University of Kent, Canterbury, Kent CT2 7NT, UK

² Department of Electronics, Cochin University of Science and Technology, Cochin, India

³ Department of Electronics, University College of Applied Sciences, Mahatma Gandhi University Regional Centre, Edappally, Cochin, India

⁴ Department of Electronics and Communication Engineering, Rajagiri School of Engineering Technology, Cochin, India

Correspondence should be addressed to Paul R. Young, p.r.young@kent.ac.uk

Received 26 November 2012; Accepted 26 November 2012

Copyright © 2012 Paul R. Young et al. This is an open access article distributed under the Creative Commons Attribution License, which permits unrestricted use, distribution, and reproduction in any medium, provided the original work is properly cited.

The topic of wearable antennas and body-centric communication systems has received a great deal of interest over the past few years with many applications in health care and sports science being proposed. These applications have included body area networks (BAN), where an array of devices or sensors, distributed across the body, communicate wirelessly to a body-mounted central hub, to be routed to an off body receiver for medical or sports monitoring. Other applications include RFID tags mounted on body that can be detected, wirelessly, for health care or security monitoring systems.

Naively, one may imagine that these systems are merely developmental with no need for further research; however, there are a number of challenges that engineers face in designing antennas and communication systems on body that are not present in a conventional system. Firstly, in body-centric systems, the antenna is necessarily mounted in close proximity to human tissue. Human tissue has a large dielectric constant compared to conventional RF substrate materials and a significant conductivity; as such, the body can have a great effect on an antenna's characteristics. This problem is compounded by the need to mount the antenna on a textile substrate, as part of an everyday garment, with the associated problems in maintaining the antenna's performance when the fabric is flexed or bent. For on-body networks, where communication between devices is necessary, the effect the body has on the channel must be characterised. This is particularly challenging due to the variability in human body shape and the dynamic nature of the channel—with movement of the body greatly affecting the channel characteristics, blocking, and scattering the signal in a complicated manner.

A large number of submissions were received for this special issue and the papers with relevant technical content were selected after review by experts. Brief synopses of some of the selected papers are given below.

“Effect of earth ground and environment on body-centric communications in the MHz band,” by K. Fujii and Y. Okumura, studies the effect the physical ground has on a body centric system. The authors model the human body shunted to earth ground in a radio anechoic chamber to analyze the electric field strength around it and clarify the effect of earth ground during BAN run time. The results suggest that earth ground has little influence on the human body and wearable devices. Only when the human body is directly grounded, the electric field near the feet area will decrease. The input impedance of the transmitter is approximately the same, and the received open-circuit voltage and current of the receiver are also the same. In addition, the authors also suggest that stable communications can be established by developing a closed circuit using earth ground as return path.

The problems of antennas on textile substrates are addressed in *“Metamaterial embedded wearable rectangular microstrip patch antenna,”* by J. G. Joshi, S. S. Pattnaik, and S. Devi. Here, the authors propose a modified patch antenna embedded with a metamaterial square SRR, on a fabric substrate, that maintains its characteristics even when flexed. The bending effect on the performance of wearable antenna is shown to be reduced by making slots in the radiating patch but it leads to mismatching at the desired lower resonance frequency. The authors report that embedding a metamaterial SRR is an advantageous approach to obtain better impedance matching at the desired resonant frequency

as this SRR introduces additional inductance, capacitance, and mutual inductance to match the impedance at the required frequency.

The topic of ultrawideband (UWB) communications on body is studied in “*Improved successive interference cancellation for MIMO/UWB-based wireless body area network*,” by M. Jayasheela and A. Rajeswari where cancellation schemes to improve the problems of interference in BANs are presented. An improved successive interference cancellation scheme for MIMO/UWB-based wireless body area network is proposed here. To mitigate interdevice interference in body area network successive interference cancellation with optimal ordering is used. TH PPM modulation followed by MMSE equalization is employed in this paper.

Applications of on-body systems are covered in “*Design of a wearable, low-cost, through-wall Doppler radar system*,” by S. Agneessens, P. V. Torre, F. Declercq, B. Spinnewyn, G.-J. Stockman, H. Rogier, and D. V. Ginste. In this paper, an on-body radar system is presented with applications for motion detection in difficult terrains and disaster areas. The system operates at 2.35 GHz and is integrable into garments. The main individual components of the radar system, that is, the transmit array and active receive antenna, as well as the system itself, have been reported to be thoroughly tested, validating the proposed design.

“*Performance of ultrawideband wireless tags for on-body radio channel characterisation*,” by M. M. Khan, Q. H. Abbasi, A. Alomainy, and Y. Hao studies path loss models for UWB on body channels. Experimental characterisation of an on-body radio channel for ultrawideband (UWB) wireless active tags is reported. UWB on-body radio propagation channel measurements are performed in the chamber and indoor environments. Nine different UWB on-body radio channels are investigated for static and movement scenarios. Results demonstrate that lognormal distribution provides the best fits for on-body propagation channels path loss model.

The effects that bending has on the polarisation and radiation pattern of a conventional patch antenna is covered in “*Analysis of circular polarization of cylindrically bent microstrip antennas*,” by T. Kellomäki. The authors present a simplified model of a bent circularly polarised patch antenna and predict the frequency shift of the axial ratio band. Uncontrolled bending is a problem associated especially with flexible textile antennas, so the authors present some guidelines for wearable antenna design and its placement as well.

It is hoped that this special issue goes some way in addressing the challenges associated with wearable antennas and systems, adding to the state-of-the-art in this exciting field.

*Paul R. Young
C. K. Aanandan
Thomaskutty Mathew
Deepti Das Krishna*

Research Article

Effect of Earth Ground and Environment on Body-Centric Communications in the MHz Band

Katsuyuki Fujii and Yasuyuki Okumura

Faculty of Information Sciences and Engineering, Nanzan University, 27 Seirei-cho, Aichi, Seto 489-0863, Japan

Correspondence should be addressed to Katsuyuki Fujii, fujii@sd.nanzan-u.ac.jp

Received 27 February 2012; Revised 9 August 2012; Accepted 14 August 2012

Academic Editor: Deepti Das Krishna

Copyright © 2012 K. Fujii and Y. Okumura. This is an open access article distributed under the Creative Commons Attribution License, which permits unrestricted use, distribution, and reproduction in any medium, provided the original work is properly cited.

Body area network (BAN) research, which uses the human body as a transmission channel, has recently attracted considerable attention globally. Zimmerman first advocated the idea in 1995. Illustrations of the electric field streamlines around the human body and wearable devices with electrodes were drawn. In the pictures, the electrodes of the wearable devices constitute a closed circuit with the human body and the earth ground. However, analysis of the circuit has not been conducted. In this study, we model the human body shunted to earth ground in a radio anechoic chamber to analyze the electric field strength around it and clarify the effect of earth ground during BAN run time. The results suggest that earth ground has little influence on the human body and wearable devices. Only when the human body is directly grounded, the electric field near the feet area will decrease. The input impedance of the transmitter is approximately the same, and the received open-circuit voltage and current of the receiver are also the same. In addition, we elucidate that stable communications can be established by developing a closed circuit using earth ground as return path. When the external electronic devices and human body are shunted to earth ground, the received open-circuit voltage and current increase.

1. Introduction

Research in wearable computing, which can always exchange information anywhere, has been actively pursued in recent years. For example, Zimmerman advocated the use of the human body as a transmission path [1, 2]. When a user wearing a transmitter with an electrode touches a receiver, a personal area network (PAN), which consists of the human body as the transmission path, is built. By transforming the human body into a transmission channel, transmission lines and communication need not occur during our daily activities. Moreover, it is unnecessary to establish a line of sight such as an IrDA, and energy consumption may be lower than that needed for wireless communications. Research on wearable devices is being performed by various organizations all over the world, and the expectations for utilization are growing. For example, the first technical textbook about BAN was published by Hall and Hao in 2006 [3]. Moreover, the second edition, which includes the latest research trends, was published in May 2012 [4]. In 2007, a task group for

wireless personal area network (WPAN) was organized by IEEE [5], and, in 2009, the first special issue regarding this research field was published by IEEE [6]. In Japan, medical information and communications technology (MICT) is an active field [7]. In addition, medical applications that can receive health-monitoring information of humans are becoming important in an aging society.

The WPAN carrier frequency is different for each application. It is divided into two domains: (1) antenna propagation [10–12] and (2) electrostatic coupling [1, 2]. We have modeled the wearable devices attached to the human body as shown in Figure 1 and studied the transmission mechanisms of wearable devices using the human body as the transmission channel from the viewpoint of the interaction between the body and electromagnetic fields [8]. Furthermore, although the model analysis using the whole body has been conducted, the difference in the transmission characteristics which depends on the coupling between the human body and the earth ground has been unsolved. In near future, with the spread of wearable devices for WPAN,

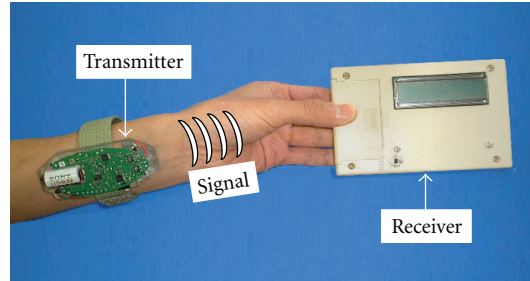


FIGURE 1: Transmission system using the human body as a transmission channel [8].

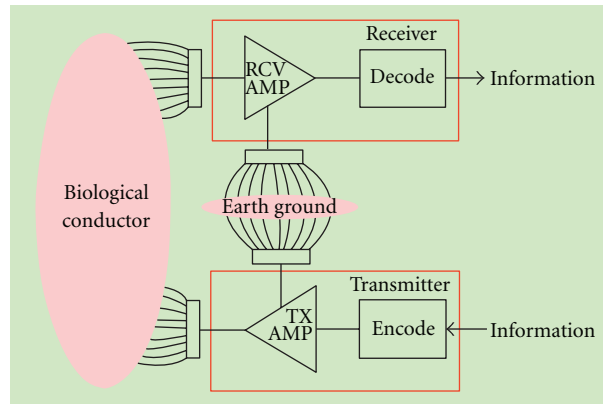


FIGURE 2: Electric field stream line model of PAN [1, 2].

wearable devices may be found almost everywhere on the human body, and they will exchange the data. To acquire a design guide in that case, it is necessary to understand how a signal is distributed over the whole body and how transmission characteristics change as a function of the environment.

2. Earth Ground and Transmission Characteristics

2.1. Analysis Model. In Zimmerman's studies [1, 2], there is coupling between earth ground and a biological conductor, as shown in Figure 2. However, few physical mechanisms that focus on ground have been explored until recently [9]. In this section, we model the human body with wearable devices in contact with earth ground in a radio anechoic chamber and report the effect of earth ground. Figure 3 shows the standard-posture model that has been simplified by dividing the body into legs, body, arms, shoulders, and head. Then, each part is modeled as a rectangular parallelepiped [9]. At 10 MHz, relative permittivity ($\epsilon_r = 170.73$) and conductivity ($\sigma = 0.62 \text{ S/m}$) are equal to the human muscle [13]. The size of the simplified body model is adapted from Japanese male and female averages, obtained from the statistical data [14].

The radio anechoic chamber at Chiba University is $7230 \times 5730 \times 2930 \text{ mm}^3$ in size, and it has a 70 mm thick concrete base ($\epsilon_r = 3.8$, $\sigma = 6.67 \times 10^{-6} \text{ S/m}$, [15]) [16]. The absorber in the chamber is disregarded because we used 10 MHz sinusoidal waves that are not absorbed by the

absorber. Perfect electric conductor sheets cover the ceiling, walls, and base under the concrete.

Figure 4 shows the structure of the wearable transmitter and receiver. This transmitter consists of one signal electrode and one circuit board. The signal electrode outputs a sinusoidal wave ($3 \text{ V}_{\text{p-p}}$) of 10 MHz. To apply this transmitter to finite difference time domain (FDTD) method, the electrode and circuit board are modeled by using perfect electric conductor sheets, and the delta-gap voltage of the 10 MHz sinusoidal wave is fed between the signal electrode and the circuit board. The receiver has one receiving electrode and one circuit board. The received open-circuit voltage (OCV) is calculated from the electric field between the receiving electrode and circuit board. The grid spacing of the FDTD method is $\Delta x = \Delta y = \Delta z = 5 \text{ mm}$.

Figure 5 shows the calculation model of the human body in contact with earth ground with wearable devices in the radio anechoic chamber. The human body is in center of the chamber, and a perfect electric conductor sheet of $3000 \times 3000 \text{ mm}^2$ in size is placed under the legs.

Figure 6 shows four patterns of the simplified human-body model by varying the contact with earth ground (perfect electric conductor sheet). Figure 6(a) shows the legs directly shunted to earth ground, Figure 6(b) simulates the case of wearing shoes with a 3 cm thick sole, Figure 6(c) shows the far distance from the legs to ground (40 cm), and Figure 6(d) is for the free space case, in which the human body is not coupled to the surroundings. By using these calculation models, electric field distribution, OCV,

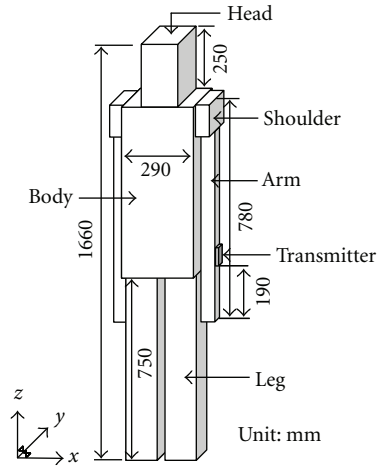


FIGURE 3: Simplified whole human body model [9].

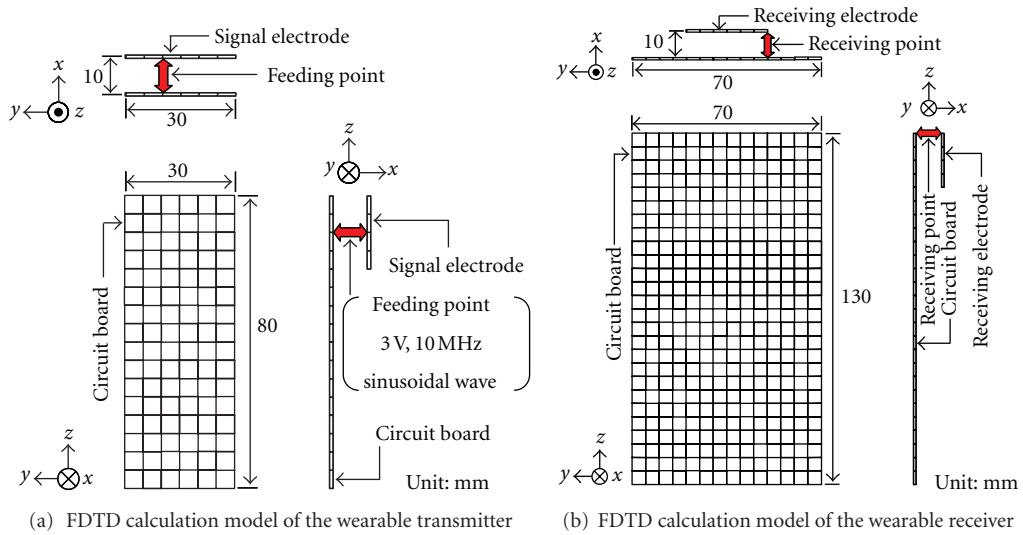


FIGURE 4: Structure of the wearable transmitter and receiver [8].

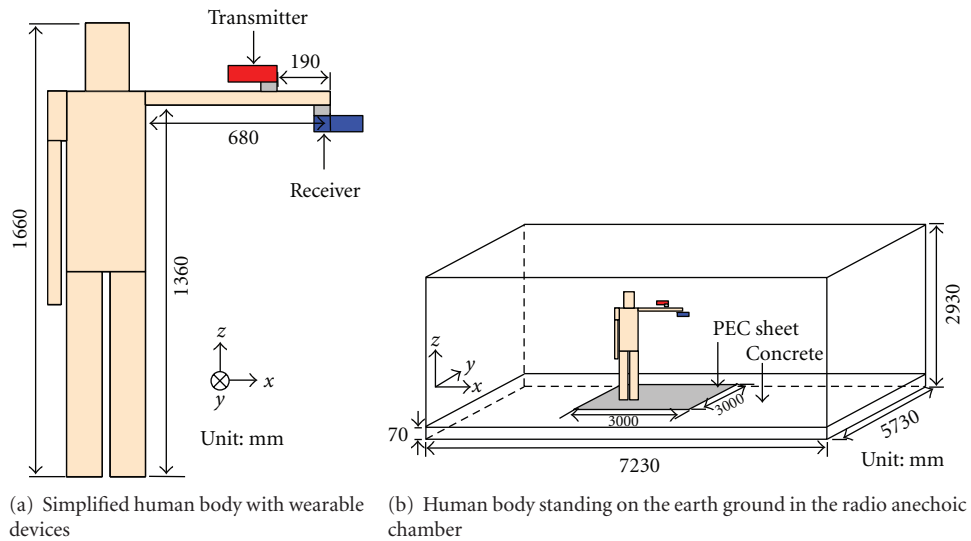


FIGURE 5: FDTD calculation model.

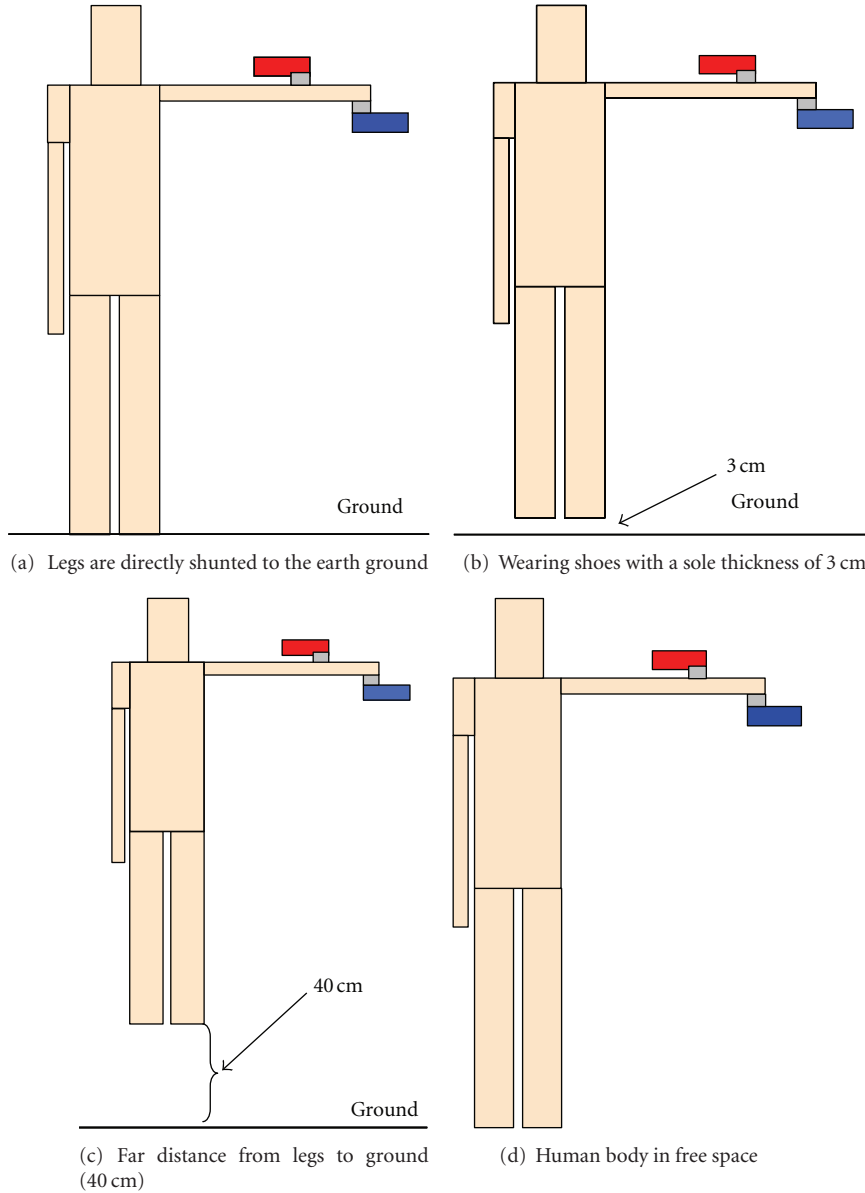


FIGURE 6: Verification models for the influence of the earth ground.

TABLE 1: Input power and input impedance of the transmitter.

Model name	Input power (W)	Impedance (Ω)	
		Real	Imaginary
Ground	1.47×10^{-6}	20.9	-2825.6
3 cm up	1.43×10^{-6}	20.4	-2826.1
40 cm up	1.43×10^{-6}	20.2	-2826.2
Free space	1.43×10^{-6}	20.4	-2826.2

and the receiver current are discussed considering the effect of earth ground in the radio anechoic chamber.

2.2. Calculation Results and Discussion. The results of the electric field distribution shown in Figures 7(a)–7(d) verify

TABLE 2: OCV and current of the receiver.

Model name	OCV (mV)	J (nA)
Ground	9.19	72.1
3 cm up	9.26	73.1
40 cm up	9.48	74.4
Free space	9.55	75.1

the influence of the earth ground. These figures illustrate the human body directly shunted to the earth ground, 3 cm above ground, 40 cm above ground, and in free space, respectively. It is evident that most of the electric field is distributed around the transmitter and along the arm. However, since the single-electrode structure of the transmitter was adopted, the radiation (leakage) in the air

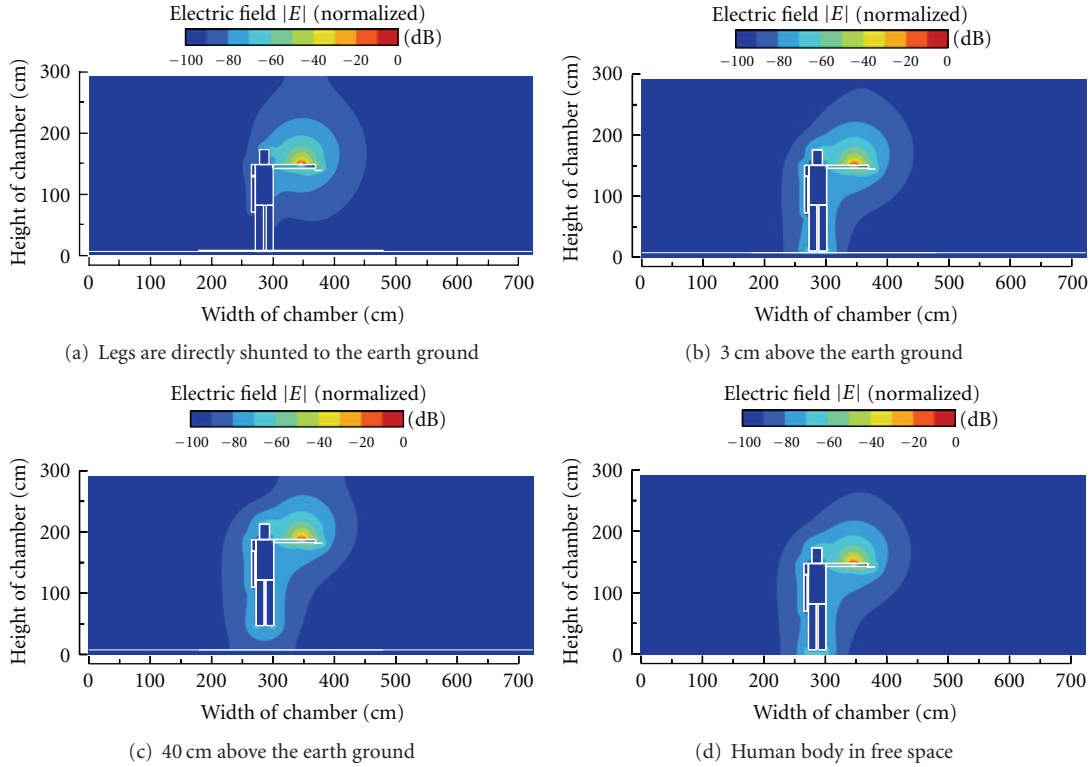


FIGURE 7: Electric field distribution around the human body.

TABLE 3: Input power and input impedance of the transmitter.

Model name	Input power (W)	Impedance (Ω)	
		Real	Imaginary
A. table w/leg	1.03×10^{-2}	53.5	-7.9
A. table w/o leg	1.02×10^{-2}	53.8	-7.7
w/o table	1.02×10^{-2}	53.9	-7.5
Free space	1.02×10^{-2}	53.9	-7.5
W. table w/leg	1.02×10^{-2}	53.9	-7.6
W. table w/o leg	1.02×10^{-2}	53.9	-7.6

TABLE 4: OCV and current of the receiver.

Model name	OCV (V)	J (μA)
A. table w/leg	0.63	4.92
A. table w/o leg	0.43	3.40
w/o table	0.27	2.13
Free space	0.26	2.03
W. table w/leg	0.31	2.44
W. table w/o leg	0.31	2.41

was strong. In Figure 7(a), the critical point is that the electric field strength decreases significantly around the leg region. It is assumed that existence of the earth ground prevents the electric field from the foot area. However, in the domain of the upper half of the body, there is no difference compared with other models. Moreover, from Figures 7(b) and 7(c), if the human body floats in the air, coverage of the electric

field improves. These results show that when BAN devices are attached to the legs, the situation in which the legs are not directly shunted to the earth ground is effective.

Consideration for each vector component of the electric field is as follows. The electric field component perpendicular to the body surface is dominant. The human body acts as a conductor at 10 MHz because the loss tangent of the muscle is approximately 6.5. Therefore, while developing BAN devices, antennas designed to receive the perpendicular component of the electric field are required.

Table 1 shows input power and input impedance of the transmitter. It can be observed that input power is small because the one-electrode structure strengthens the capacitance of the input impedance. However, even if the contact conditions with the earth ground change, the values of Table 1 remain constant. Table 2 shows the received OCV [mV] and current J [nA] of the receiver of each model. The strength remains constant because of the earth ground. From these results, it can be concluded that there is no coupling with earth ground. Therefore, only when the human body is directly grounded, the electric field near the feet area decreases.

3. Considering the Closed-Circuit Model through Earth Ground

3.1. Calculation Models. In this section, a closed-circuit model through earth ground is considered. This means having BAN communication with an external electronic device

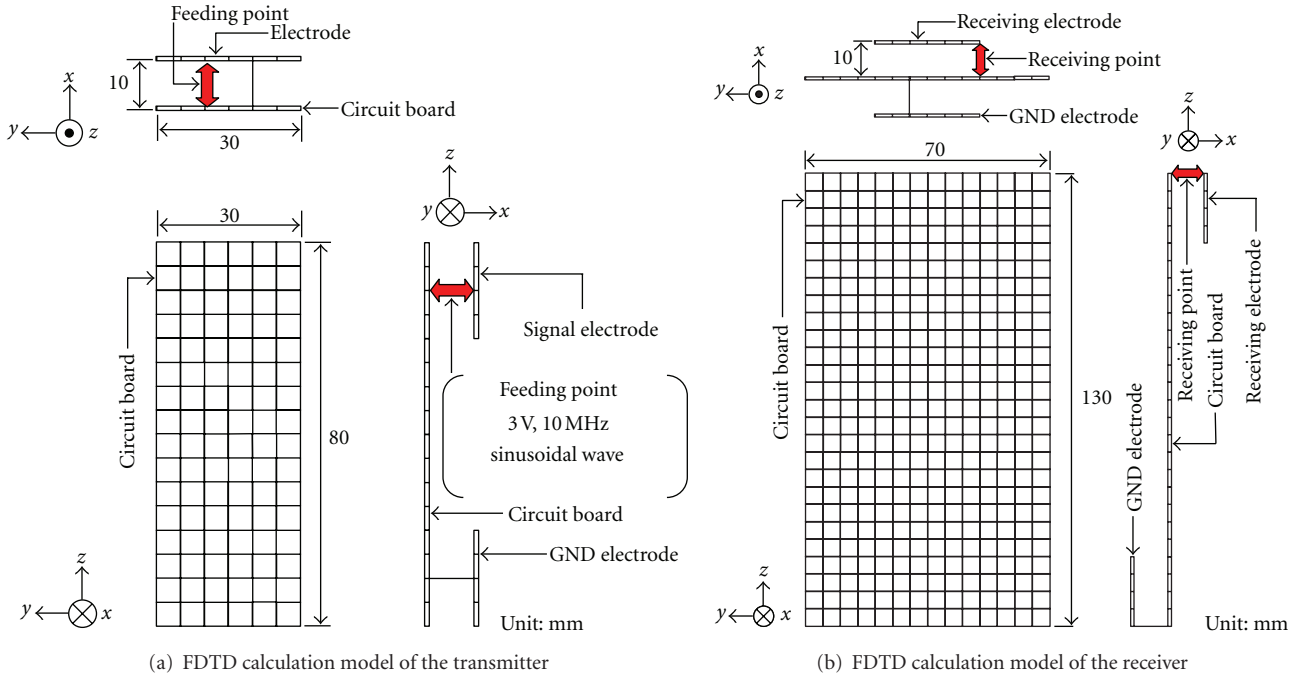


FIGURE 8: FDTD calculation model of the transmitter and receiver.

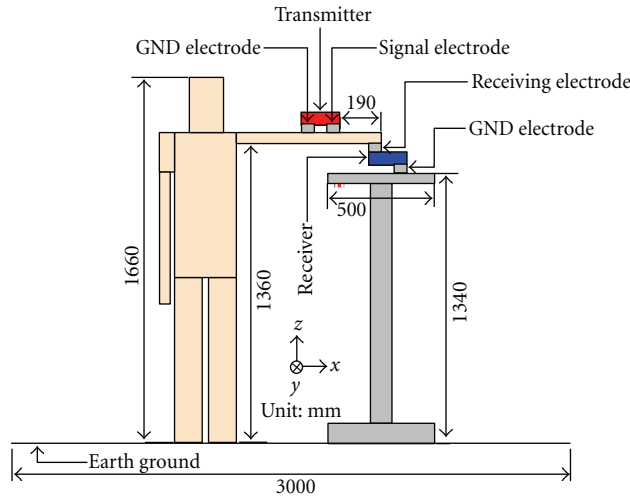


FIGURE 9: Calculation model of developing a closed circuit through the earth ground.

that is shunted to the stable earth ground level. Figure 8 shows FDTD calculation models of the wearable transmitter and receiver. The electrode structure is changed to establish a closed circuit through the earth ground. The transmitter has two electrodes [8]. One is a signal electrode, which feeds a 10 MHz sinusoidal wave ($3 V_{p-p}$), and the other one is the ground (GND) electrode, which is shunted to the ground level of the transmitter. In addition, the receiver has two electrodes. One is the receiving electrode, and the other one is the GND electrode, which can be shunted to the earth ground.

Figure 9 shows the calculation model of developing the closed circuit through the earth ground. This figure is simply drawn so that the electrode structures, position,

and environment are easily understood. The arm is lifted horizontally, similar to Section 2. The signal electrode is in contact at 190 mm from the fingertip. The receiving electrode is arranged under the fingertip. Moreover, to imitate an external device shunted to the earth ground, an aluminum table is modeled forming a current path to the earth ground.

In Figure 10, six types of situations are shown to clarify the effect of establishing a closed-circuit path through the earth ground. Each red line indicates the current path. In Figure 10(a), a tight circuit is formed by using an aluminum table ($\epsilon_r = 1.00$, $\sigma = 3.82 \times 10^7$ S/m, [17]) shunted to the earth ground. Figure 10(b) shows the aluminum table without leg that interrupts the current path through the earth

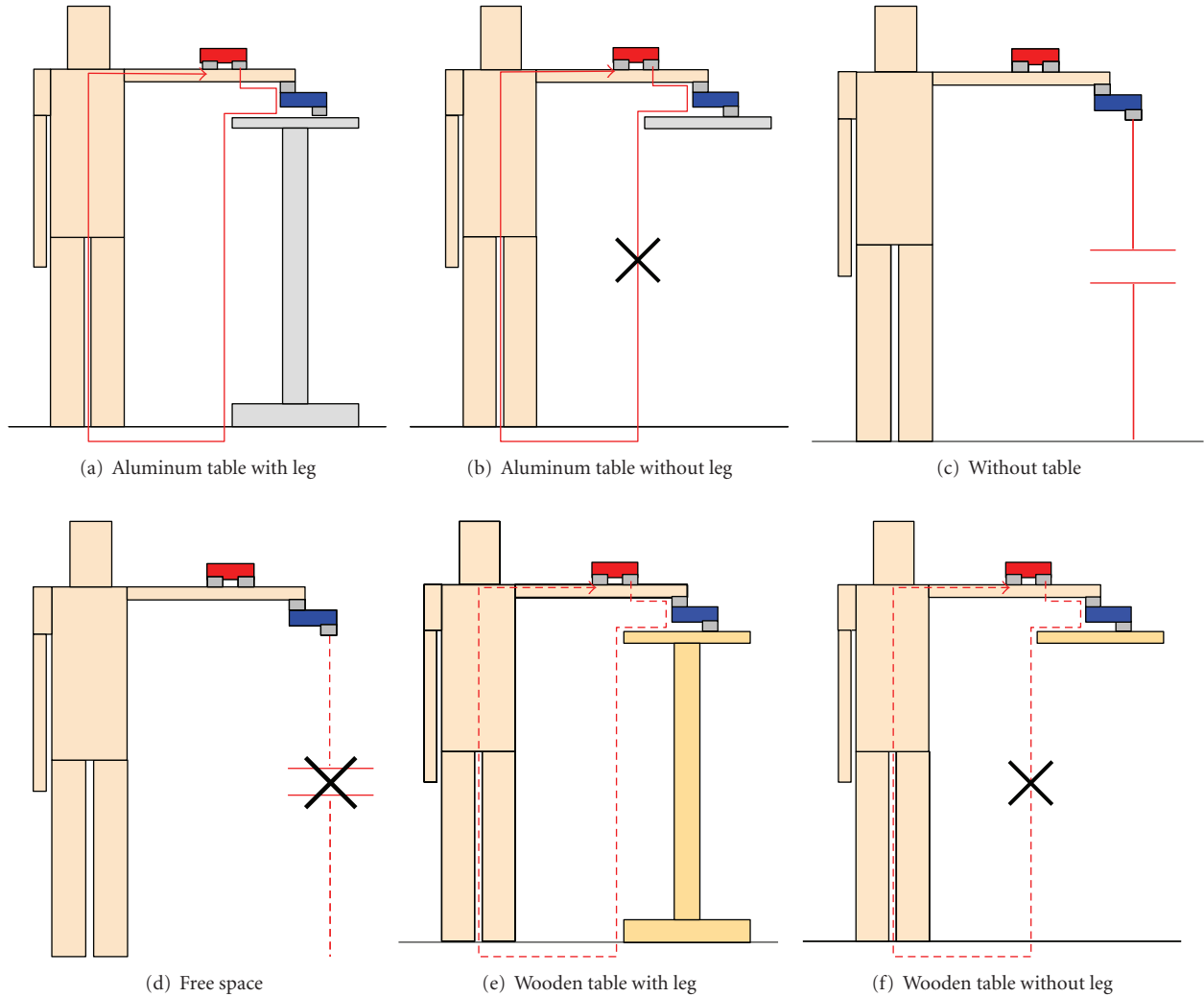


FIGURE 10: Analysis models for the effect of current loop path.

ground. Figure 10(c) shows the model that interrupts the circuit, so there is no influence of the surface of the aluminum table. Figure 10(d) shows the human body with wearable devices floating in free space. Therefore, the body is not influenced by the surroundings. Moreover, Figures 10(e) and 10(f) show the results of the analysis performed for a wooden table ($\epsilon_r = 2.75$, $\sigma = 1.53 \times 10^{-5}$ S/m [17]) to clarify loose coupling.

3.2. Calculation Results and Discussion. In this section, we discuss the calculation results for the electric field strength, received OCV, and received current. All electric-field-strength data shown in Figure 11 are normalized to the electric field at the feeding gap. The electric field of each model is distributed along the human body. These tendencies are relatively similar to the results of Section 2. Besides, the input power and input impedance of the transmitter of each model in Table 3 are similar because GND electrode of the transmitter contributes to impedance matching [8]. Thus, the transmitter grounded to the human body is not influenced by the surroundings.

One of the notable features of electric field distribution is that the strength between the arms and the aluminum table with leg (shunted to the earth ground) is the greatest. The electric field concentration is due to the existence of large aluminum table with high conductivity and the return path of the current through the earth ground. This is the highest received OCV in Table 4. Furthermore, we can evaluate the validity of the closed-circuit model of Figure 2 by comparing the case between the aluminum table with legs and without legs.

The received OCV and current of the receiver in Table 4 suggest that it is advantageous to use the earth ground as a return path. When the return path is set, a stable connection can be constructed.

As a result, external BAN communication and wearable devices on the human body must share a stable earth ground connection to form the closed circuit, thereby allowing increased current flow to BAN area.

3.3. Measurement Results. In this section, we discuss the measurements of the received OCV from the receiver

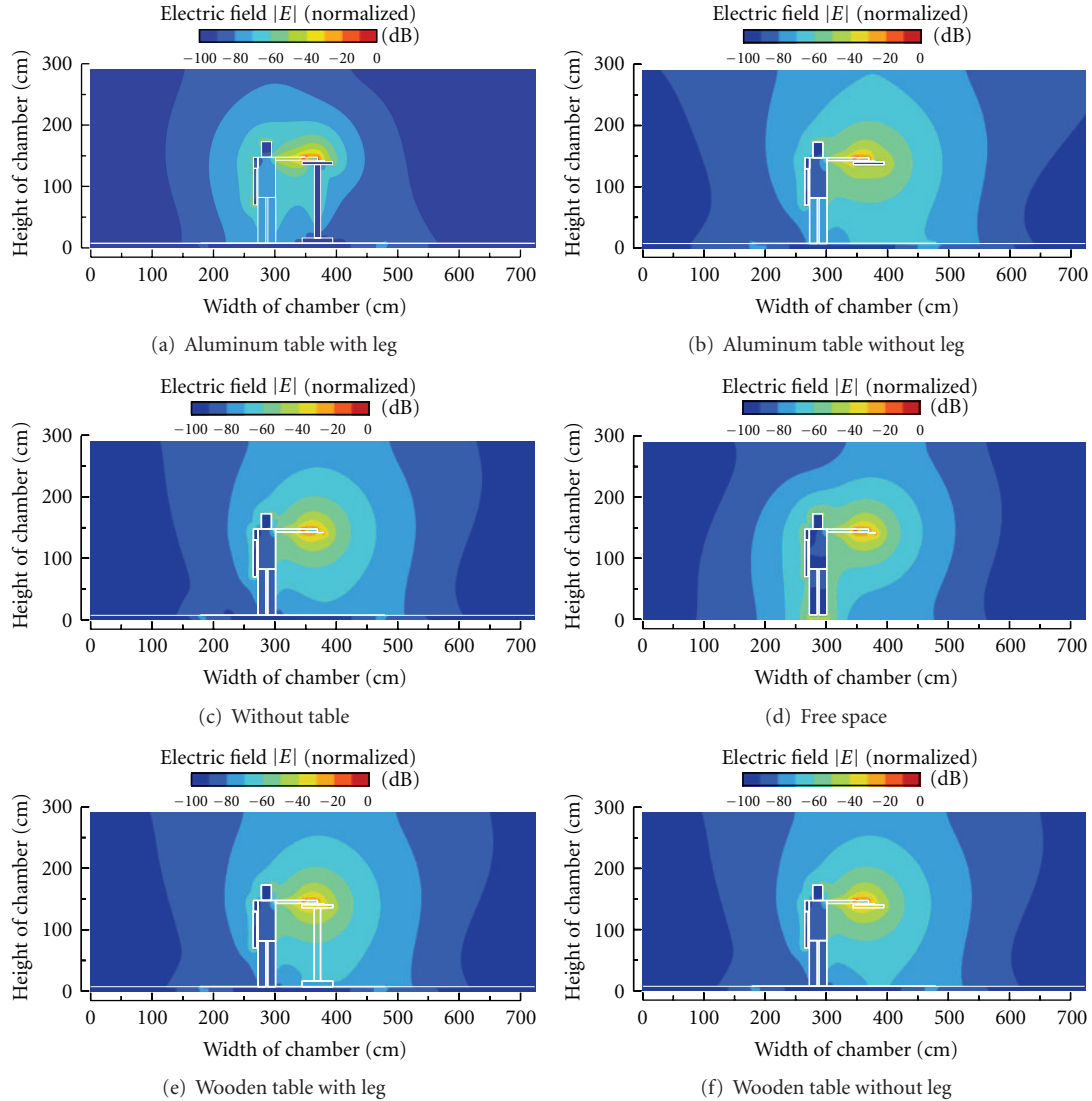


FIGURE 11: Electric field distribution.

to show the validity of the calculations. Figure 12 shows the measurement conditions. (Figure 12(a): aluminum table with leg, Figure 12(b): aluminum table without leg, Figure 12(c): without table, Figure 12(d): wooden table with leg, and Figure 12(e): wooden table without leg). The absorbers in the chamber are removed, and an aluminum plate, which imitates the earth ground, is set on the floor of the chamber with an area of $3000 \times 3000 \text{ mm}^2$. The electrode structures of the wearable transmitter and receiver are same as that of Figure 8. In the measurements, the feet of the human subject with the wearable devices are bare to directly shunt the body to the earth ground. The size of the subject is approximately the same as that of the calculation model based on the statistical data [14]. The measurement methods of reading the received OCV were severely restricted because the subject must maintain the same position during BAN run time. Thus, the measurements were obtained by another person that read the received OCV. In addition, the

observer stood on styrene foam to avoid contact with the earth ground. Therefore, the voltage fluctuation due to the existence of the observer can be neglected.

Figure 13 shows the fluctuations in OCV in each environment. The values are normalized to the case of the “w/o table” model. As the diagram indicates, the measurements agree with the calculations. The results clearly show that the received OCV fluctuates between 96% and 233% as a function of the environment. When the closed circuit through the earth ground is constructed, the received OCV becomes stronger. Therefore, it is possibly reasonable to conclude that developing a closed circuit is advantageous for stable communication in BAN.

4. Conclusions

In this study, the effect of earth ground on transmission is analyzed by using a simplified model of the human body

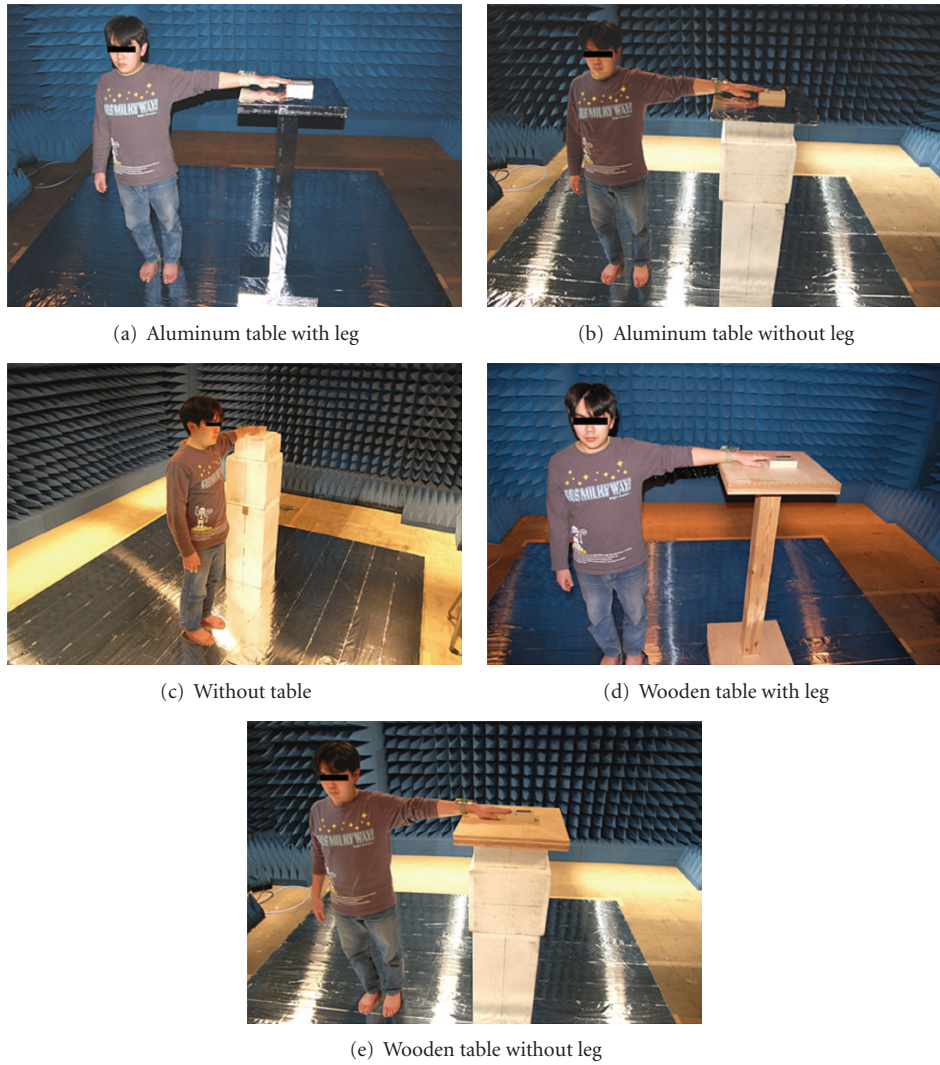


FIGURE 12: Measurement conditions.

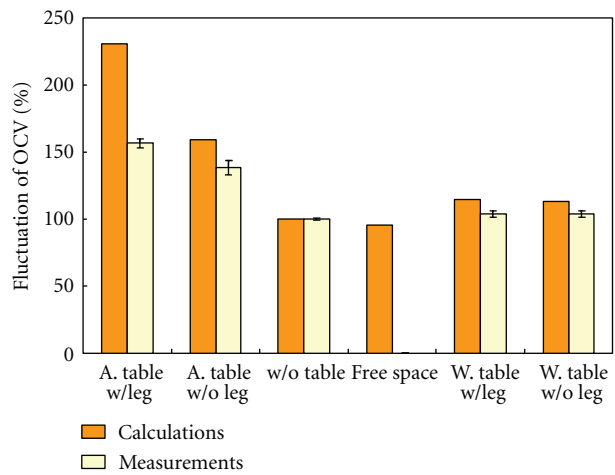


FIGURE 13: Fluctuations of OCV in each environment.

in contact with the earth ground with wearable devices in a radio anechoic chamber. The results are divided into two parts.

- (1) The effect of earth ground on the wearable devices when there is no connection to ground.
- (2) The effect on transmission when the human body, wearable devices, and the earth ground form a closed circuit.

In (1), four patterns of transmission were constructed. As a result, the input impedance of the transmitter is approximately the same, and the received OCV and current of the receiver at the fingertip are also the same. Thus, there is no effect on the signal of the transmission due to the earth ground coupling. Only when the human body is directly shunted to the earth ground, the electric field strength around the leg region weakens. In addition, when a human (whose body is considered) wears shoes (that means not directly shunted to the earth ground), electric field reduction cannot be observed, and this is approximately the same as that in the free space case.

In (2), when the external devices and human body are shunted to the earth ground (forming a closed circuit), the received OCV and current increase. This is because the current flow uses the earth ground to increase the closed circuit. Apparently, for a stable connection, it is advantageous to have the external devices and human body shunted to the earth ground. Moreover, the validity of the calculations is proved by the experiments in the radio anechoic chamber with a human.

Acknowledgments

The authors would specifically like to thank Professor Koichi Ito of Chiba University for his continuing guidance and encouragement and also wish to thank Associate Professors Masaharu Takahashi and Kazuyuki Saito of Chiba University for their valuable guidance. This study was partly supported by Nanzan University Pache Research Subsidy I-A-2 for the 2012 academic year.

References

- [1] T. G. Zimmerman, *Personal Area Networks (PAN): near-field intra-body communication [M.S. thesis]*, MIT Media Laboratory, Cambridge, Mass, USA, 1995.
- [2] T. G. Zimmerman, "Personal area networks: near-field intra-body communication," *IBM Systems Journal*, vol. 35, no. 3-4, pp. 609-617, 1996.
- [3] P. S. Hall and Y. Hao, *Antennas and Propagation for Body-Centric Wireless Communications*, Artech House, 2006.
- [4] P. S. Hall and Y. Hao, *Antennas and Propagation for Body-Centric Wireless Communications*, Artech House, 2nd edition, 2012.
- [5] IEEE 802.15 WPAN Task Group 6, <http://www.ieee802.org/15/pub/TG6.html>.
- [6] P. Hall, Y. Hao, and K. Ito, "Antennas and propagation on body-centric wireless communications," *IEEE Transactions on Antennas and Propagation*, vol. 57, no. 4, pp. 834-836, 2009.
- [7] Technical Committee on Medical Information and Communication Technology (MICT), <http://www.ieice.org/~mict/>.
- [8] K. Fujii, M. Takahashi, and K. Ito, "Electric field distributions of wearable devices using the human body as a transmission channel," *IEEE Transactions on Antennas and Propagation*, vol. 55, no. 7, pp. 2080-2087, 2007.
- [9] K. Fujii, D. Ishide, M. Takahashi, and K. Ito, "Electric field distributions generated by a wearable device using simplified whole human body models," *Journal of the Institute of Image Information and Television Engineers*, vol. 62, no. 12, pp. 1980-1987, 2008.
- [10] S. L. Cotton and W. G. Scanlon, "Channel characterization for single- and multiple-antenna wearable systems used for indoor body-to-body communications," *IEEE Transactions on Antennas and Propagation*, vol. 57, no. 4, pp. 980-990, 2009.
- [11] I. Khan and P. S. Hall, "Multiple antenna reception at 5.8 and 10 GHz for body-centric wireless communication channels," *IEEE Transactions on Antennas and Propagation*, vol. 57, no. 1, pp. 248-255, 2009.
- [12] P. Van Torre, L. Vallozzi, C. Hertleer, H. Rogier, M. Moeneclaey, and J. Verhaevert, "Indoor Off-Body wireless MIMO communication with dual polarized textile antennas," *IEEE Transactions on Antennas and Propagation*, vol. 59, no. 2, pp. 631-642, 2011.
- [13] IFAC, <http://niremf.ifac.cnr.it/tissprop/>.
- [14] Report of National Institute of Bioscience and Human-Technology, "Human body dimensions data for ergonomic design," vol. 2, no. 1, 1994.
- [15] C. Cristina and A. Orlandi, "Equivalent transmission line model for electromagnetic penetration through reinforced concrete walls," *IEICE Transactions on Communications*, vol. 78, no. 2, pp. 218-229, 1995.
- [16] K. Fujii, K. Ito, and S. Tajima, "A study on the signal propagation of whole body model wearing transmitter using human body as a transmission channel," in *Proceedings of the ITE annual convention*, Tokyo, Japan, August 2003.
- [17] W. Hayt and J. Buck, *Engineering Electromagnetics*, McGraw-Hill, 2001.

Research Article

Metamaterial Embedded Wearable Rectangular Microstrip Patch Antenna

J. G. Joshi, Shyam S. Pattnaik, and S. Devi

National Institute of Technical Teachers' Training and Research, Sector 26, Chandigarh 160019, India

Correspondence should be addressed to J. G. Joshi, jayant100@hotmail.com

Received 30 March 2012; Revised 20 June 2012; Accepted 4 July 2012

Academic Editor: Deepti Das Krishna

Copyright © 2012 J. G. Joshi et al. This is an open access article distributed under the Creative Commons Attribution License, which permits unrestricted use, distribution, and reproduction in any medium, provided the original work is properly cited.

This paper presents an indigenous low-cost metamaterial embedded wearable rectangular microstrip patch antenna using polyester substrate for IEEE 802.11a WLAN applications. The proposed antenna resonates at 5.10 GHz with a bandwidth and gain of 97 MHz and 4.92 dBi, respectively. The electrical size of this antenna is $0.254\lambda \times 0.5\lambda$. The slots are cut in rectangular patch to reduce the bending effect. This leads to mismatch the impedance at WLAN frequency band; hence, a metamaterial square SRR is embedded inside the slot. A prototype antenna has been fabricated and tested, and the measured results are presented in this paper. The simulated and measured results of the proposed antenna are found to be in good agreement. The bending effect on the performance of this antenna is experimentally verified.

1. Introduction

Nowadays, handheld communication devices and body centric communication systems need high-gain compact antennas which should be an integral part of the wearer clothing [1–6]. These systems are wearable computers; flexible mobile phones; personal digital assistant (PDA) devices; public safety band systems; sports activities; body area networks (BAN); industrial, scientific, and medical (ISM) band; WLAN; Wi-Fi; Wi-max; Bluetooth; HYPER LAN; and so forth. The textile- or cloth-based wearable antenna should communicate the voice, data, or biotelemetry signals at high data rates. The wearable antenna should have features like light weight, conformal, need to be hidden, and it should not affect the health of user. In practice, synthetic or natural materials are used as substrate to manufacture the textile or cloth-based wearable antennas. These materials are cotton, liquid crystal polymer (LCP), fleece fabric, foam, Nomex, nylon, conducting ribbon, insulated wire, conducting paint, copper coated fabric, and so forth Hall et al. presented a study on the necessity of wearable antennas for personal area networks (PAN), BAN, and ISM band applications [1]. In the literature different types of wearable antennas have been reported [2–4]. The bending effect due to human

body movements on the impedance matching of textile-based rectangular microstrip patch antenna is investigated and analyzed [5].

It is desired to reduce the size of wearable antenna so that its performance should not be affected by the bending effect and minimum deposition of electromagnetic field in the human body. In spite of numerous advantages of microstrip patch antennas it is difficult to achieve a better trade off between the gain, bandwidth, and more prominently the size of antennas. Most recently, antenna researchers have verified and evidenced an innovative approach to overcome the limitations of microstrip patch antennas by using metamaterial [7–23]. In 1968, Veselago theoretically predicted that metamaterial possesses negative values of magnetic permeability (μ) and/or electric permittivity (ϵ) [17]. Metamaterial structure consists of split ring resonators (SRRs) to produce negative permeability and thin wire elements to generate negative permittivity. Metamaterial characteristics of different SRR structures have been studied and verified [7–23]. Metamaterial is used to load the microstrip patch antennas either by partially filling it beneath the substrate of patch or placing it as superstrate (metamaterial reflective surface) on the top of the patch [7–23]. These techniques significantly enhance the gain, bandwidth, directivity of the

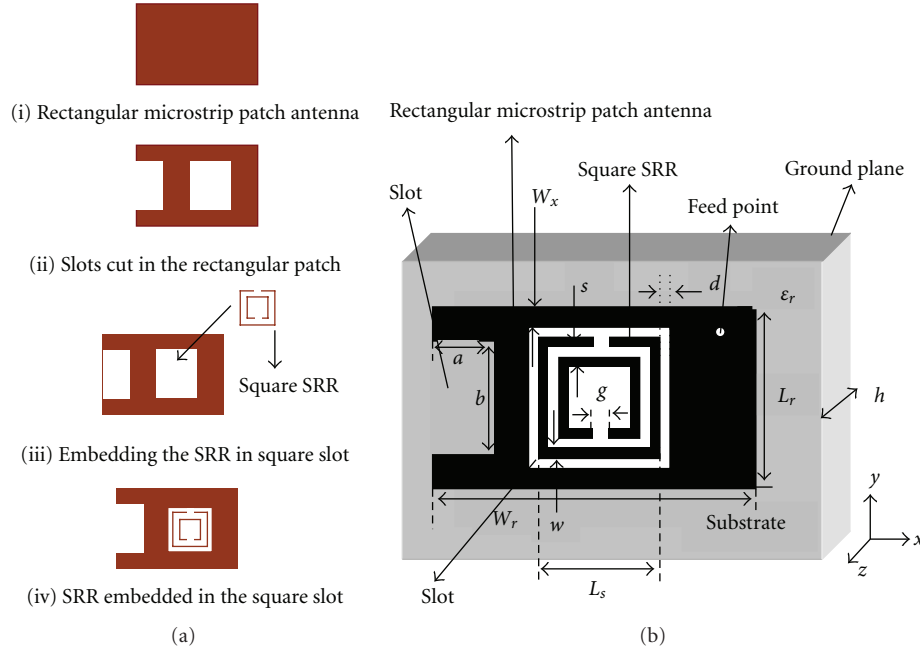


FIGURE 1: (a) Step-by-step design procedure. (b) Sketch and geometrical structure of metamaterial square SRR embedded wearable rectangular microstrip patch antenna.

microstrip patch antennas with considerable size reduction. Under loading condition, the microstrip patch antenna generates subwavelength resonances due to the modifications of the resonant modes [7–15, 22, 23]. The double negative (DNG) and single negative (SNG) metamaterial is used to load the microstrip patch antennas for size reduction by generating the subwavelength resonances [7, 8]. The effect of mutual inductance on the resonant frequency, bandwidth, gain, and size of metamaterial loaded electrically small microstrip patch antenna is reported in [12]. The specific absorption rate (SAR) can be reduced by placing metamaterial SRRs between the antenna and human muscles [16]. In their previous work, authors presented different techniques of loading the microstrip patch antennas using metamaterial to make them compact and simultaneously to enhance the gain as well as bandwidth [10, 12–15, 22, 23]. A high gain rectangular microstrip patch antenna for IEEE 802.11a WLAN applications is presented in [24]. The above mentioned literature study encouraged the authors to design the proposed wearable rectangular microstrip patch antenna.

The objective of this paper is to design and fabricate a polyester substrate-based metamaterial embedded rectangular microstrip patch antenna for WLAN applications. In this work, an attempt is made to remove the metal portion of the rectangular microstrip patch antenna by making the slots inside the patch to excite lower resonant frequency. The metal removing technique helps not only to reduce the bending effect due to human body movements on the antenna but also to reduce the SAR. The metamaterial square SRR is embedded inside the slot to achieve the better impedance matching in the WLAN band. The paper is organized into following sections. The detailed geometrical

structure, design, and fabrication processes of the proposed antenna are presented in Section 2. The simulated and measured results of the proposed antenna are presented, compared, and analyzed in Section 3. In Section 4, the bending effects on the performance of fabricated antenna are experimentally verified and presented. Finally, the paper is concluded in Section 5.

2. Antenna Design

This is a polyester substrate-based wearable antenna designed for IEEE 802.11a WLAN applications. Figure 1(a) depicts the step-by-step design procedure of the proposed wearable antenna. The antenna design is divided into three steps—(a) design and simulations of rectangular microstrip patch antenna, (b) making rectangular and square slots in the rectangular patch to excite the desired lower resonant frequency for size reduction, (c) embedding the designed metamaterial square SRR inside the square slot for better impedance matching at WLAN frequency band. In simulations, when the SRR is embedded inside the square slot of the patch, better matching is noticed at the resonance frequency 5.10 GHz. In simulations, it is observed that a small difference in the placement of square SRR shifts the resonance frequency with considerable changes in the matching conditions. Finally, the SRR is placed inside the square slot at the distance of $d = 1$ mm as shown in Figure 1(b). The square SRR is magnetically coupled with the slotted rectangular patch to form an LC resonator that resonates at 5.10 GHz by making the antenna compact. Figure 1(b) depicts the sketch and geometrical structure of metamaterial square SRR embedded wearable rectangular microstrip patch antenna.

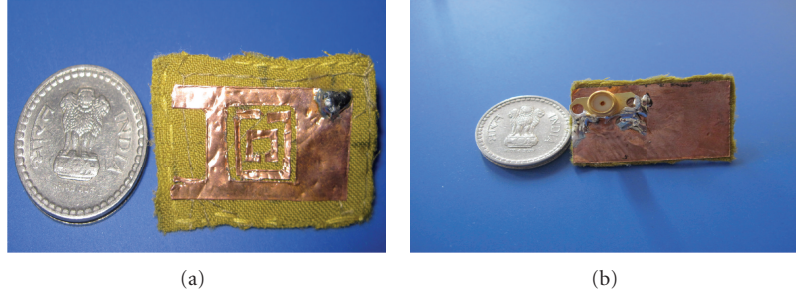


FIGURE 2: Photographs of the fabricated metamaterial square SRR embedded wearable rectangular microstrip patch antenna. (a) Radiating patch. (b) Ground plane.

Figures 2(a) and 2(b), respectively, depict the photographs of radiating patch and ground plane with SMA connector of the fabricated metamaterial SRR embedded wearable rectangular microstrip patch antenna. Initially, the rectangular microstrip patch antenna of length (L_r) is designed for resonant frequency 8.65 GHz using (1) [25, 26]:

$$L_r = \frac{c}{f_r \sqrt{\epsilon_e}}, \quad (1)$$

where, f_r is resonant frequency, c is velocity of light (3×10^8 m/sec), ϵ_r is relative permittivity (8.854×10^{-12} F/m), and ϵ_e is effective dielectric constant of the substrate which is calculated using (2):

$$\epsilon_e = \frac{(\epsilon_r + 1)}{2} + \frac{(\epsilon_r - 1)}{2} \left(1 + \frac{12h}{W}\right)^{-1/2}. \quad (2)$$

The dimensions of rectangular microstrip patch are length $L_r = 15$ mm and width $W_r = 30$ mm. The slots are cut in the rectangular microstrip patch to reduce the resonant frequency to WLAN applications as well as to reduce the metal area. Initially, a rectangular slot of dimensions $a = 6$ mm and $b = 8$ mm is cut inside the radiating edge of the rectangular microstrip patch but no better impedance matching is obtained. Hence, at the centre of rectangular patch a square slot of dimensions 10 mm \times 10 mm is created. Again the better matching could not be obtained in the WLAN frequency band. Further, to obtain the better impedance matching and to achieve a subwavelength resonance a metamaterial square SRR is embedded into the square slot to load this antenna. The geometrical dimensions of the square SRR as shown in Figure 1(b), width of split rings (w), separation between inner and outer split rings (s), and gap at the splits of rings (g), are set to $w = s = g = 1$ mm, respectively. The length of outer square split ring (L_s) is 9 mm. The distance between outer square SRR and the edge of cut on the rectangular microstrip patch is $d = 1$ mm. The equations (1) and (2) are used to design the rectangular microstrip patch antenna at resonance frequency 8.65 GHz without (i) making slots in the radiating patch and (ii) embedding the SRR inside the square slot. The designed antenna resonates at 8.48 GHz which is reduced to the working frequency 5.10 GHz by making the slots and embedding the SRR inside the slot. Due to slots the resonant

length of the designed rectangular patch is changed and poor matching is observed during the simulations at the working frequency. Further, the inductance and capacitance of SRR with the mutual induction between the antenna and SRR provide better matching at the working frequency 5.10 GHz.

The aspect ratio of rectangular microstrip patch, that is, length (L_r) to width (W_r) ratio, is 0.5. Similarly, the aspect ratio, of square slot is 1. The aspect ratio of rectangular slot, that is, length “ a ” to width “ b ”, is set to 0.75 which is to one-half of the sum of aspect ratios of the rectangular patch and the slot. The antenna is coaxially fed by a 50Ω SMA connector at $x = 11$ mm and $y = 7$ mm. The polyester cloth substrate of thickness $h = 1$ mm, relative permittivity $\epsilon_r = 1.39$, and loss tangent $\tan \delta = 0.01$ is used to design and fabricate the proposed antenna. The substrate of desired thickness is prepared by cutting and sewing the polyester cloth. According to the designed dimensions and shapes the radiating patch, square SRR, and ground plane of the antenna are cut from the self-adhesive copper tape of thickness 0.1 mm and tightly adhered on the prepared substrate. The size of this antenna at resonance frequency 5.10 GHz is $0.254\lambda \times 0.5\lambda$. This antenna is simulated using method of moment-based IE3D electromagnetic simulator.

The advantages of this antenna are as follows. (a) In this antenna design the slots are cut in the rectangular microstrip patch to make the antenna compact due to which the metal portion of the radiating patch has been removed. Thus, as compared to the conventional rectangular microstrip patch antenna (without slots), small portion of the proposed antenna (with slots) gets bent due to the body movements. Hence, the unwanted bending effects on the resonant frequency and impedance matching (S_{11}) of the antenna have been reduced. (b) This type of geometry is useful to reduce the deposition of electromagnetic field, that is, SAR, due to the fringing field entering in the body tissues. (c) Lower resonant frequency has been achieved.

3. Results and Discussion

Initially, the metamaterial characteristics of the square SRR are verified and presented before analyzing its loading effect on the proposed rectangular microstrip patch antenna. Figure 3 shows the reflection (S_{11}) and transmission (S_{21}) coefficient characteristics of the square SRR that resonates at

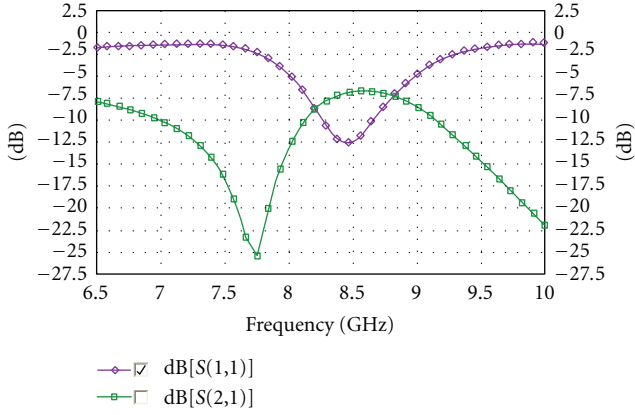


FIGURE 3: Reflection (S_{11}) and transmission (S_{21}) coefficient characteristics of square SRR.

8.48 GHz. The effective medium theory is used to verify the permeability (μ_r) and permittivity (ϵ_r) from the reflection and transmission coefficients (S -parameters). The Nicolson-Ross-Weir (NRW) approach is used to obtain these effective medium parameters. The expressions of (3) are used to determine the effective parameters [10, 12, 19–23]. The metamaterial characteristics of the SRR are verified using the S -parameters obtained from IE3D electromagnetic simulator and MATLAB code with mathematical (3) [10, 12, 19–23]:

$$\begin{aligned} \mu_r &= \frac{2}{jk_0 h} \frac{1 - V_2}{1 + V_2}, \\ \epsilon_r &= \frac{2}{jk_0 h} \frac{1 - V_1}{1 + V_1}, \end{aligned} \quad (3)$$

where k_0 is wave number, h is substrate thickness, V_1 and V_2 are composite terms to represent the addition and subtraction of S -parameters. The values of V_1 and V_2 are calculated as $V_1 = S_{21} + S_{11}$ and $V_2 = S_{21} - S_{11}$. The factor $k_0 h = 0.336$ which is $\ll 1$ [19–23].

Figure 3 shows that the square SRR resonates at 8.48 GHz in the range of 8.35 GHz to 8.7 GHz with good impedance matching. Figure 4 depicts the relative permeability (μ_r) characteristics of the square SRR which indicate that the SRR is a single negative, that is, mu negative (MNG) metamaterial. The value of permeability (μ_r) is negative in the frequency range of 8.35 GHz to 8.7 GHz. This SRR is embedded inside the slot to load the rectangular microstrip patch. The negative magnetic permeability of the SRR in the frequency range 8.35 GHz to 8.7 GHz significantly improves the impedance matching to the source at desired resonance frequency 5.10 GHz which is much lower than the isolated antenna. Thus, MNG SRR provides the miniaturization of the rectangular microstrip patch antenna to obtain the desired subwavelength performance. In this frequency range, the equivalent capacitance of MNG SRR has large capacitance and the patch has large inductance which forms LC resonator that resonates at 5.10 GHz. The value of relative magnetic permeability at working frequency 5.10 GHz is real.

Basically, SRR is an LC resonant circuit. The resonant frequency of the square SRR is calculated by using equivalent

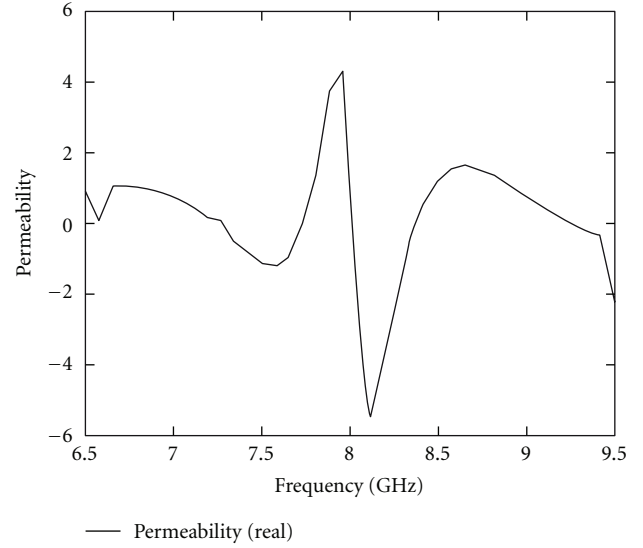


FIGURE 4: Relative permeability (μ_r) characteristics of the square SRR.

circuit theory to validate it with the simulated frequency. The inductance (L) of the square SRR is calculated using (4) [12, 21–23]:

$$L = \frac{\mu_0}{2} \frac{L_{s\text{avg}}}{4} 4.86 \left[\ln \frac{0.98}{\rho} + 1.84\rho \right], \quad (4)$$

where μ_0 is the free space permeability ($4\pi \times 10^{-7}$ H/m), ρ is the filling ratio expressed as $\rho = (N - 1)(w + s)/[L_s - (N - 1)(w + s)]$, the average length of square SRR ($L_{s\text{avg}}$) is calculated as $L_{s\text{avg}} = 4[L_s - (N - 1)(w + s)]$, and N is the number of split rings.

The equivalent capacitance (C), that is, capacitance per unit length of the square SRR, is calculated using (5) [12, 21–23]:

$$C = \epsilon_0 \frac{N - 1}{2} [2L_s - (2N - 1)(w + s)] \frac{K\sqrt{1 - k_1^2}}{K(k_1)}, \quad (5)$$

where ϵ_0 is the free space permittivity (8.854×10^{-12} F/m), K is the complete elliptic integral of first kind, k_1 is the argument of integral expressed as $k_1 = (s/2)/(w + s/2)$.

Thus, by using equivalent circuit theory and mathematical equations, the calculated values of equivalent circuit elements are inductance $L = 30$ nH and capacitance $C = 0.0119$ pF. Theoretically, using the values of L and C the resonant frequency of SRR is calculated to 8.43 GHz. The simulated resonant frequency of SRR is 8.48 GHz (Figure 3) which is in good agreement with the theoretical results. Figure 5 depicts the simulated return loss (S_{11}) characteristics of the rectangular microstrip patch antenna without the slots and metamaterial SRR. In this configuration, the antenna resonates at 8.97 GHz which is in good agreement with the designed frequency. Further, to decrease the resonant frequency of this antenna to WLAN frequency-band applications the slots are cut in the radiating patch. To obtain

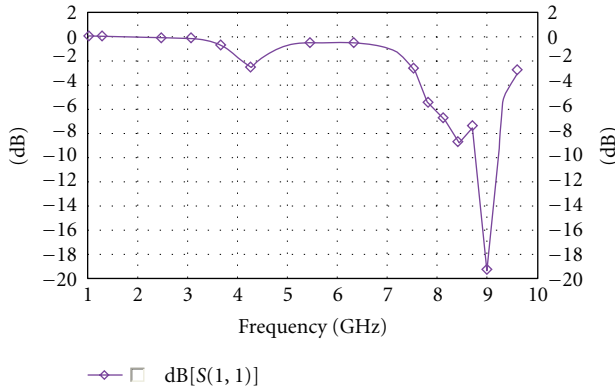


FIGURE 5: Simulated reflection coefficient characteristics of rectangular microstrip patch antenna without cut and square SRR.

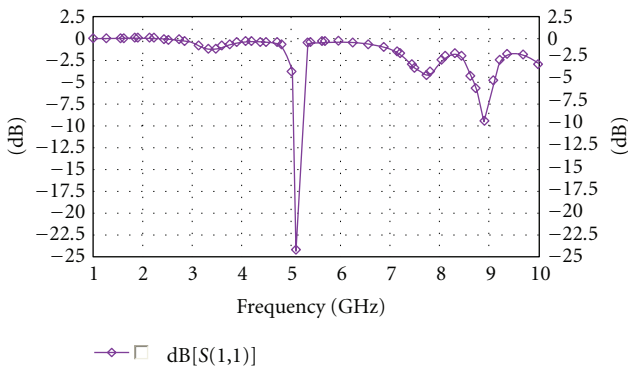


FIGURE 6: Simulated reflection coefficient characteristics of meta-material embedded wearable rectangular microstrip patch antenna.

the better impedance matching a square SRR is placed in the square slot.

Figure 6 depicts the simulated reflection coefficient (S_{11}) characteristics of proposed wearable antenna with the slots and embedded square SRR. In this condition, the antenna resonates at 5.10 GHz with a bandwidth and gain of 97 MHz and 4.95 dBi, respectively. Further, to validate the simulated and measured results the fabricated antenna is tested.

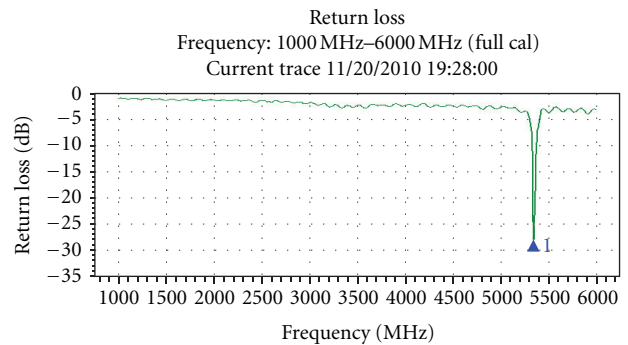
Figure 7 shows the photograph of experimental set up of testing and measurement of the fabricated antenna. Bird site analyzer (Model no. SA-6000EX, Frequency range 25 MHz to 6 GHz) interfaced with a personal computer is used to measure the return loss characteristics of the fabricated antenna.

Figure 8 shows the measured reflection coefficient (S_{11}) characteristics of the fabricated metamaterial square SRR loaded wearable rectangular microstrip patch antenna which resonates at 5.34 GHz with the better matching at -27.96 dB. Figure 9 shows the measured VSWR 1.07 at the resonance frequency 5.34 GHz. The weight of fabricated antenna is measured by a digital weighing machine Essae (DS-852) and found to 2.8 gm with SMA connector (1.2 gm without SMA connector).

Figures 10(a) and 10(b), respectively, illustrate the azimuth and elevation radiation patterns of the proposed

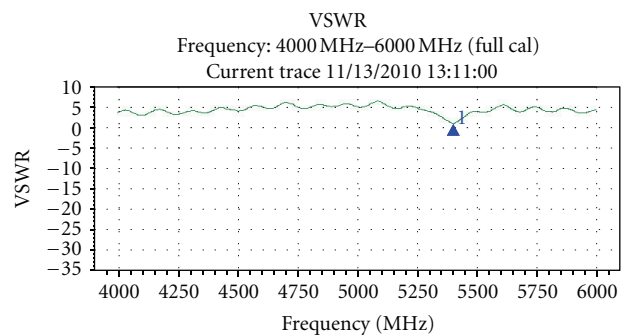


FIGURE 7: Photograph of experimental set up of fabricated metamaterial square SRR embedded wearable rectangular microstrip patch antenna.



M1: (5345.99, -27.96)

FIGURE 8: Measured reflection coefficient (S_{11}) characteristics of metamaterial square SRR embedded wearable rectangular microstrip patch antenna.



M1: (5400.84, 1.07)

FIGURE 9: Measured VSWR characteristics of metamaterial square SRR embedded wearable rectangular microstrip patch antenna.

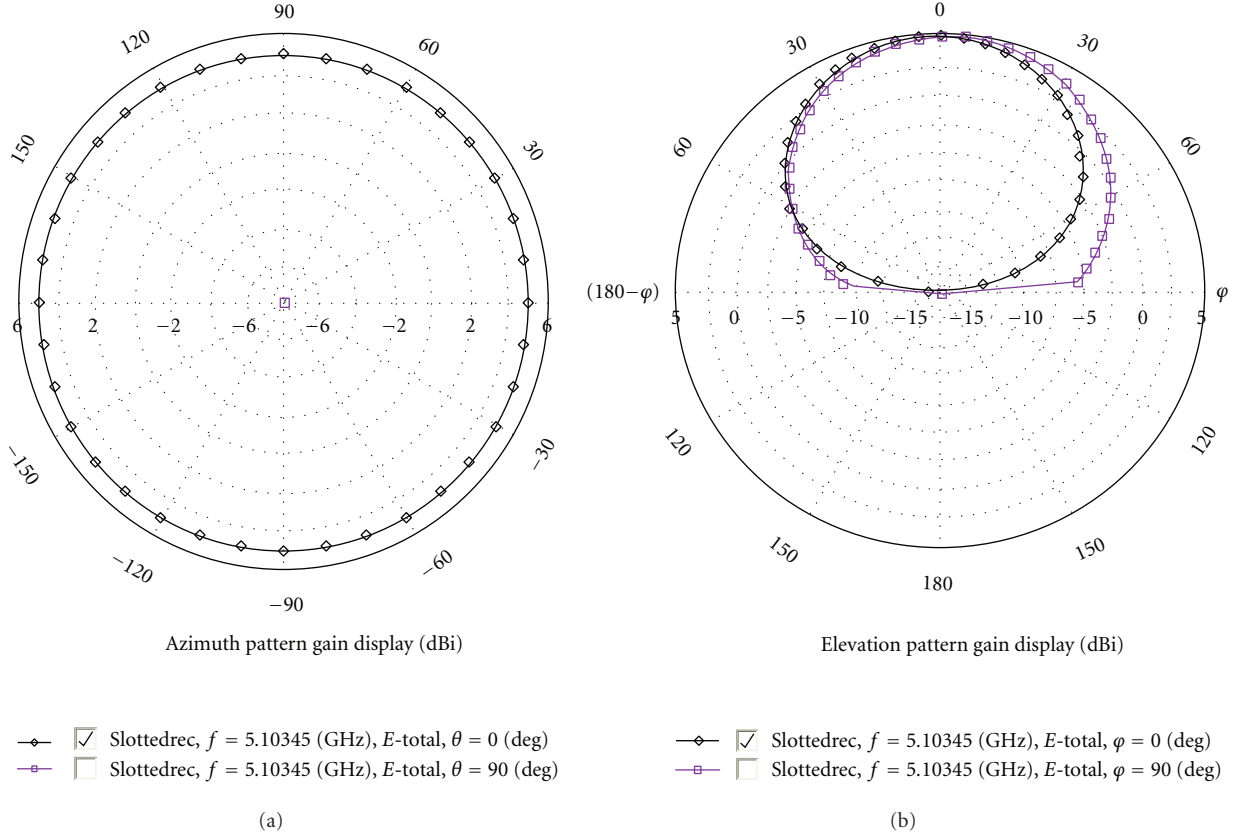


FIGURE 10: Radiation patterns of metamaterial square SRR embedded wearable rectangular microstrip patch antenna. (a) Azimuth. (b) Elevation.

antenna. The gain and directivity of this antenna is 4.95 dBi and 8.60 dBi, respectively.

Figures 11(a) and 11(b), respectively, depict the simulated surface and vector current distribution along the proposed wearable rectangular microstrip antenna without and with the square SRR embedded inside the slot. The current is not uniformly distributed when the SRR is not embedded as shown in Figure 11(a).

When the square SRR is embedded inside the slot current flows along slotted portion and due to the electromagnetic induction the time varying flux induces the current on the outer and inner split rings of square SRR (Figure 11(b)). The arrow shows current flow along the microstrip patch and the square SRR. The current is uniformly distributed along the slot of the antenna. Thus, the SRR embedding makes the uniform current distribution along the antenna. It results in inducing the large electric field across the gap capacitance at the splits and mutual capacitance between the split rings. Under loading condition, the mutual inductance between the square SRR and the edge of rectangular patch is calculated to $M = 0.873$ nH using (6):

$$M = \frac{\mu_0 L_s}{2\pi} \left[0.467 + \frac{0.059(W_x + w)^2}{L_s^2} \right], \quad (6)$$

where W_x is the edge width of the slotted rectangular patch as shown in Figure 1(b). The inductance of slotted antenna

and the equivalent capacitance of the square SRR form the LC resonator circuit of the SRR embedded rectangular microstrip patch antenna which in turn provides the better impedance matching at resonance frequency 5.10 GHz.

4. Experimental Study of Bending Effects on the Wearable Antenna Performance

In Section 3, the performance of the proposed antenna is theoretically and experimentally verified under the flat surface condition. In practice, the wearable antenna is installed as an integrated part of the clothing on different parts of the human body like shoulder, forearm, wrist, waist, and thigh. The bending of wearable antenna takes place according to the frequent movements of the human body. Therefore, an experimental study is executed to examine the bending effect on impedance matching and the resonance frequency of proposed wearable antenna under different bending conditions. In this experiment, the shoulder, wrist, knee shapes of human body are realized by using the curved surfaces of two cylindrical polyvinyl chloride (PVC) pipes of internal radius 54.5 mm and 44.5 mm, respectively. The proposed antenna is tested by properly bending and swaddling it on surface of both of the PVC pipes. Figure 12 represents the photographs of PVC pipes used in this experimentation. Figure 13 shows a snapshot of experimental set up to study

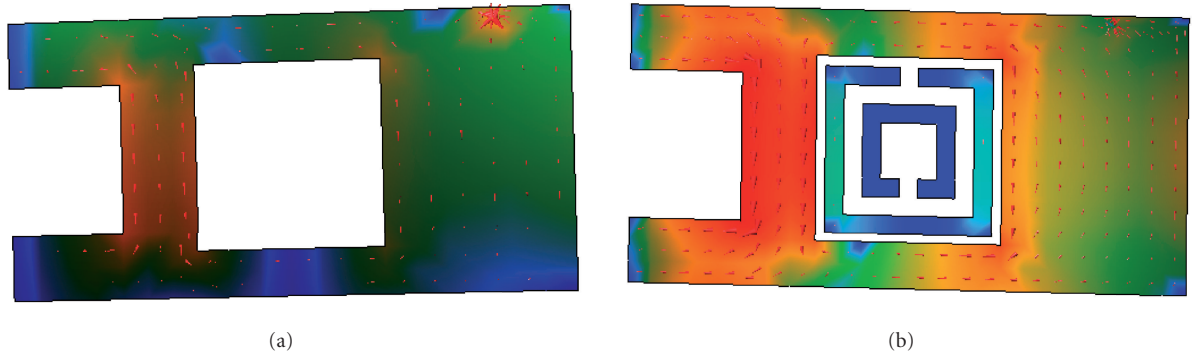


FIGURE 11: Simulated surface and vector current distribution along wearable rectangular microstrip patch antenna. (a) Without embedding the square SRR. (b) With embedded square SRR inside the slot.



FIGURE 12: Photographs of proposed antenna bent on PVC pipes of 54.5 mm and 44.5 mm radii.



FIGURE 13: Photograph of experimental set up to test the bending effect on fabricated metamaterial SRR embedded wearable rectangular microstrip patch antenna.

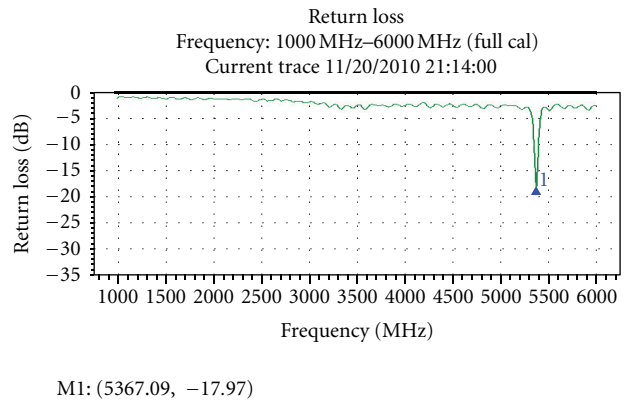


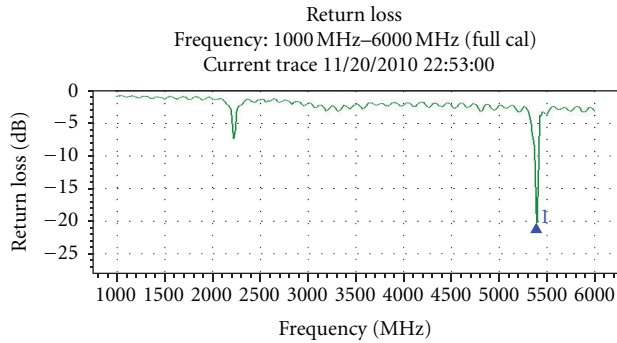
FIGURE 14: Measured reflection coefficient (S_{11}) characteristics of the proposed wearable antenna bent on 54.5 mm radius PVC pipe.

the bending effect on proposed wearable antenna swaddled on the PVC pipe.

Figures 14 and 15, respectively, depict the measured return loss (S_{11}) characteristics of the antenna under bending conditions on the PVC pipes of radii 54.5 and 44.5 mm, respectively.

When this antenna is bent on the pipe of radius 54.5 mm it resonates at 5.367 GHz with return loss of -17.97 dB as

shown in Figure 14. Similarly, when the antenna is bent on pipe radius of 44.5 mm the resonant frequency of the antenna is shifted to 5.388 GHz with the return loss is -20.22 dB as shown in Figure 15. From the experimental results it is observed that in bending condition the resonant frequency of the proposed antenna is shifted to higher side when the antenna is more bent because the resonant length of the antenna is reduced. When the reflection coefficient



M1: (5388.19, -20.22)

FIGURE 15: Measured reflection coefficient (S_{11}) characteristics of the proposed wearable antenna bent on 44.5 mm radius PVC pipe.



FIGURE 16: On body positioning of the fabricated metamaterial SRR embedded wearable rectangular microstrip patch antenna.

(S_{11}) and impedance bandwidth of measured results in bending conditions are studied, no extensive changes in the performance of the proposed antenna are observed.

Figure 16 shows the photographs of on body positioning of the fabricated wearable antenna on the helmet and shoulder, respectively. Thus, it is observed that the slotting means metal removing technique which is an advantageous

approach to (a) reduce the adverse effects on wearable antenna due to bending and (b) minimize the electromagnetic absorption (SAR) in the human body. The impedance mismatch due to slotting in the microstrip patch at the subwavelength resonance is well matched by embedding the metamaterial SRR. This technique avoids the complex techniques to reduce the size and to enhance the performance of microstrip patch antennas like meandering, shorting pin, and so forth.

5. Conclusion

In this paper, a metamaterial square SRR embedded wearable rectangular microstrip patch antenna for IEEE 802.11a WLAN applications is presented. The bending effect on the performance of wearable antenna can be reduced making slots in the radiating patch but it leads to mismatching the impedance at the subwavelength resonance, that is, at desired lower resonance frequency. It is found that the embedding a metamaterial SRR is an advantageous approach to obtain the better impedance matching at the desired resonance frequency. This SRR introduces additional inductance, capacitance, and mutual inductance to match the impedance at the required frequency. The simulated and measured frequency of the proposed wearable antenna is found to be in good agreement. The important features of this antenna are light weight, simple fabrication, and low cost. In further study, the authors have extended their work to measure the SAR of the proposed antenna.

Acknowledgments

The authors sincerely express their gratitude to the anonymous reviewers for their valuable comments. The support of Director, National Institute of Technical Teachers Training and Research (NITTTR), Chandigarh, India, is thankfully acknowledged. J. G. Joshi is highly indebted to Director, Directorate of Technical Education, Mumbai (M.S.), India, and Principal, Government Polytechnic, Pune, India, for sponsoring him to pursue full time Ph.D. under AICTE sponsored Ph.D. QIP (POLY) scheme.

References

- [1] P. S. Hall, Y. Hao, and S. L. Cotton, "Advances in antennas and propagation for body centric wireless communications," in *Proceedings of the 4th European Conference on Antennas and Propagation (EuCAP '10)*, April 2010.
- [2] C. Hertleer, H. Rogier, L. Vallozzi, and L. Van Langenhove, "A textile antenna for off-body communication integrated into protective clothing for firefighters," *IEEE Transactions on Antennas and Propagation*, vol. 57, no. 4, pp. 919–925, 2009.
- [3] S. H. Choi, T. J. Jung, and S. Lim, "Flexible antenna based on compact right/left-handed transmission line," *Electronic Letters*, vol. 46, no. 17, pp. 1181–1182, 2010.
- [4] A. Tronquo, H. Rogier, C. Hertleer, and L. Van Langenhove, "Robust planar textile antenna for wireless body LANs operating in 2.45 GHz ISM band," *Electronics Letters*, vol. 42, no. 3, pp. 21–22, 2006.

- [5] S. Sankaralingam and B. Gupta, "Development of textile antennas for body wearable applications and investigations on their performance under bent conditions," *Progress in Electromagnetics Research B*, no. 22, pp. 53–71, 2010.
- [6] P. Salonen and Y. Rahmat-Samii, "Textile antennas: effects of antenna bending on input matching and impedance bandwidth," *IEEE Aerospace and Electronic Systems Magazine*, vol. 22, no. 3, pp. 10–14, 2007.
- [7] A. Alù, F. Bilotti, N. Engheta, and L. Vegni, "Subwavelength, compact, resonant patch antennas loaded with metamaterials," *IEEE Transactions on Antennas and Propagation*, vol. 55, no. 1, pp. 13–25, 2007.
- [8] P. Y. Chen and A. Alu, "Dual-mode miniaturized elliptical patch antenna with μ -negative metamaterials," *IEEE Antennas and Wireless Propagation Letters*, vol. 9, pp. 351–354, 2010.
- [9] F. Bilotti, A. Alu, and L. Vegni, "Design of miniaturized metamaterial patch antennas with μ -negative loading," *IEEE Transactions on Antennas and Propagation*, vol. 56, no. 6, pp. 1640–1647, 2008.
- [10] J. G. Joshi, S. S. Pattnaik, S. Devi, and M. R. Lohokare, "Electrically small patch antenna loaded with metamaterial," *IETE Journal of Research*, vol. 56, no. 6, pp. 373–379, 2010.
- [11] J. Montero-de-Paz, E. Ugarte-Muñoz, F. J. Herraiz-Martínez, V. González-Posadas, L. E. García-Muñoz, and D. Segovia-Vargas, "Multifrequency self-diplexed single patch antennas loaded with split ring resonators," *Progress in Electromagnetics Research*, vol. 113, pp. 47–66, 2011.
- [12] J. G. Joshi, S. S. Pattnaik, S. Devi, and M. R. Lohokare, "Frequency switching of electrically small patch antenna using metamaterial loading," *Indian Journal of Radio and Space Physics*, vol. 40, no. 3, pp. 159–165, 2011.
- [13] J. G. Joshi, S. S. Pattnaik, S. Devi, and M. R. Lohokare, "Microstrip patch antenna loaded with magnetoinductive waveguide," in *Proceedings of the 12th National Symposium on Antennas and Propagation (APSYM '10)*, pp. 101–105, Department of Electronics, Cochin University of Science and Technology (CUSAT), Cochin, India, 2010.
- [14] F. E. Gardiol, "Report on APSYM'2010: national symposium on antennas and propagation," *IEEE Antennas and Propagation Magazine*, vol. 53, no. 1, pp. 123–126, 2011.
- [15] S. S. Pattnaik, J. G. Joshi, S. Devi, and M. R. Lohokare, "Electrically small rectangular microstrip patch antenna loaded with metamaterial," in *Proceedings of the International Symposium on IEEE Antennas and Propagation Society*, pp. 247–250, Guangzhou, China, December 2010.
- [16] J. N. Hwang and F. C. Chen, "Study of SAR reduction with split ring resonators," in *Proceedings of the IEEE Antennas and Propagation Society International Symposium and USNC/URSI Meeting*, vol. 2, pp. 780–783, Washington, DC, USA, July 2005.
- [17] V. G. Veselago, "The electrodynamics of substances with simultaneously negative values of ϵ and μ ," *Soviet Physics Uspekhi*, vol. 10, pp. 509–514, 1968.
- [18] J. B. Pendry, A. J. Holden, D. J. Robbins, and W. J. Stewart, "Magnetism from conductors and enhanced nonlinear phenomena," *IEEE Transactions on Microwave Theory and Techniques*, vol. 47, no. 11, pp. 2075–2084, 1999.
- [19] D. R. Smith, D. C. Vier, T. Koschny, and C. M. Soukoulis, "Electromagnetic parameter retrieval from inhomogeneous metamaterials," *Physical Review E*, vol. 71, no. 3, Article ID 036617, 11 pages, 2005.
- [20] R. W. Ziolkowski, "Design, fabrication, and testing of double negative metamaterials," *IEEE Transactions on Antennas and Propagation*, vol. 51, no. 7, pp. 1516–1529, 2003.
- [21] F. Bilotti, A. Toscano, L. Vegni, K. Aydin, K. B. Alici, and E. Ozbay, "Equivalent-circuit models for the design of metamaterials based on artificial magnetic inclusions," *IEEE Transactions on Microwave Theory and Techniques*, vol. 55, no. 12, pp. 2865–2873, 2007.
- [22] J. G. Joshi, S. S. Pattnaik, S. Devi, and M. R. Lohokare, "Bandwidth enhancement and size reduction of microstrip patch antenna by magnetoinductive waveguide loading," *Journal of Wireless Engineering and Technology*, vol. 2, no. 2, pp. 37–44, 2011.
- [23] J. G. Joshi, S. S. Pattnaik, and S. Devi, "Partially metamaterial ground plane loaded rectangular slotted microstrip patch antenna," *International Journal of Microwave and Optical Technology*, vol. 7, no. 1, pp. 1–11, 2012.
- [24] A. K. Agrawal, S. S. Pattnaik, S. Devi, and J. G. Joshi, "Broadband and high gain microstrip patch antenna for WLAN," *Indian Journal of Radio and Space Physics*, vol. 40, no. 5, pp. 282–286, 2011.
- [25] R. Garg, P. Bhartia, I. Bahl, and A. Ittipiboon, *Microstrip Antenna Design Handbook*, Artech House, Norwood, Mass, USA, 1980.
- [26] I. J. Bahl and P. Bhartia, *Microstrip Antennas*, Artech House, Dedham, Mass, USA, 1980.

Research Article

Improved Successive Interference Cancellation for MIMO/UWB-Based Wireless Body Area Network

M. Jayasheela¹ and A. Rajeswari²

¹Department of Electronics and Communication Engineering, SNS College of Technology, SNS Kalvi Nagar, Saravanampatti, Coimbatore 641035, India

²Department of Electronics and Communication Engineering, Coimbatore Institute of Technology, Peelamedu, Coimbatore 641014, India

Correspondence should be addressed to M. Jayasheela, jayasheela.ece.snsct@gmail.com

Received 24 February 2012; Accepted 21 June 2012

Academic Editor: C. Aanandan

Copyright © 2012 M. Jayasheela and A. Rajeswari. This is an open access article distributed under the Creative Commons Attribution License, which permits unrestricted use, distribution, and reproduction in any medium, provided the original work is properly cited.

In body area networks, various sensors are attached to clothing or on the body or even implanted under the skin. The sensors measure such as heart beat, the record of prolonged electrocardiogram, blood pressure, and so on. In this paper, an improved Successive interference cancellation (SIC) scheme based on zero correlation zone sequences is proposed. Here ZCZ is used as a random code for TH PPM UWB system. Nodes in a WBAN are connected through wireless communication channel within a very close range. The decrease in internode distance leads to interference between devices. To reduce this interference, an enhanced successive interference cancellation scheme based on ZCZ with optimal ordering is adopted. Because of zero correlation property of ZCZ, the performance of TH PPM UWB system through WBAN channel with ZCZ sequences outperforms performance of existing zero correlation duration code. In this paper, performance of UWB system for various modulation schemes are compared. Performance of UWB/MIMO (2×2) system employing SIC with optimal ordering using ZCZ codes also compared with pseudorandom (PN) and ZCD codes. Simulation results are obtained using sample biological functions as input to the proposed TH PPM UWB/MIMO (2×2) system with m-ZCZ codes in WBAN environment with multiple devices.

1. Introduction

Monitoring of physiological conditions of a patient who is in remote is possible nowadays with the help of wireless medical telemetry [1–3]. This enhances the quality of patient care and the efficiency of hospital administration capabilities. It also helps to reduce healthcare costs because it permits the remote monitoring of several patients simultaneously. The development of this technology leads to wireless body area network (WBAN) [4] where smart wireless medical sensors measuring, for example, electrocardiogram (ECG), noninvasive blood pressure, and the blood oxygen saturation placed in and around the body can communicate with the outside world using wireless networks and provide medical information. The realtime information can be forwarded to a physician.

Ultrawideband (UWB) communication has strong advantages quite promising for WBAN applications [5] because

it offers a low-power high data rate technology with large bandwidth signals that provides robustness to jamming and has low probability of interception [6]. UWB low transmit power requirements, which are mainly used in low data rate networks with low duty cycles, allow longer battery life for body worn units [4]. Moreover, UWB can be used to monitor vital parameters such as respiration and heart rate [4]. In addition, UWB gives good penetrating properties that could be implemented to imaging in medical applications [7].

In the WBAN, radio propagations from devices that are close to or inside the human body are complex and distinctive comparing to the other environments since the human body has a complex shape consisting of different tissues with their own permittivity and conductivity.

The UWB system with the help of multiple-input-multiple-output (MIMO) scheme employs features such as spatial diversity and spatial multiplexing, leading to higher system throughput. However, in UWB/MIMO systems, the

performance degradation may be caused by the effects of multiple access interference (MAI) and multipath fading. In the literature [7], successive interference cancellation (SIC) scheme has been proven to work well for interference cancellation of outdoor communication and other multimedia transmission systems. Therefore, SIC scheme can be one of the promising solutions to mitigate interference effects on the performance of WBAN.

Bae et al. show that interference mitigated due to MAI by introducing optimal SIC for UWB/MIMO using zero correlation duration code as spreading code for UWB system in a multidevice environment. Performance comparison of ZF-OSIC, MMSE-OSIC is analyzed [7].

In our previous paper [8], BER performance of CDMA system was found using ZCZ sequences. ZCZ sequences have both autocorrelation side lobes, cross-correlation function are zero, and sequence length is flexible [8].

In this paper, improved interference cancellation schemes for UWB/MIMO-based wireless body area network using m-ZCZ sequences are proposed. In this work, TH PPMUWB system with zero correlation zone code is used as a spreading code which has robust MAI capability. The system performance is analysed in terms of BER.

The paper deals with the following WBAN channel is explained in Section 2. The proposed UWB/MIMO system model is described in Section 3. Performance analysis is given in Section 4. Simulation Results are presented in Section 5. Conclusion is given in, last section.

2. WBAN Channel Model

Figure 1 shows the possible communication links for WBAN. WBAN channel are classified into two categories according to the field of applications [7]. The first category is a nonmedical application where the user is using the wireless connection between his MP3 player and headset. The other category is medical application related to patient health care domain. In latter case, a patient can wear communication equipment with the smart sensors that can constantly measure the patient biological information such as blood pressure, heart rate, electrocardiogram (ECG), electroencephalogram (EEG), respiration, and so on. According to location of equipment, there are three types: in-body, on-body, and off-body. Moreover, speed is categorized as low, moderate, and high. Table 1 gives the Classification of the WBAN systems for various criteria [7].

The distance between the external devices is typically considered to be a maximum of 5 meters. Table 2 shows the parameters of WBAN Channels for different direction of body [7].

In WBAN channel, the complex impulse response $h_i(t)$ for the i th device is given by [7] as following:

$$h_i(t) = \sum_{m=0}^{m-1} \alpha_m^i \delta(t - \tau_m^i), \quad (1)$$

where m is the number of total arrival paths and modeled as passion random variables with mean value of 400, m is the

TABLE 1: Classification of WBAN channel.

Criterion	WBAN channel mode		
	Nonmedical	Medical	
Field of application			
Location	In-body	On-body	Off-body
Speed	Low	Middle	High

TABLE 2: Parameters of WBAN channel for different direction of body.

Direction of body in degrees	Γ in ns	F_k	σ (dB)
0	44.6346	5.111	7.3
90	54.2868	4.348	7.08
180	53.4186	3.638	7.03
270	83.9635	3.983	7.19

m th arrival path of the signal and α_m^i is the magnitude of m th path;

$$|\alpha_m^i|^2 = L_0 \exp\left(-\frac{\tau_m^i}{\Gamma} - F_k[1 - \delta(m)]\right)\beta, \quad (2)$$

where L_0 is a path Loss, Γ is an exponential decay factor, β is a log random variable, τ_m^i is described as path arrival time, d is the distance between m th device and the receiver, and F_k is an effect of the K -factor in nonlinear sight that can be calculated as

$$F_k = \frac{\Delta k \ln 10}{10}. \quad (3)$$

3. Proposed System Model

Figure 2 shows the block diagram of Proposed UWB/MIMO system using m-ZCZ codes.

The data from devices are transmitted by using TH PPM UWB modulator. As a spread code of TH PPM UWB systems, the zero correlation zone code with robust MAI is employed for random hopping. Then the signal is fed into UWB MIMO (2×2) encoder and it is fed through WBAN channel with the channel parameters shown in Table 2. At the receiver side, incoming data is processed by MMSE equalizer and is followed by SIC scheme with optimal ordering in order to mitigate the interference.

The Channel impulse response in the WBAN channel with multipath propagation can be expressed as

$$h(t) = \sum_{m=0}^{k-1} \alpha(m) \delta(t - mT_p), \quad (4)$$

where k is the total number of multipath components, $\alpha(m)$ is a fading coefficient of the m path. $\delta(t)$ is dirac delta uncton. T_p is the minimum multipath resolution.

The received signal $Y_p(t)$ at the P th receive antenna is given as

$$Y_p(t) = \sum_{n=1}^N \sum_{m=0}^K h_{p,n}(k) x_n(t - kT_p) + n_k(t), \quad (5)$$

where $h_{p,n}(k)$ represents a fading coefficient of m th path for the signal from n th transmit Antenna to the p th receive antenna. $n_k(t)$ is the additive white Gaussian noise.

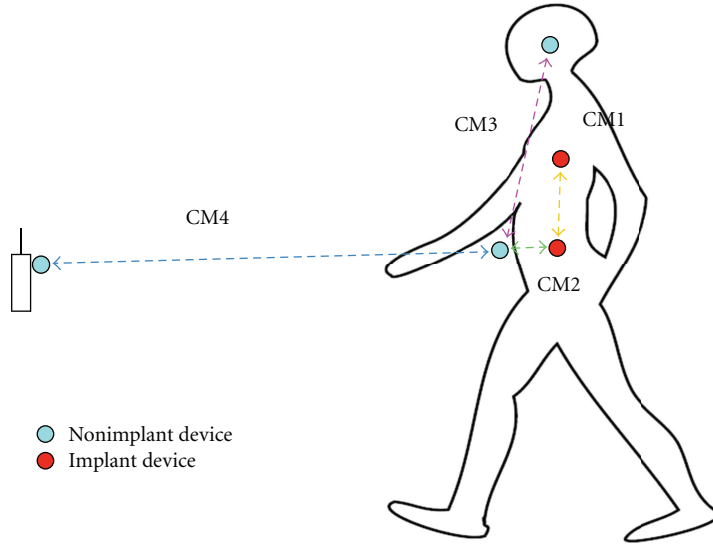


FIGURE 1: Possible communication links for WBAN.

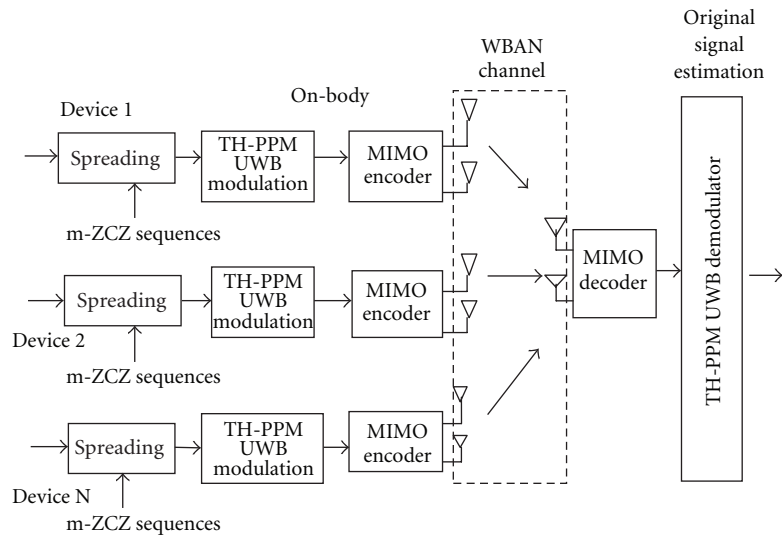


FIGURE 2: Proposed UWB/MIMO system using m-ZCZ codes.

3.1. *ZCZ Sequences.* The m-ZCZ code set is denoted as $m\text{-ZCZ}(C_L, S, W_{\min}) = \{(z_{i1}, z_{i2})\}$, where $i = 0, 1, \dots, S-1$, and C_L represents code length, S is set size of the code set, and W_{\min} is minimum length of one-side ZCZ.

The first subcode of the i th code is $z_{i1} = a^{i \cdot w_{\min}}$ with the length of N , where a^0 is an m -sequence with its period N , and $a^{i \cdot w_{\min}}$ stands for the sequence generated by cyclically leftward shifted a^0 with $i \cdot W_{\min}$ chips. This can be represented as

$$a_n^{i \cdot w_{\min}} = a_{(n+i \cdot w_{\min})}^0 \bmod N, \quad (6)$$

where $n = 0, 1, \dots, N-1$, and n is the chip index.

The second subcode $z_{i2} = \{+1\}$ contains only one “+1” chip. The congregated code length is $C_L = N + 1$. The set size of the code is $S = \lfloor N/W_{\min} \rfloor$.

The periodic autocorrelation function (ACF) of an m-ZCZ code and periodic cross-correlation function (CCF) of any two m-ZCZ codes can be calculated as follows [8]:

$$\begin{aligned} R_{i,j}(k) &= \sum_{n=0}^{N-1} a_n^{i \cdot w_{\min}} a_{n+k}^{j \cdot w_{\min}} + z_{i2} z_{j2} \\ &= \sum_{n=0}^{N-1} a_{(n+i \cdot w_{\min})}^0 \bmod N a_{(n+1+j \cdot w_{\min})}^0 \\ &\quad \times \bmod N + z_{i2} z_{j2} \end{aligned}$$

$$\begin{aligned}
&= \begin{cases} N+1 & i=j, k=0 \\ -1+1 & i=j, 0 < |k| < w_{\min}, \\ & \text{or } i \neq j, |k| < w_{\min} \end{cases} \\
&= \begin{cases} C_L & i=j, k=0 \\ 0 & i=j, 0 < |k| < w_{\min}, \\ & \text{or } i \neq j, |k| < w_{\min}, \end{cases} \quad (7)
\end{aligned}$$

where integer k denotes the relative time shift.

From (7), it is seen that the ACF of any m-ZCZ code is zero when $0 < |k| < W_{\min}$ and the CCF between any two codes is zero $|k| < W_{\min}$. Thus, there exists a ZCZ with minimum one-side length being w_{\min} . The w_{\min} can be flexibly controlled by adjusting the number of cyclic shifted chips.

3.1.1. Example. Given $L = 64$ and $w_{\min} = 30$, a set of m-ZCZ codes are denoted by $(64, 2, 30)$ containing $J = \lfloor 63/30 \rfloor = 2$ codes as

$$\begin{aligned}
&(z_{01}, z_{02}) \\
&= \begin{pmatrix} -1 & 1 & 1 & 1 & 1 & 1 & -1 & -1 \\ -1 & -1 & 1 & 1 & -1 & 1 & 1 & -1 \\ 1 & -1 & 1 & -1 & 1 & -1 & -1 & 1 \\ -1 & 1 & 1 & -1 & -1 & 1 & -1 & 1 \\ 1 & 1 & 1 & -1 & 1 & 1 & 1 & -1 \\ 1 & -1 & -1 & 1 & -1 & -1 & -1 & -1 \\ -1 & -1 & 1 & 1 & 1 & 1 & 1 & -1 \\ 1 & 1 & 1 & -1 & 1 & -1 & -1 & 1 \\ -1 & -1 & -1 & -1 & -1 & -1 & 1 & -1 \\ 1 & -1 & -1 & -1 & 1 & -1 & 1 & -1 \\ -1 & -1 & 1 & 1 & 1 & -1 & -1 & 1 \\ 1 & -1 & -1 & -1 & 1 & -1 & -1 & 1 \\ 1 & 1 & 1 & 1 & -1 & -1 & -1 & 1 \\ 1 & -1 & -1 & 1 & 1 & -1 & -1 & -1 \\ 1 & -1 & 1 & -1 & 1 & 1 & 1 & -1 \\ 1 & 1 & -1 & 1 & -1 & 1 & -1 & 1 \end{pmatrix},
\end{aligned}$$

$$\begin{aligned}
&(z_{11}, z_{12}) \\
&= \begin{pmatrix} -1 & 1 & 1 & 1 & 1 & 1 & -1 & -1 \\ -1 & -1 & 1 & 1 & -1 & 1 & 1 & -1 \\ 1 & -1 & 1 & -1 & 1 & -1 & -1 & 1 \\ -1 & 1 & 1 & -1 & -1 & 1 & -1 & 1 \\ 1 & 1 & 1 & -1 & 1 & 1 & 1 & -1 \\ 1 & -1 & -1 & 1 & -1 & -1 & -1 & -1 \\ -1 & -1 & 1 & 1 & 1 & 1 & 1 & -1 \\ 1 & 1 & 1 & -1 & 1 & -1 & -1 & 1 \\ -1 & -1 & -1 & -1 & -1 & -1 & 1 & -1 \\ 1 & -1 & -1 & -1 & 1 & -1 & 1 & -1 \\ -1 & -1 & 1 & 1 & 1 & -1 & -1 & 1 \\ 1 & -1 & -1 & -1 & 1 & -1 & -1 & 1 \\ 1 & 1 & 1 & 1 & -1 & -1 & -1 & 1 \\ 1 & -1 & -1 & 1 & 1 & -1 & -1 & -1 \\ 1 & -1 & 1 & -1 & 1 & 1 & 1 & -1 \\ 1 & 1 & -1 & 1 & -1 & 1 & -1 & 1 \end{pmatrix}. \quad (8)
\end{aligned}$$

3.2. MMSE Equalizer for 2×2 MIMO Channel. In the first time slot, the received signal on the first receive antenna is

$$y_1 = h_{1,1}x_1 + h_{1,2}x_2 + n_1 = [h_{1,1} \ h_{1,2}] \begin{bmatrix} x_1 \\ x_2 \end{bmatrix} + n_1. \quad (9)$$

The received signal on the second receive antenna is

$$y_2 = h_{2,1}x_1 + h_{2,2}x_2 + n_2 = [h_{2,1} \ h_{2,2}] \begin{bmatrix} x_1 \\ x_2 \end{bmatrix} + n_2, \quad (10)$$

where y_1 and y_2 are the received symbols on the first and second antennas, respectively,

$h_{1,1}$ is the channel from 1st transmit antenna to 1st receive antenna;

$h_{1,2}$ is the channel from 2nd transmit antenna to 1st receive antenna;

$h_{2,1}$ is the channel from 1st transmit antenna to 2nd receive antenna;

$h_{2,2}$ is the channel from 2nd transmit antenna to 2nd receive antenna;

x_1, x_2 are the transmitted symbols and n_1, n_2 is the noise on 1st, 2nd receive antennas.

Assuming that the receiver knows $h_{1,1}, h_{1,2}, h_{2,1}, h_{2,2}$, and y_1, y_2 the matrix representation of the above equation is

$$\begin{bmatrix} y_1 \\ y_2 \end{bmatrix} = \begin{bmatrix} h_{1,1} & h_{1,2} \\ h_{2,1} & h_{2,2} \end{bmatrix} \begin{bmatrix} x_1 \\ x_2 \end{bmatrix} + \begin{bmatrix} n_1 \\ n_2 \end{bmatrix}. \quad (11)$$

Equivalently,

$$y = Hx + n. \quad (12)$$

The minimum mean square error (MMSE) algorithm is used to find a coefficient “ w ” which minimizes the error criterion. The decoding matrix is given by [7]

$$W = [H^H H + N_0 I]^{-1} H^H, \quad (13)$$

where W is equalization matrix and H is channel matrix. This matrix is known as the pseudoinverse for a general $m \times n$ matrix and $N_0 I$ is the noise term, where

$$\begin{aligned}
H^H H &= \begin{bmatrix} h_{1,1}^* & h_{2,1}^* \\ h_{1,2}^* & h_{2,2}^* \end{bmatrix} \begin{bmatrix} h_{1,1} & h_{1,2} \\ h_{2,1} & h_{2,2} \end{bmatrix} \\
&= \begin{bmatrix} |h_{1,1}|^2 + |h_{2,1}|^2 & h_{1,1}^* h_{1,2} + h_{2,1}^* h_{2,2} \\ h_{1,2}^* h_{1,1} + h_{2,2}^* h_{2,1} & |h_{1,2}|^2 + |h_{2,2}|^2 \end{bmatrix}. \quad (14)
\end{aligned}$$

The MMSE algorithm is used to counteract the interference by varying decoding matrix according to SNR. It also prevents the amplification of noise component.

3.3. SIC with Optimal Ordering. The interference cancellation technique SIC is used after linear equalization to mitigate the effect of MAI. In conventional successive interference cancellation, the receiver arbitrarily takes one of the

estimated symbols (e.g., \bar{x}_2) and subtract its effect from the received symbol y_1 and y_2 . If the previous decision is incorrect and error occurs then next decision also could be incorrect [7].

To eliminate the error propagation, SIC with optimal ordering is adopted. SIC with optimal ordering has more intelligence in choosing the effect of \bar{x}_1 first or \bar{x}_2 first and then subtracts corresponding \bar{x}_1 or \bar{x}_2 from the received signal. In this scheme, the strongest signal is cancelled out first followed by the second strongest, and so forth.

The received power at the both the antennas corresponding to the transmitted symbol x_1 is

$$P_{x1} = |h_{1,1}|^2 + |h_{2,1}|^2. \quad (15)$$

The received power at both antennas corresponding to the transmitted symbol x_2 is

$$P_{x2} = |h_{1,2}|^2 + |h_{2,2}|^2. \quad (16)$$

If $P_{x1} > P_{x2}$, then the receiver decides to remove the effect of \bar{x}_1 from the received vectors y_1 and y_2 . Then \bar{x}_2 is reestimated as

$$r_2 = Hx_2 + n, \quad (17)$$

where r is the reestimated signal.

Else if $P_{x1} \leq P_{x2}$ the receiver decides to subtract effect of \bar{x}_2 from the received vectors y_1 and y_2 . Then \bar{x}_1 is reestimated as

$$r_1 = Hx_1 + n. \quad (18)$$

The SIC with optimal ordering guarantees the reliability of the signal decoded first so that signal has minimum error probability.

3.4. Pseudocode for the Proposed System

- (i) Generate random binary sequence of +1's and -1's.
- (ii) Binary sequence is spread using m-ZCZ sequences and groups them into symbols.
- (iii) Spread symbols are converted into UWB pulses. It is modulated using TH PPM modulation (PPM TH-ZCZ).
- (iv) The symbols are transmitted through BAN channel.
- (v) Equalize the received symbols with minimum mean square error criterion.
- (vi) Do successive interference cancellation by both classical and optimal ordering approach.
- (vii) Perform maximal ratio combining for equalizing the new received symbol.
- (viii) Perform hard decision decoding and count the bit errors.
- (ix) BER performance has been compared with PPM-TH, PAM DS-PN, and PAM-DS-ZCD [7].

TABLE 3: Simulation parameters.

Modulation	TH PPM
MIMO scheme	2 by 2
Spreading code	ZCZ
Channel model	WBAN (CM4)
Equalizer	MMSE
Interference cancellation	SIC with
Scheme	Optimal ordering

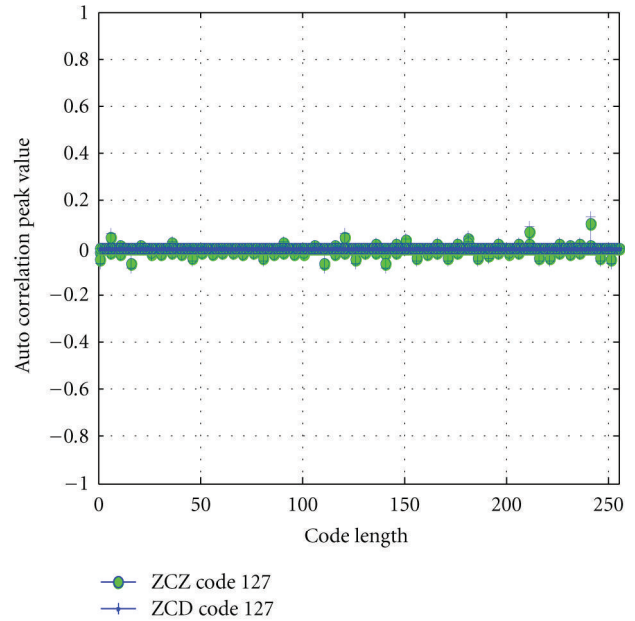


FIGURE 3: Performance of autocorrelation function.

4. Results and Discussion

The performance of the proposed UWB/MIMO system using ZCZ sequences combined with successive interference cancellation scheme is simulated in the WBAN Environment.

In this section, the performance of UWB system for various modulation schemes using ZCZ codes is simulated using Monte Carlo simulations in the WBAN environment. BER performance has been compared with UWB/MIMO (2×2) system employing SIC with optimal ordering for different codes. Table 3 gives the simulation parameters.

Figures 3 and 4 show the performance of the correlation function of ZCD and ZCZ code. It is seen that performance evaluated in terms of correlation peak value. The energy of the side lobes is higher in case of ZCD for the autocorrelation function almost approaches zero in case of ZCZ code and ZCD has comparatively high peak values. Because of good autocorrelation and cross-correlation properties, ZCZ code shows better performance than that of ZCD code.

Figure 5 compares the performance of PN, ZCD, and the proposed ZCZ code with different code lengths for SIC with optimal ordering. Since ZCZ has robust MAI characteristics the ZCZ code showed better performance than that of existing PN and ZCD codes. When $E_b/N_0 = 8$ dB, BER of

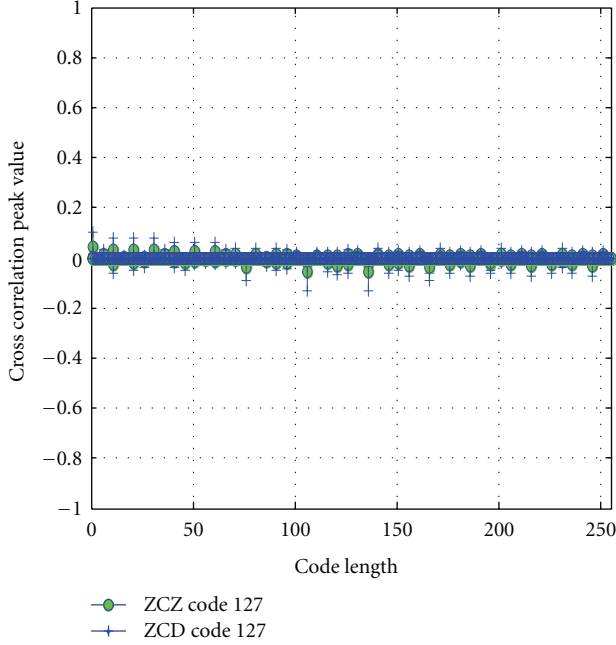


FIGURE 4: Performance of cross-correlation function.

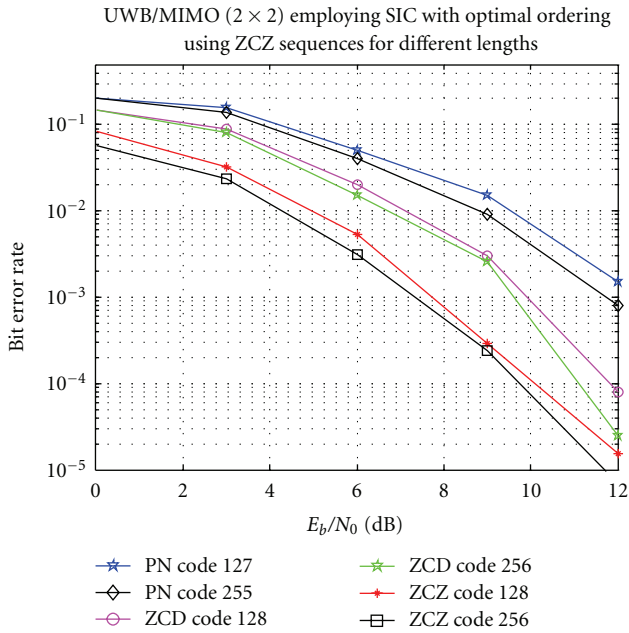


FIGURE 5: Performance of UWB/MIMO (2×2) system employing SIC with optimal ordering using ZCZ sequences for different sequence lengths.

ZCZ code is $\sim 10^{-4}$ and for ZCD code BER value is increased to $\sim 10^{-3}$ and $\sim 10^{-2}$ PN code. From the figure, it is seen that when SNR increases BER of UWB/MIMO system decreases.

Figure 6 shows the performance comparison of UWB system in WBAN for PPM TH [7], PPM TH-ZCZ (proposed), PAM DS-PN [7], and PAM DS-ZCD [7] systems.

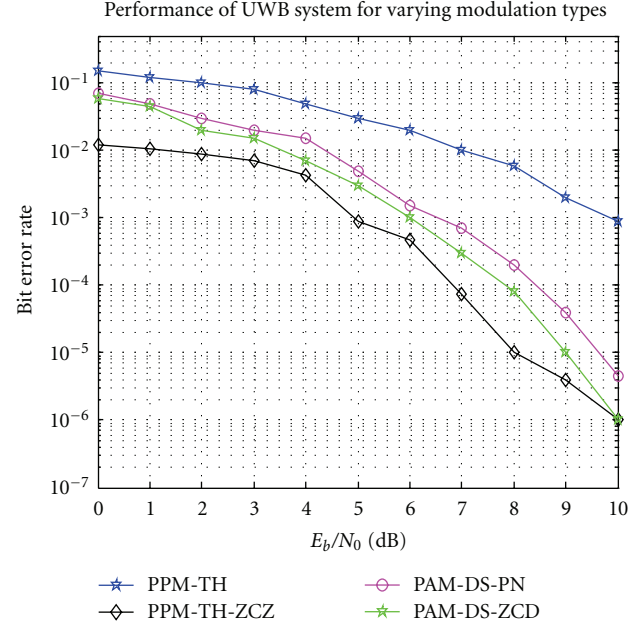


FIGURE 6: Performance of UWB system employing for varying modulation types.

It shows that proposed system with PPM TH-ZCZ outperforms all the other three. In Figure 4, When $E_b/N_0 = 8$ dB, BER value of PPM-TH-ZCZ code is $\sim 10^{-5}$. PAM-DS-ZCD system for same dB the BER is increased to $\sim 10^{-4}$ [7]. In PPM TH system without ZCZ code, BER value is increased to $\sim 10^{-2}$. At 8 dB, it can be seen that PPM TH-ZCZ shows 10% improvement of BER compared with PAM DS-ZCD [7] for the same dB.

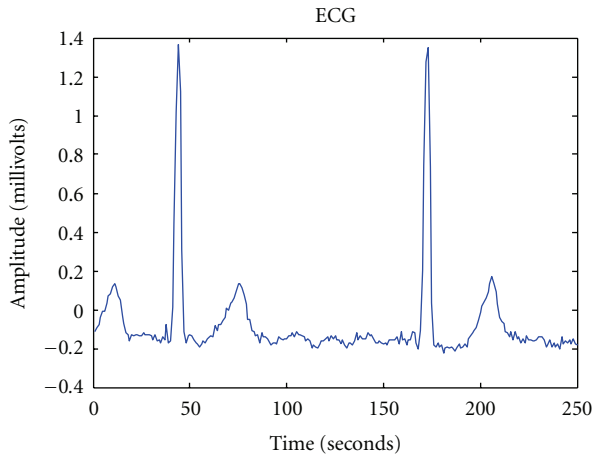
5. Validation

In order to validate the performance of proposed improved successive interference cancellation for MIMO-based wireless body area network, we have considered several devices in WBAN channel for body surface to external (CM4). For testing, BER results have been obtained with multiple biological functions as the input to the various devices in the system model shown in Figure 2. Samples of biological functions such as ECG and blood pressure are given in Figure 7.

In Figures 7(a)–7(c) show that ECG signal of patient is passed through TH-PPM UWB/MIMO system under WBAN environment (CM4). At the receiver side, the signal is demodulated based on TH-code of each patient, despreading, and then decoded to get back the transmitted ECG signal. Similarly, Figures 7(d)–7(f) show that continuous measurement of blood pressure signal of patient is passed through TH-PPM UWB/MIMO system under WBAN environment (CM4). At the receiver side, the signal is demodulated based on TH-code of each patient, despreading, and then decoded to get back the original data.

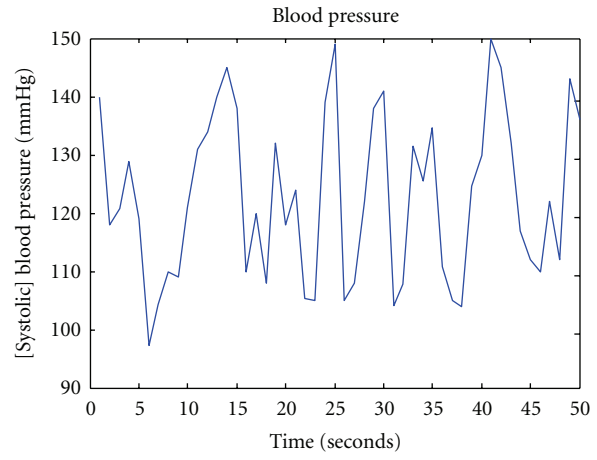
Figure 8 shows the performance of PPM TH-ZCZ UWB/MIMO (2×2) system with 10, 5, and 1 devices in WBAN channel, CM4 with inputs such as ECG and blood pressure.

Biological functions



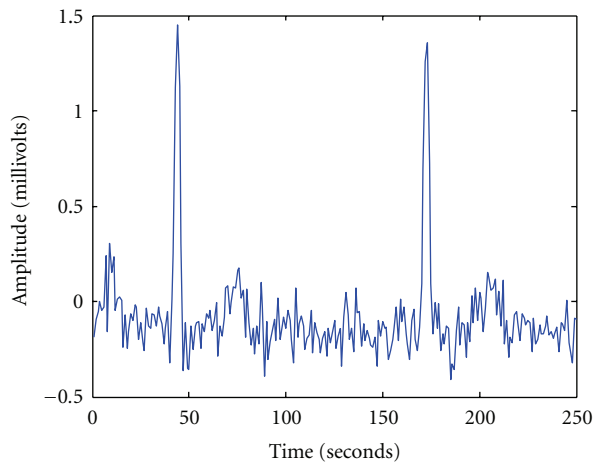
— ECG signal

(a) Measured ECG signal of a patient



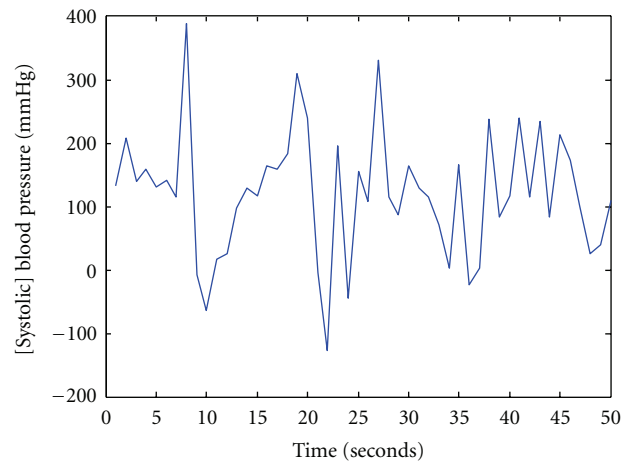
— (Systolic) blood pressure signal

(d) Measured blood pressure (normal) of a patient



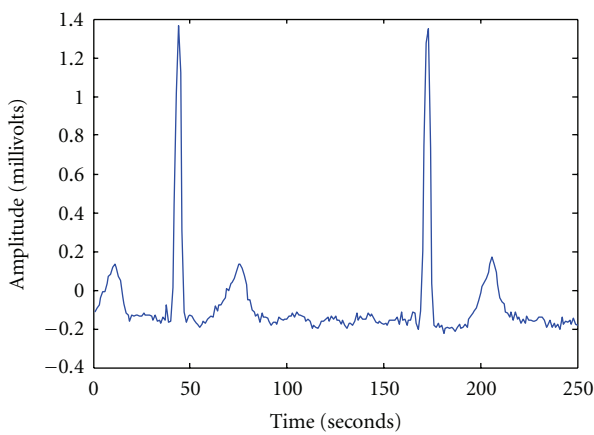
— Noisy ECG signal

(b) After passing through WBAN channel, CM4



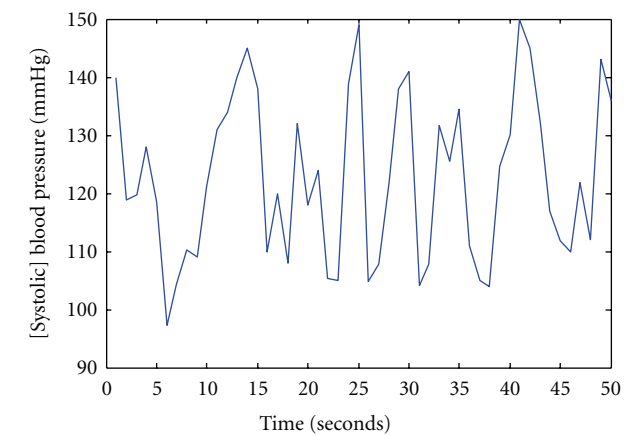
— Blood pressure signal in WBAN channel

(e) After passing through WBAN channel, CM4



— Recovered ECG signal

(c) Recovered signal through proposed UWB/MIMO system using m-ZCZ codes



— Recovered blood pressure signal

(f) Recovered signal through proposed UWB/MIMO system using m-ZCZ codes

FIGURE 7: Transmission/reception of sample biological functions of patients through PPM TH-ZCZ UWB/MIMO (2 × 2) system.

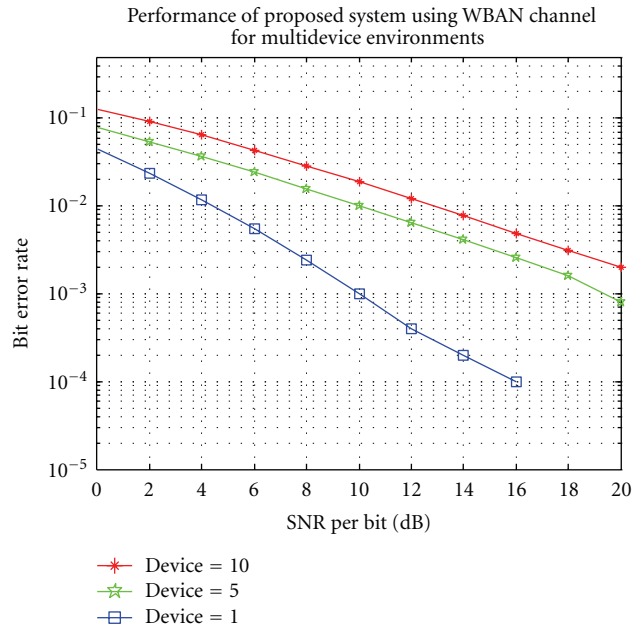


FIGURE 8: Performance of PPM TH UWB/MIMO (2 × 2) system using m-ZCZ codes for multidevice environments in WBAN channel.

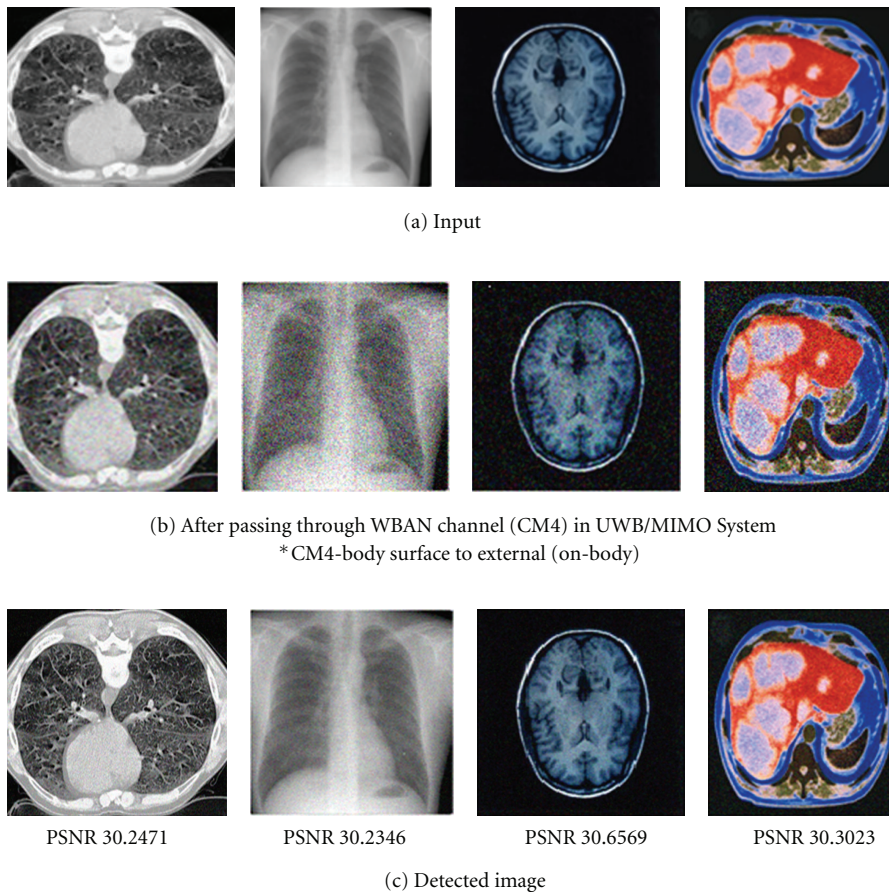


FIGURE 9: PSNR values of sample biomedical images: sample biological images through PPM TH-ZCZ UWB/MIMO (2 × 2) system.

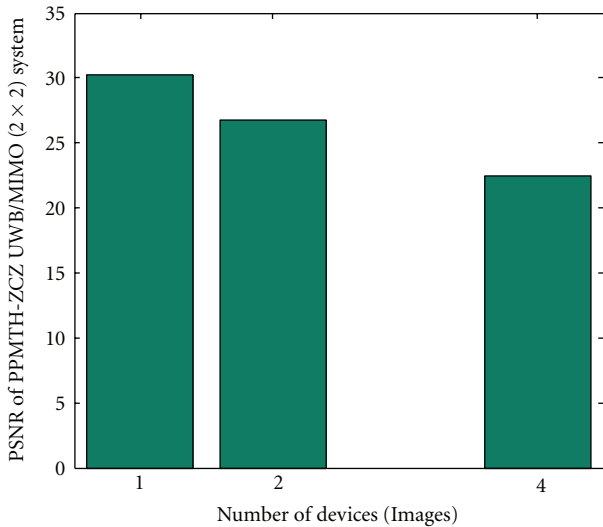


FIGURE 10: Histogram when input as biomedical image for PPM TH-ZCZ UWB/MIMO (2×2) system with multiple devices in WBAN channel (CM4).

From the figure, it can be seen that when one device is used, BER value is $\sim 10^{-3}$ at $E_b/N_0 = 10$ dB and for the same E_b/N_0 BER is increased to $\sim 10^{-2}$ when the number of devices is increased to five. Thus increase in number of devices causes increase of multiaccess interference power which leads to increase of BER. Thus, we have validated that an increase in the number of devices induces the performance degradation of PPM TH-ZCZ UWB/MIMO system in WBAN environment.

We have considered images as input to the proposed system shown in Figure 2 which can be used in telemedicine application. Figure 9(a) shows the inputs of biomedical Image which are given to the proposed system. Figure 9(b) shows noisy images obtained after passing through WBAN channel. Figure 9(c) shows the detected images using improved successive interference cancellation for MIMO/UWB-based body area network with m-ZCZ codes.

Figure 10 shows the histogram when biomedical images are given for PPM TH-ZCZ UWB/MIMO (2×2) system with 4, 2, and 1 devices in WBAN channel (CM4). From the figure, it can be seen that when one device is used, PSNR value is 30.2 and for the four devices PSNR value decreases to 22.5. Thus as number of devices increases, the PSNR value decreases due to increase in multiaccess interference.

6. Conclusion

In this paper, an improved successive interference cancellation scheme for MIMO/UWB-based wireless body area network is proposed. Proposed system utilizes ZCZ sequences as a spreading sequence. To mitigate interdevice interference in body area network successive interference cancellation with optimal ordering is used. TH PPM modulation followed by MMSE equalization is employed. From the simulation results, it can be seen that TH PPM-ZCZ UWB system gives

better BER performance than that of existing TH PPM without ZCZ, PAM-DS-PN, and PAM-DS-ZCD because of good cross-correlation properties. Also ZCZ codes have been compared with various other codes such as PN, ZCD codes for UWB/MIMO (2×2) system for different code lengths. Finally simulation results are validated using sample biological functions as input to the proposed TH PPM-ZCZ UWB/MIMO (2×2) system in WBAN environment with multiple devices.

Acronyms

3GPP:	Third generation partnership project
BAN:	Body area network
BER:	Bit error rate
ECG:	Electrocardiogram
EEG:	Electroencephalogram
MIMO:	Multiple input multiple-output
MAI:	Multiple access interference
PAM:	Pulse amplitude modulation
PPM:	Pulse position modulation
SIC:	Successive interference cancellation
SNR:	Signal-to-noise ratio
ZCD:	Zero correlation duration
UWB:	Ultrawide band
ZCZ:	Zero correlation zone
ZF-OSIC:	Zero forcing-optimal successive interference.

References

- [1] C. S. Pattichis, E. Kyriacou, S. Voskarides, M. S. Pattichis, R. Istepanian, and C. N. Schizas, "Wireless telemedicine systems: an overview," *IEEE Antennas & Propagation Magazine*, vol. 44, no. 2, pp. 143–153, 2002.
- [2] S. Tachakra and R. Istepanian. K. Banistas, "Mobile E-Health: the unwired evolution of telemedicine," in *Proceedings of HealthCom: Enterprise Networking and Computing in the Healthcare Industry*, 2001.
- [3] V. kaur and J. Malhotra, "Performance evaluation of M-ary modulations through WBAN channel," *International Magazine on Advances in Computer Science and Telecommunications*, vol. 2, no. 1, pp. 21–25, 2011.
- [4] J. Bernhard, P. Nagel, J. Hupp, W. Strauss, and T. von der Gruen, "BAN-body area network for wearable computing," in *Proceedings of the 9th Wireless World Research Forum (WWRF '03)*, Zurich, Switzerland, July 2003.
- [5] D. Porcino and W. Hirt, "Ultra-wideband radio technology: potential and challenges ahead," *IEEE Communications Magazine*, vol. 41, no. 7, pp. 66–74, 2003.
- [6] M. Z. Win and R. A. Scholtz, "Characterization of ultra-wide bandwidth wireless indoor channels: a communication-theoretic view," *IEEE Journal on Selected Areas in Communications*, vol. 20, no. 9, pp. 1613–1627, 2002.
- [7] J. N. Bae, Y. H. Choi, J. Y. Kim, J. W. Kwon, and D. I. Kim, "Efficient interference cancellation scheme for wireless body area network," *Journal of Communications and Networks*, vol. 13, no. 2, pp. 167–174, 2011.
- [8] M. Jayasheela and A. Rajeswari, "Performance of CDMA system using m-ZCZ sequences," in *Proceedings of 5th International ICST Mobile Multimedia Communications Conference (MOBIMEDIA '09)*, ACM, 2009.

Research Article

Design of a Wearable, Low-Cost, Through-Wall Doppler Radar System

**Sam Agneessens,¹ Patrick Van Torre,^{1,2} Frederick Declercq,¹ Bart Spinnewyn,¹
Gert-Jan Stockman,¹ Hendrik Rogier,¹ and Dries Vande Ginste¹**

¹Department of Information Technology, Ghent University, Sint-Pietersnieuwstraat 41, 9000 Ghent, Belgium

²INWE Department, Hogeschool Gent, Schoonmeersstraat 52, 9000 Ghent, Belgium

Correspondence should be addressed to Sam Agneessens, sam.agneessens@intec.ugent.be

Received 24 February 2012; Accepted 16 June 2012

Academic Editor: C. Aanandan

Copyright © 2012 Sam Agneessens et al. This is an open access article distributed under the Creative Commons Attribution License, which permits unrestricted use, distribution, and reproduction in any medium, provided the original work is properly cited.

A novel, low-cost, low-weight, wearable Doppler radar system composed of textile materials and capable of detecting moving objects behind a barrier is presented. The system operates at 2.35 GHz and is integrable into garments, making it well-suited for usage in difficult to access terrain, such as disaster areas or burning buildings. Wearability is maximized by relying on flexible, low-weight, and breathable materials to manufacture the key parts of the system. The low-complexity Doppler radar system makes use of an array of four textile-transmit antennas to scan the surroundings. The beam emitted by this array is right-hand circularly polarized along all scanning angles and provides a measured gain of 9.2 dBi. At the receiving end, textile materials are used to develop an active wearable receive antenna, with 15.7 dBi gain, 1.1 dB noise figure, left-hand circular polarization, and a 3 dB axial ratio beamwidth larger than 50°. Several measurement setups demonstrate that the onbody system is capable of detecting multiple moving subjects in indoor environments, including through-wall scenarios.

1. Introduction

By integrating textile antennas into garments, low-weight, wearable, wireless systems can be created. These systems have the advantage that they are comfortable to wear and do not limit the user's ability to move. Such systems can be deployed to gather environmental (air humidity, temperature) or biometric data (heart rate, respiratory data), to provide information about the user's location (GPS), to inform the user about hazardous situations, and so forth.

An important field in which such systems can be deployed is security and rescue applications. The potential to detect and track human movers through walls and closed doors is an interesting feature for security, surveillance, and rescue systems [1]. Such an ability can be used to localize survivors after a natural disaster or accidents (e.g., an earthquake, people in a burning building) or to provide information about the position and number of criminals or hostile forces in an urban area.

For deployment during rescue operations, it is vital that the through-wall radar system is low-weight, compact, and comfortable to wear [2]. The user's motions should not be hindered and the extra effort of transporting the system should remain minimal. Therefore, the primary motivation for this paper was to design a low-weight, wearable, through-wall radar system. It makes use of textile materials to manufacture a passive transmit array, scanning the surroundings, combined with an active receive antenna. Textile materials make the system breathable, flexible, and well-suited for integration into garments.

Extensive research has been performed to develop through-wall radars and comprehensive documentation about the state-of-the-art can be found in the literature. Systems relying on Synthetic Aperture Radar (SAR) imaging focus on the emulation of a larger aperture by moving a small antenna to enhance the system resolution [3, 4]. Others are based on multipoint sensors or arrays and exploit the different viewing angles of these antennas in order to

compose the image [5]. These systems are often heavy, large, and energy consuming, which requires them to be vehicle-mounted, making them unsuited for practical use in difficult to access terrain, such as disaster areas or burning buildings [2]. Other systems that are designed to be limited in size and weight [6, 7] still suffer from the problem that they require the user to carry around an extra piece of equipment. This hinders the person's movement and leads to extra gear in situations where agility is key.

Adopting textile antennas in wireless systems is gaining importance. Several case studies indicate that they are well-suited, as mobile phone antennas, for space applications or in wireless communication links [8–10], as they offer good performance, comparable to conventional antennas, combined with interesting properties such as low-weight, low-cost, and high level of integrability into garments [11]. They can be deployed in a similar fashion as conventional antennas, allowing to construct arrays [12, 13] or active antennas [14].

In this paper a novel low-weight, highly integrable, wearable radar system capable of detecting moving objects behind a barrier, such as a closed door, is designed, manufactured, and thoroughly tested. Thereto several important design choices have been made, specifically the following.

- (i) The scanning of the environment is performed by a right-hand circularly polarized transmit array manufactured using materials commonly found in firefighter garments.
- (ii) An active textile antenna is deployed at the receiver end of the system. This active antenna is left-hand circularly polarized to minimize mutual coupling between transmitter and receiver and to reduce the negative influence of multipath. Furthermore, the integrated low-noise amplifier (LNA) increases the system's overall sensitivity.
- (iii) Beam scanning is implemented by means of power dividers, electronic phase shifters, and a microcontroller. The circuit composed by these elements may be implemented on a flexible polyimide substrate, directly integrated behind the transmit array or active antenna.

The paper is organized as follows. First, the global radar system is discussed in Section 2. The principle of operation and design choices are explained, as well as the layout of the beamforming circuit. Special attention is devoted to (i) the possibilities of integrating this circuit behind the array in order to further increase the system's wearability and (ii) the time-multiplexed measurement methodology. Section 3 is dedicated to the design criteria and development of the textile antennas: a right-hand circularly polarized transmit array and an active receive antenna, based on [14], with the additional feature of being left-handed circularly polarized. In Section 4, the simulation and measurement results are presented. The performance of the textile antennas is validated and the radar system is thoroughly tested. The system is shown to be capable of detecting multiple targets behind a closed door in a free-space and an off-body setup.

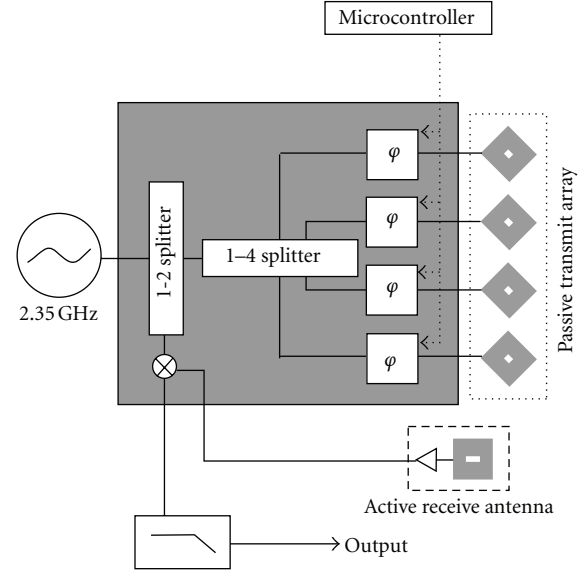


FIGURE 1: Block diagram of the wearable radar system.

2. Radar System

Textile antennas have a large number of applications. Here, they are used as the key component in the design of a low-cost, wearable, through-wall Doppler radar system. The system leverages passive and active textile antennas, that are highly integrable, making them very well-suited for a wearable radar system. To limit the system's power consumption and overall complexity, a simple Doppler architecture is deployed and data processing is kept to a minimum. Figure 1 shows the block diagram of the designed through-wall radar. The transmit side relies on a phased array of four RHCP (right-hand circularly polarized) passive antennas to electronically scan the surroundings. Steering of the beam is implemented by a beamforming circuit composed of phase shifters (JSPHS-2484+), a power divider (BP4U+), and a microcontroller, all from Mini-Circuits [15]. At the receiving end, an LHCP (left-hand circularly polarized) active antenna is used to detect the reflected signal. This signal is demodulated by a mixer (ADE-35+ from Mini-Circuits) and low-pass (LP) filter in order to extract the Doppler shift, which is then processed by a portable computer. The chosen polarizations eliminate the direct path between the transmit and receive antennas, reject second-order reflections, and minimize the influence of multipath. The system transmits a continuous wave signal at a frequency of 2.35 GHz, avoiding interference from the 2.45 GHz ISM band, providing good wall penetration [16, 17] and keeping losses in the textile materials acceptable.

The beamforming circuit is composed of the above described, small, low-weight SMT-components and, in this proof-of-principle design, it is realized on a rigid FR4 substrate. The choice for an FR4 substrate allows for easy measurement and testing during the development phase. Obviously, overall flexibility and wearability of the system

can easily be further improved by implementing the small-footprint circuits together with the passive interconnects on a flexible substrate. Polyimide is very well-suited for this goal, since it is a thin, low-weight, flexible substrate material that can be glued on top of a fabric layer, placed behind the ground plane of the transmit array or receive antenna. Integration of the beamforming circuit underneath the ground plane keeps the overall surface of the system small, limits the length of the interconnects—and related losses—and reduces parasitic coupling by shielding the circuit from electromagnetic radiation. This method of realizing an electronic circuit onto a hybrid polyimide-textile substrate underneath an antenna is adopted later in this paper (Section 3.2) to manufacture the active receive antenna.

Detection of moving targets is performed by adopting a time multiplexing approach. The surroundings are scanned by the transmit array at a discrete number of directions. This scanning occurs at high speed, that is, the period of a single sweep is small compared to the period of the received Doppler signal. During each sweep, the Doppler signal is sampled, each sample corresponding to a discrete transmit angle. By combining the samples of the subsequent scans for each of the directions, waveforms are formed. Each waveform corresponds to the received signal from a single direction and it is as if all the different directions are scanned “simultaneously.” The sweep frequency and number of discrete sampling angles limit the maximal detectable Doppler shift. For detection of walking humans, this upper frequency does not cause problems, since the Doppler shift remains sufficiently low.

3. Antenna Design

A wearable radar system requires antennas that are constructed using light-weight, breathable, and flexible materials. The materials proposed below are commonly found in firefighter garments, which makes them very well-suited for the intended application. Both receive and transmit antennas are based on a rectangular ring topology with a coaxial feed [18]. This results in antennas that are easy to construct and allows obtaining circular polarization by means of a single feedpoint. Circularly polarized antennas have a number of very useful properties for the design of a radar system, such as increased isolation between receiver and transmitter and easy rejection of unwanted reflections, which makes the system less sensitive to the negative influence of multipath.

3.1. Transmit Array. The textile antenna array consists of identical rectangular ring patch antennas. The conducting patch and ground plane of the antenna elements are fabricated by means of Flectron, a copper-plated nylon fabric, with a surface resistivity of $R_s = 0.176 \Omega/\text{sq}$ at 2.35 GHz. A polyurethane protective foam manufactured by Brunet Lion for use in firefighter suits, called Azzurri, is applied as substrate material. It has a thickness of 3.55 mm, permittivity $\epsilon_r = 1.19$, and loss tangent $\tan \delta = 0.003$. These antennas need to be circularly polarized and matched to the 50 Ω signal source, so it is required that their individual axial ratio

and reflection coefficient remain below 3 dB and -10 dB, respectively.

The array itself is a phased array, this allows for simple and power-efficient beamforming. This transmit array must provide sufficient gain and an almost constant beam width for the different scanning angles. In order to fix the number of array elements, a tradeoff was made between high directivity and low side lobes on one hand and available space and low mutual coupling between elements on the other hand. An isolation between the elements of 20 dB is enforced. The last design criterion for the array is a constant RHCP polarization while scanning. This requires that the emitted radiation remains RHCP in the direction of maximal gain of the steered beam.

Based on these criteria, a four-element uniform linear array was designed, whose geometry and dimensions are presented in Figure 2 and Table 1. Spacing between the elements is 8.5 cm, providing an array with an aperture of 33 cm allowing it to be fitted onto a human wearer’s chest Figure 11.

3.2. Active Receive Antenna. The active receive antenna consists of a rectangular ring patch connected directly, without matching networks, to an LNA underneath its ground plane. This design approach avoids losses in components pertaining to the matching network and keeps interconnect losses low, as these degrade overall system noise performance and, hence, radar sensitivity. The radar system requires the LNA to have good noise performance, while maintaining sufficient gain. The active receive antenna as a whole should be LHCP to increase isolation between transmitter and receiver and to minimize the negative influence of second-order reflections and multipath on the system’s performance. To achieve this, following design strategy is adopted: first, a suitable LNA design is selected, providing good noise performance and sufficient amplifier gain. In the next step, the antenna parameters are adapted to realize LHCP and the impedance required by the LNA for optimal noise performance.

For the LNA an ATF-54143 + e-PHEMT from Avago technologies is applied as the active element in a grounded source topology [19]. The LNA substrate is multilayered. The copper footprint is etched onto a 25 μm polyimide film, that is, glued on top of an Aramid layer ($\epsilon_r = 1.686$, $\tan \delta = 0.015$) of 400 μm . This design provides a stable LNA with sufficient gain and linearity as well as a low noise figure.

Similar to the passive transmit array, the antenna substrate is polyurethane foam and the ground plane and patch are again manufactured relying on Flectron. Antenna and LNA share this common ground plane through which both are connected by a feed line. The geometry of this active antenna is displayed in Figure 3 and Table 1 presents the antenna dimensions.

The design criteria for this receive antenna need to be met in a band around the frequency of the transmitted wave. The width of this band depends on the Doppler shift produced by a moving object (or person in this case). If the maximal velocity is assumed to be 6 m/s [20], this Doppler shift remains well below 1 kHz and the design criteria—good noise performance, ample gain and LHCP—only need to be

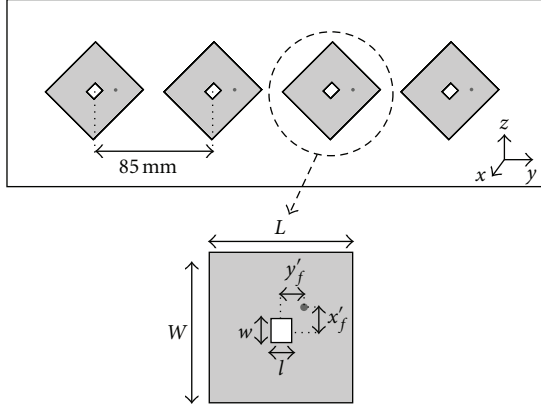


FIGURE 2: Geometry of the passive transmit array.

met in a very small band around the central frequency of 2.35 GHz.

4. Simulations and Measurements

4.1. Transmit Array. First, the transmit array is characterized in terms of its scattering parameters. Figure 4 shows the simulated and measured reflection coefficient for an antenna element at the edge of the array and the isolation to its direct neighbor. At 2.35 GHz, the reflection coefficient $|S_{11}|$ of the displayed antenna is smaller than -10 dB, indicating that the antenna elements are matched to the 50Ω signal source. The measured mutual coupling $|S_{21}|$ between the elements is lower than -20 dB, confirming that the isolation between these two elements is sufficiently high. The simulated and measured results for the other array elements are similar to the results shown in Figure 4.

The array radiation pattern is another important parameter of the system, as variation in the gain pattern's main lobe, deformation of the beam and size of the sidelobes have a large influence on its performance (e.g., the maximal obtainable scanning resolution). Figure 5 presents the simulated and measured gain pattern when the main lobe of the beam is steered along 0° in the azimuth plane, that is, the XY -plane (Figure 2). The patterns show a large degree of resemblance, but the measured gain value of 9.2 dBi is smaller than the simulated gain of 13.8 dBi. This is due to the fact that the simulation does not take the losses in the steering circuit and the insertion loss of the phase shifters, which were measured to add up to 3.9 dBi for a 0° steering angle, into account. The measured 3 dB half beamwidth is 9° and remains constant along all considered steering angles.

The phase shifters limit the maximal angle along which the beam can be steered, without large deformation in shape. The steering angle of the beam ranges from -15° to $+15^\circ$ and Figure 6 shows the measured gain pattern for the steering angles -10° , 0° and 15° . The highest measured sidelobe gain is about 2 dBi when the beam is steered along an angle of $\pm 15^\circ$, resulting in a sidelobe suppression of 7 dB, which is important in avoiding "ghost echoes." The detection range can be further augmented by cascading the used phase

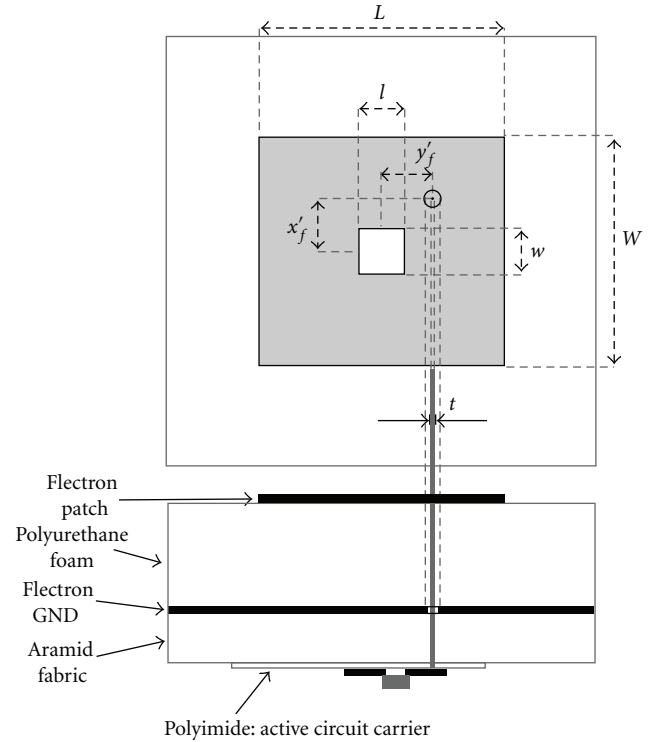


FIGURE 3: Geometry of the active receive antenna.

TABLE 1: Dimensions of the individual transmit array elements and active receive antenna element.

	Array element	Active antenna
W	51.8 mm	49.5 mm
L	55.4 mm	51 mm
w	8.8 mm	17.5 mm
l	7.5 mm	7 mm
x'_f	7.4 mm	8 mm
y'_f	10.1 mm	-5 mm
t	1.25 mm	0.85 mm

shifters. Simulations indicate that the deformation of the beam at a maximal steering angle of $\pm 30^\circ$ remains low and a side lobe suppression larger than 8.5 dB, so the scanning range may be increased to cover -30° to $+30^\circ$ without system performance loss.

Another important feature of the system is the polarization of the beam. Figure 7 visualizes the measured axial ratio for different steering angles. It can be seen that the array remains RHCP along all these angles.

4.2. Active Receive Antenna. The active receive antenna is designed to have an impedance matched to the simulated optimal noise impedance of the LNA, that is, $(35.7 - j15.7) \Omega$, to maximize the noise performance. This antenna without LNA has a measured gain, G_p , in the main direction of 7.3 dBi. The simulated and measured gain pattern, G_{tot} , and axial ratio of the active receive antenna are shown in Figure 8. The maximal simulated and measured gain is 18.6 dBi and

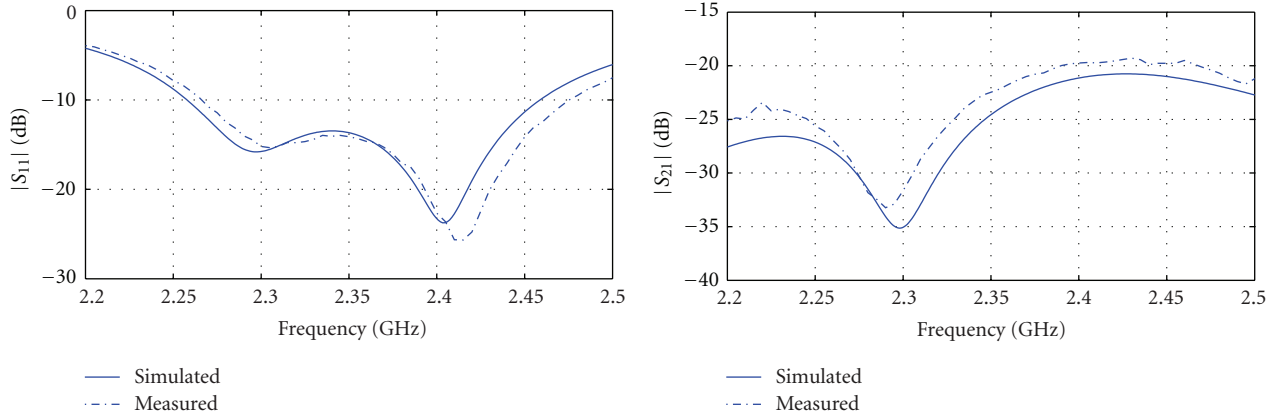


FIGURE 4: Simulated (full line) and measured (dashed-dotted line) reflection coefficient of a single element and mutual coupling between two neighboring array elements.

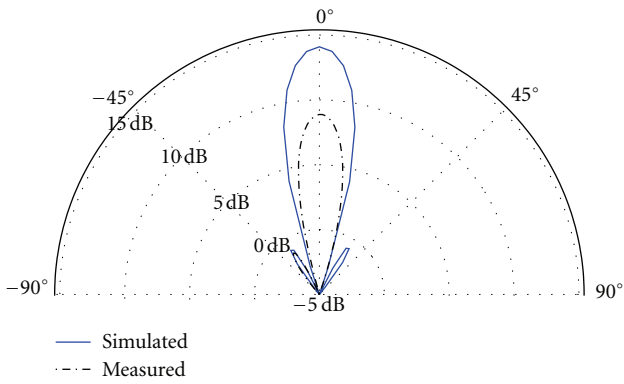


FIGURE 5: Simulated (full line) and measured (dashed-dotted line) gain pattern in the azimuth plane, that is, the XY-plane (Figure 2), for an array with main lobe steered along 0°.

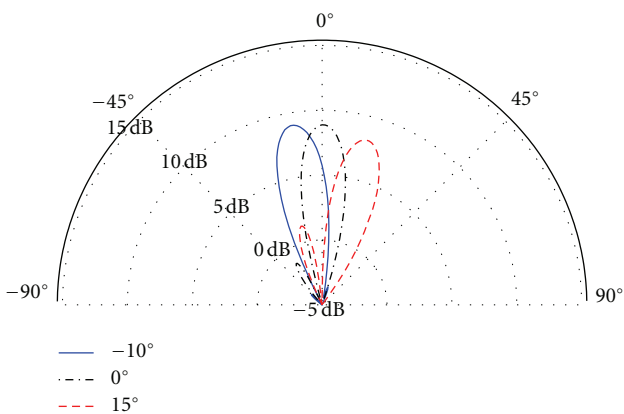


FIGURE 6: Radiation pattern in the azimuth plane with direction of maximal gain at -10°, 0°, and 15°.

15.7 dBi, respectively. The measured 3 dB beamwidth in terms of gain exceeds 60° and the 3 dB axial ratio beamwidth in terms of circular polarization is larger than 50°. The discrepancies in gain and axial ratio between measurements

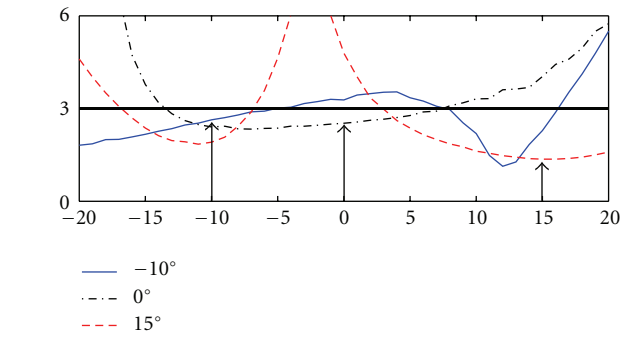


FIGURE 7: Axial ratio for radiation patterns in the azimuth plane with direction of maximal gain at -10°, 0°, and 15°.

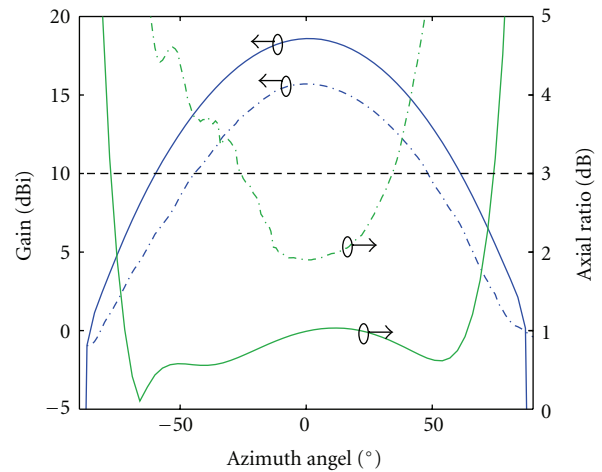


FIGURE 8: Simulated (full line) and measured (dashed-dotted line) total gain and axial ratio for the active receive antenna.

and simulations evolve from the manual manufacturing process and misalignments during the measurements.

The LNA is unconditionally stable and, when attached to the receive antenna, exhibits a simulated transducer gain

of 11.3 dB and a noise figure of 0.9 dB at the operating frequency of 2.35 GHz when attached to the receive antenna. The actual transducer gain, G_t of the LNA cannot be measured directly, due to the integration into the active antenna, but it can be deduced from following relation:

$$G_{\text{tot}}(\theta, \phi) = G_p(\theta, \phi)G_T, \quad (1)$$

where $G_{\text{tot}}(\theta, \phi)$ is the measured gain of the active antenna and $G_p(\theta, \phi)$ is the measured gain of a passive antenna with identical dimensions. This leads to $G_t = 8.1$ dB. With the knowledge of G_t it is possible to calculate the noise factor by measuring the noise power density P_n referred to 290 K [21]:

$$F = 1 + \frac{P_n}{G_t} - \frac{T_a}{290}, \quad (2)$$

with T_a the effective noise temperature (286.3 K). The noise figure measured in an anechoic chamber at 2.35 GHz is 1.1 dB, which is in good agreement with the simulations.

In summary, the performance of the active antenna is outstanding, making it ideal for usage as a receive antenna in the radar system.

4.3. Radar System. To validate the radar's performance, a series of measurements are conducted. First, they are carried out with the radar in a free-space environment, that is, without the presence of a human body. Next, the system is worn by a person. For both configurations, two series of measurements are performed. First, loudspeakers producing an audio tone at a fixed frequency are detected, as this yields stable and repeatable results. Next, human subjects are used as moving targets.

4.3.1. Free-Space Measurements. The transmitter and receiver are placed in free-space at a distance of approximately 20 cm apart from each other. As such, the measured isolation between them is larger than 40 dB, which is sufficient for the radar system to function properly. This low coupling avoids saturation of the active antenna amplifier by the power of the transmitted wave, which is 5 dBm.

The first experiment uses a single speaker, producing a fixed tone at a low frequency (10 Hz), so that the movement of the cone is large enough to measure. The speaker is placed along a 0° azimuth angle, 3 m away from the radar and the cone is covered by copper tape to increase the reflections. The received spectrum for each angle is visualized in Figure 9. The 10 Hz peak is clearly visible at 0° and only noise is received along the other scanned angles.

Figure 10 shows the frequency spectrum for the second experiment. There are two different targets: a person approaches the radar at the 0° angle and a speaker is placed at the -15° angle, now producing a 15 Hz tone. The human target is detected at a peak frequency of 24 Hz, which corresponds to a normal walking velocity of 1.5 m/s. The speaker is picked up at -15° . There is also a smaller "ghost echo," originating from the sidelobes of the scanning beam at 15° .

4.3.2. On-Body Measurements. The influence of the wearer on the system's ability to detect targets behind a closed

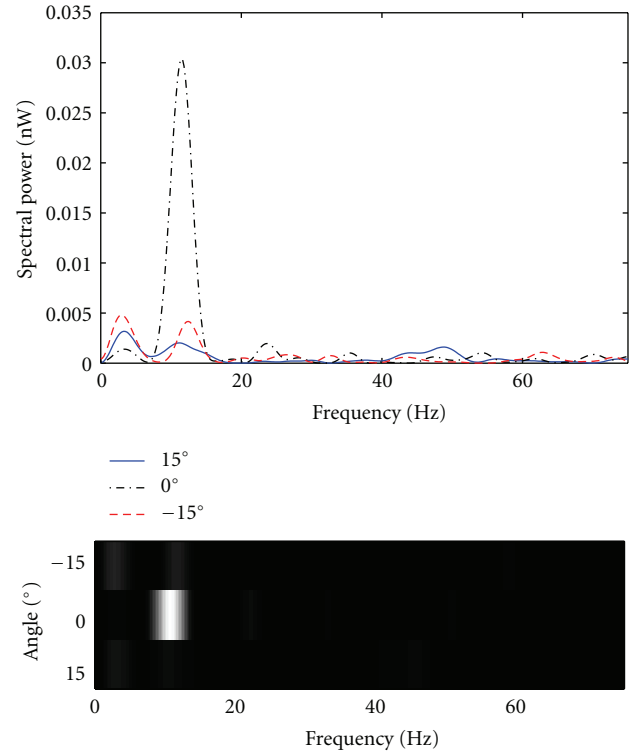


FIGURE 9: Spectrogram of the received signal when a speaker, producing a 10 Hz tone, is placed at 0° .

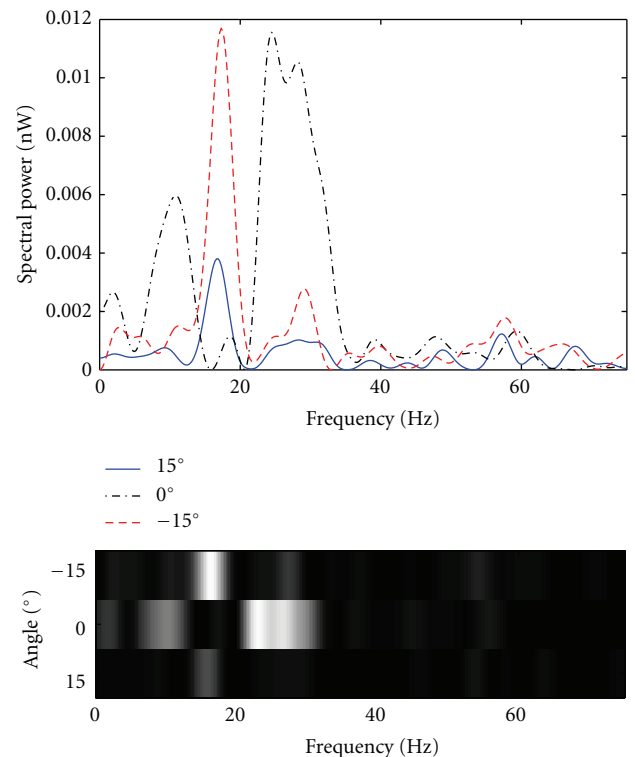


FIGURE 10: Spectrogram for a person walking towards the radar at a 0° angle and a speaker placed at -15° (15 Hz).

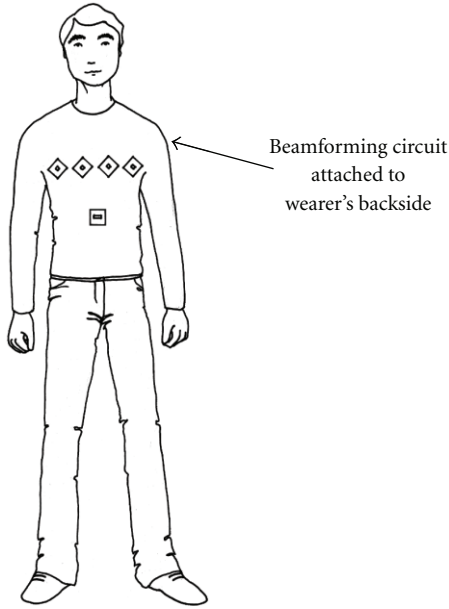


FIGURE 11: Textile radar system positioned on a human wearer (drawing by Laura Goethals).

wooden door, covered by fire retardant paint, is analyzed. Figure 11 gives a representation of how the system is positioned on a human wearer. The array is attached onto the user's chest in order to minimize the deformation of the array and the active antenna is placed below it at a large enough distance in order to limit mutual coupling between transmitter and receiver. The beamforming circuit is attached to the back of the suit.

The person wearing the radar is separated from the target by a barrier, in our experiment a closed wooden door. The targets used in the experiments consist of a speaker producing a 15 Hz tone placed at approximately 1.5 m and a person walking towards the radar at the other side of the door. The frequency spectra measured during these tests are shown in Figure 12 (speaker) and Figure 13 (person), respectively. The results are similar to the free-space experiments, the frequency components related to the movement of the speaker and human target are clearly visible. This indicates that the system performance is not significantly reduced when deployed onto a human wearer and that detection remains possible even in the presence of a barrier, such as a door or a wall, between the radar and the moving object.

Deploying the radar on the human body as described in this paper limits the region where objects can be detected to the frontal hemisphere. However, certain cases may require the wearer to have knowledge of what is happening behind him/her. The time-multiplexed scanning method allows simple extension of the detection area, to include the backward hemisphere, by the addition of an extra transmit array and receiver antenna at the rear of the observer, but without the need of extra data processing hardware. This extended detection range comes at the cost of additional scanning angles and may require an increase of scanning and sampling frequency to maintain a usable (i.e., high enough)

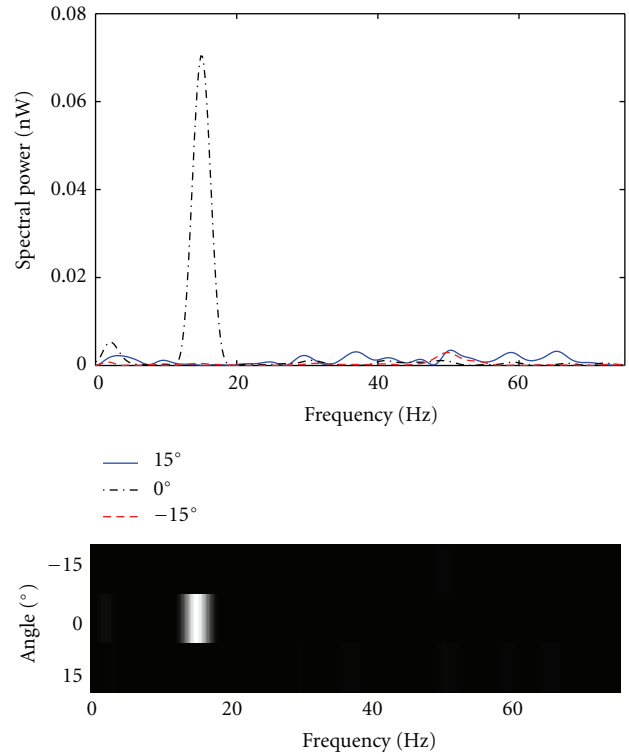


FIGURE 12: Spectrogram for a speaker at distance of 1.5 m, producing a 15 Hz tone behind a closed door when the radar is deployed on the human body.

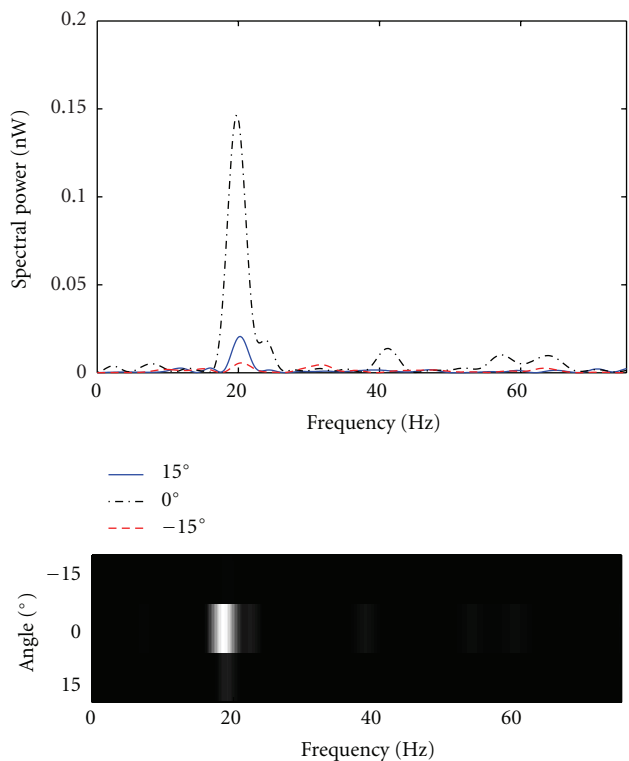


FIGURE 13: Spectrogram for a person walking towards the observer behind a closed door when the radar is deployed on the human body.

maximal detectable Doppler shift. A system which relies on such a front and back array to increase its performance is presented in [22].

5. Conclusions and Future Research

A novel low-weight, wearable radar system, capable of detecting moving human subjects behind a barrier, such as a door, a wall, or debris of a building, was proposed.

Wearability is maximized by using textile materials to manufacture the receive and transmit antennas. The RHCP transmit array allows to scan the environment and maintain a circular polarization along all steering angles. The system sensitivity is enhanced by using an LHCP active receive antenna, optimized for noise performance. Using opposite antenna polarizations enhances the isolation between receiver and transmitter, allows for easy rejection of second-order reflections and minimizes the unwanted effects of multipath. Furthermore, the beamforming circuit is small and can easily be realized on a flexible substrate, such as polyimide, which can be glued behind the array to improve wearability and to limit the system's size. The extensive use of breathable, low-weight and flexible materials in the design of this radar system makes it very well-suited to be integrated into garments worn by rescue workers, firefighters, or law enforcement personnel operating in rough, difficult to access, or hazardous terrain.

The main individual components of the radar system, that is, the transmit array and active receive antenna, as well as the system itself, have been thoroughly tested, validating the design. The main novelty and focus of this work is, however, the wearability of the system and it was a deliberate design choice to keep the radar data processing simple and power-efficient.

Better performance can easily be obtained by more extensive data processing or the work can be taken as a starting point for a wearable radar system with imaging techniques. Further study including measurements in scenarios where the targets are behind multilayered structures, such as concrete or composite walls, is needed to further characterize the system's performance as a through-wall radar system. Such future work can also include the study of the system's performance when it is worn in more dynamic situations which may cause more bending or deformations of the transmit array and receiver antenna (e.g., crouching).

References

- [1] E. J. Baranoski, "Through-wall imaging: historical perspective and future directions," *Journal of the Franklin Institute*, vol. 345, no. 6, pp. 556–569, 2008.
- [2] M. Farwell, J. Ross, R. Luttrell, D. Cohen, W. Chin, and T. Dogaru, "Sense through the wall system development and design considerations," *Journal of the Franklin Institute*, vol. 345, no. 6, pp. 570–591, 2008.
- [3] F. Ahmad and M. G. Amin, "Multi-location wideband synthetic aperture imaging for urban sensing applications," *Journal of the Franklin Institute*, vol. 345, no. 6, pp. 618–639, 2008.
- [4] M. Dehmollaian and K. Sarabandi, "Refocusing through building walls using synthetic aperture radar," *IEEE Transactions on Geoscience and Remote Sensing*, vol. 46, no. 6, pp. 1589–1599, 2008.
- [5] F. Ahmad, M. G. Amin, and G. Mandapati, "Autofocusing of through-the-wall radar imagery under unknown wall characteristics," *IEEE Transactions on Image Processing*, vol. 16, no. 7, pp. 1785–1795, 2007.
- [6] K. Browne, R. Burkholder, and J. Volakis, "Through-wall radar imaging system utilizing a light-weight low-profile printed array," in *Proceedings of the 4th European Conference on Antennas and Propagation (EuCAP '10)*, pp. 12–16, IEEE, Barcelona, Spain, April 2010.
- [7] S. S. Ram and H. Ling, "Through-wall tracking of human movers using joint doppler and array processing," *IEEE Geoscience and Remote Sensing Letters*, vol. 5, no. 3, pp. 537–541, 2008.
- [8] P. J. Massey, "Mobile phone fabric antennas integrated within clothing," in *Proceedings of the 11th International Conference on Antennas and Propagation*, no. 480, pp. 17–20, Manchester, UK, April 2001.
- [9] T. Kennedy, P. Fink, A. Chu, and G. Studor, "Potential space applications for body-centric wireless and E-textile antennas," in *Proceedings of the Institution of Engineering and Technology Seminar on Antennas and Propagation for Body-Centric Wireless Communications*, pp. 77–83, The Institution of Engineering and Technology, London, UK, April 2007.
- [10] M. Klemm and G. Troester, "Textile UWB antennas for wireless body area networks," *IEEE Transactions on Antennas and Propagation*, vol. 54, no. 11, pp. 3192–3197, 2006.
- [11] C. Hertleer, H. Rogier, L. Vallozzi, and L. van Langenhove, "A textile antenna for off-body communication integrated into protective clothing for firefighters," *IEEE Transactions on Antennas and Propagation*, vol. 57, no. 4, pp. 919–925, 2009.
- [12] T. F. Kennedy, P. W. Fink, A. W. Chu et al., "Body-worn E-textile antennas: the good, the low-mass, and the conformal," *IEEE Transactions on Antennas and Propagation*, vol. 57, no. 4, pp. 910–918, 2009.
- [13] M. L. Scarpello, D. Vande Ginste, and H. Rogier, "Design of a low-cost steerable textile antenna array operating in varying relative humidity conditions," *Microwave and Optical Technology Letters*, vol. 54, no. 1, pp. 40–44, 2012.
- [14] F. Declercq and H. Rogier, "Active integrated wearable textile antenna with optimized noise characteristics," *IEEE Transactions on Antennas and Propagation*, vol. 58, no. 9, pp. 3050–3054, 2010.
- [15] <http://www.minicircuits.com/>.
- [16] M. Amin and K. Sarabandi, "Special issue on remote sensing of building interior," *IEEE Transactions on Geoscience and Remote Sensing*, vol. 47, no. 5, pp. 1267–1268, 2009.
- [17] T. B. Gibson and D. C. Jenn, "Prediction and measurement of wall insertion loss," *IEEE Transactions on Antennas and Propagation*, vol. 47, no. 1, pp. 55–57, 1999.
- [18] G. Vermeeren, H. Rogier, F. Olyslager, and D. de Zutter, "Low-cost planar rectangular ring antenna for operation in HiperLAN band," *Electronics Letters*, vol. 38, no. 5, pp. 208–209, 2002.
- [19] ATF-54143, "High Intercept Low Noise Amplifier for the 1850-1910 MHz PCS Band using the Enhancement Mode PHEMT," Application Note 1222, Avago Technologies, 2006.
- [20] S. S. Ram, Y. Li, A. Lin, and H. Ling, "Doppler-based detection and tracking of humans in indoor environments," *Journal of the Franklin Institute*, vol. 345, no. 6, pp. 679–699, 2008.

- [21] H. An, B. Nauwelaers, A. R. van de Capelle, and R. G. Bosisio, "A novel measurement technique for amplifier-type active antennas," in *Proceedings of the IEEE MTT-S International Microwave Symposium Digest*, vol. 3, pp. 1473–1476, San Diego, Calif, USA, May 1994.
- [22] P. van Torre, L. Vallozzi, H. Rogier, and J. Verhaevert, "Indoor off-body wireless communication using static zero-elevation beamforming on front and back textile antenna arrays," in *Proceedings of the 6th European Conference on Antennas and Propagation (EuCAP '12)*, Prague, Czech Republic, March 2012, Convened Session "Recent Advances and Applications of Body-Centric Wireless Communications".

Research Article

Performance of Ultrawideband Wireless Tags for On-Body Radio Channel Characterisation

Mohammad Monirujjaman Khan,^{1,2} Qammer H. Abbasi,¹ Akram Alomainy,¹ and Yang Hao¹

¹ School of Electronic Engineering and Computer Science, Queen Mary University of London, London E1 4NS, UK

² Department of Electrical and Electronic Engineering, American International University-Bangladesh, Dhaka 1213, Bangladesh

Correspondence should be addressed to Mohammad Monirujjaman Khan, mohammad.khan@elec.qmul.ac.uk

Received 16 February 2012; Accepted 21 June 2012

Academic Editor: C. Aanandan

Copyright © 2012 Mohammad Monirujjaman Khan et al. This is an open access article distributed under the Creative Commons Attribution License, which permits unrestricted use, distribution, and reproduction in any medium, provided the original work is properly cited.

Experimental characterisation of on-body radio channel for ultrawideband (UWB) wireless active tags is reported in this paper. The aim of this study is to investigate the performance of the commercially available wireless tags on the UWB on-body radio channel characterisation. Measurement campaigns are performed in the chamber and in an indoor environment. Statistical path loss parameters of nine different on-body radio channels for static and dynamic cases are shown and analyzed. Results demonstrated that lognormal distribution provides the best fits for on-body propagation channels path loss model. The path loss was modeled as a function of distance for 34 different receiver locations for propagation along the front part of the body. A reduction of 11.46% path loss exponent is noticed in case of indoor environment as compared to anechoic chamber. In addition, path loss exponent is also extracted for different body parts (trunk, arms, and legs). Second-order channel parameters as fade probability (FP), level crossing rate (LCR), and average fade duration (AFD) are also investigated.

1. Introduction

Ultrawideband (UWB) communication is an exciting and innovative technology that has attracted much attention and experienced considerable growth in the past few years due to its distinctive characteristics. It is a low-power, high data rate technology that minimizes multipath interference due to late time-of-arrival. Its low-power requirement due to control over duty cycle allows longer battery life and also introduces green radio system. One of the most potential areas of UWB applications is the body-centric wireless networks where various units/sensors are scattered on/around the human body to measure specified physiological data that is, patient monitoring for healthcare applications [1–3].

In the past few years researchers have been thoroughly investigating narrowband and ultrawideband on-body radio channels. In [4–7], on-body radio channel characterisation was presented at the unlicensed frequency band of 2.45 GHz. UWB on-body radio channel characterisation and system level modelling for body-centric wireless networks have been presented extensively in the open literature [2, 8–20].

In [8–20], UWB on-body propagation channels have been characterized, and their behaviour has been investigated in indoor and chamber for standstill, various postured and dynamic human body based on different antennas. Most UWB on-body channel measurements are performed using two standalone antennas and cables connecting to a vector network or spectrum analyzer which is more a controlled environment and restrictive; however, in real life scenarios potential UWB body-centric wireless network needs to be integrated with compact sensors and provides efficient and reliable communication channels. Critical issues remain with regards to indoor propagations, radio channel characterization, and human body effect which they need to be addressed before the concept can be deployed for commercial applications.

In this paper, measurement campaigns were performed in the chamber and indoor environment using commercially available UWB wearable active tags and reader. The main aim of this study is to investigate the performance of the commercially available wireless tags on the UWB on-body radio channel characterization. Nine different on-body radio

channels are investigated and the effects of the body movements on the path loss are analysed. Second-order statistics for three different on-body links are investigated. The results reported here provide information on optimum sensor locations on the body considering efficient and reliable communication links for various applications, for example, healthcare and performance monitoring.

The rest of the paper is organised as follows: Section 2 illustrates the measurement settings, and it briefly introduces the UWB tags, Sections 3 and 4 present the measurement results and on-body radio channel parameters and modelling aspects, and finally Section 5 draws the main conclusion of the presented study.

2. Measurement Settings

Measurement campaigns were performed using UWB wearable active tags and reader provided by time domain PLUS [21]. For this measurement purpose, a real human subject was used. The test subject was an adult male of mass 90 Kg, height 1.68 meter, and chest circumference 114 cm. Nine different ultrawideband wireless active transmitter tags were attached at different locations on the human body: left/right chest, left/right thigh, left wrist, left/right ankle, left elbow, and left ear, as shown in Figure 1, while the UWB antenna connected with the reader was placed on the left waist of the human subject for tag's signal reception. Two measurement scenarios are considered: static and dynamic human body. For static case, subject was standing still for a period of 60 seconds wearing nine tags on the body and, for the movement case, the subject was walking 5 steps ahead and 5 steps back, starting with the left leg and right arm as a normal walking speed. For the dynamic case, the measurement duration was again 60 seconds while the subject was doing the same walking movement for the measurement duration. Location-based software was used to save the tags transmission ID, received signal strength (RSSI), and time of arrival data from the reader. The UWB tags are battery powered, and the duration of the battery life is four years since the tags only transmit UWB pulses every one second. The tag's transmit power is -13.01 dBm which is around 40 dB less than mobile phone transmit power. The operating frequency of the tags used for this measurement is 5.9~7.25 GHz with a centre frequency of 6.6 GHz. The UWB tag is small and durable, with a plastic housing that allows it to be attached to assets or people. The dimension of the tag is (13 mm \times 36 mm \times 33 mm) and the weight is 0.74 oz (22 g). Figures 2(a), 2(b), and 2(c) show the UWB tag encased inside the plastic housing, the bottom view of the tag without plastic housing, and the top view of the tag showing the tag antenna [21]. The free space and on-body radiation patterns of the tag antenna at 6.6 GHz are measured in the anechoic chamber. The on-body radiation patterns are measured by placing the tag antenna on the same test subject as mentioned earlier. Figures 3(a) and 3(b) show comparison of free space and on-body radiation patterns (XY and YZ planes) at 6.6 GHz of the tag antenna. The tag antenna has monopole-like radiation patterns. When the tag is mounted on the body, the radiation pattern is omnidirectional over the surface (XZ

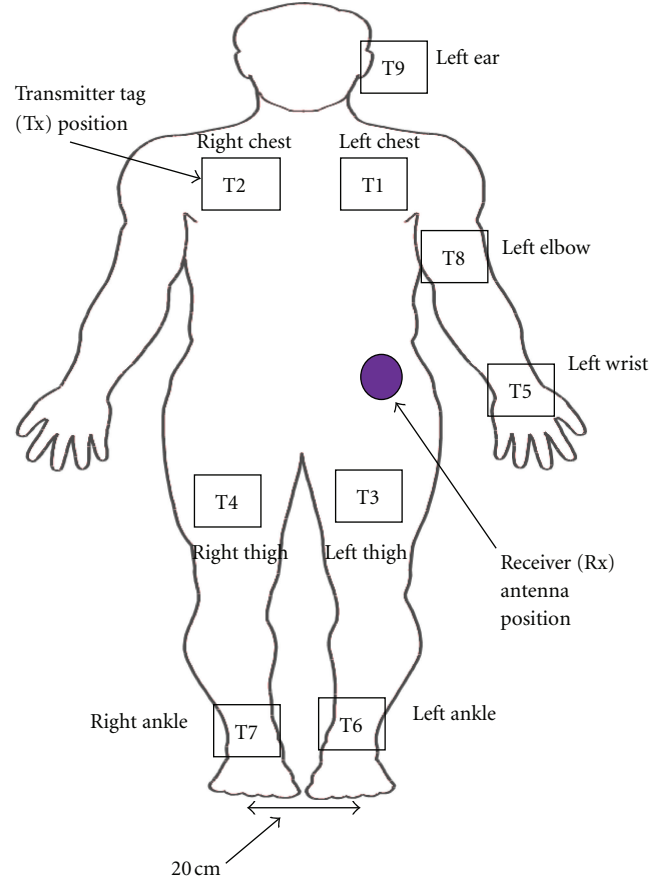


FIGURE 1: On-body measurement settings showing the receiver antenna is on the left waist, and nine transmitter tags are on different locations of the body (nine static and dynamic channels cases analysed).

plane) of the body (test subject) and the elevation plane (YZ) radiation pattern is directed towards off the body direction with a null in the main beam.

The measurement was first performed in the anechoic chamber to eliminate multipath reflections from surrounding environment and then repeated in the Body-Centric Wireless Sensor Lab at Queen Mary University of London to consider the effect of the indoor environment on the on-body radio propagation channels. Figure 4 shows the dimensions and geometry of the Body-Centric Wireless Sensor Lab. The total area of the lab is 45 m² which includes a meeting area, treadmill machine, workstations, and a hospital bed for healthcare applications. The measured Received Signal Strength Indicator (RSSI) level for each transmitter tag is recorded over the measurement duration of 60 seconds for each different location.

3. UWB On-Body Radio Channel Parameters

3.1. On-Body Radio Channel Characterisation. In this work, the path loss for nine different on-body channels was calculated from the measured RSSI for each transmitter tag. The cumulative distribution function (CDF) of the path loss

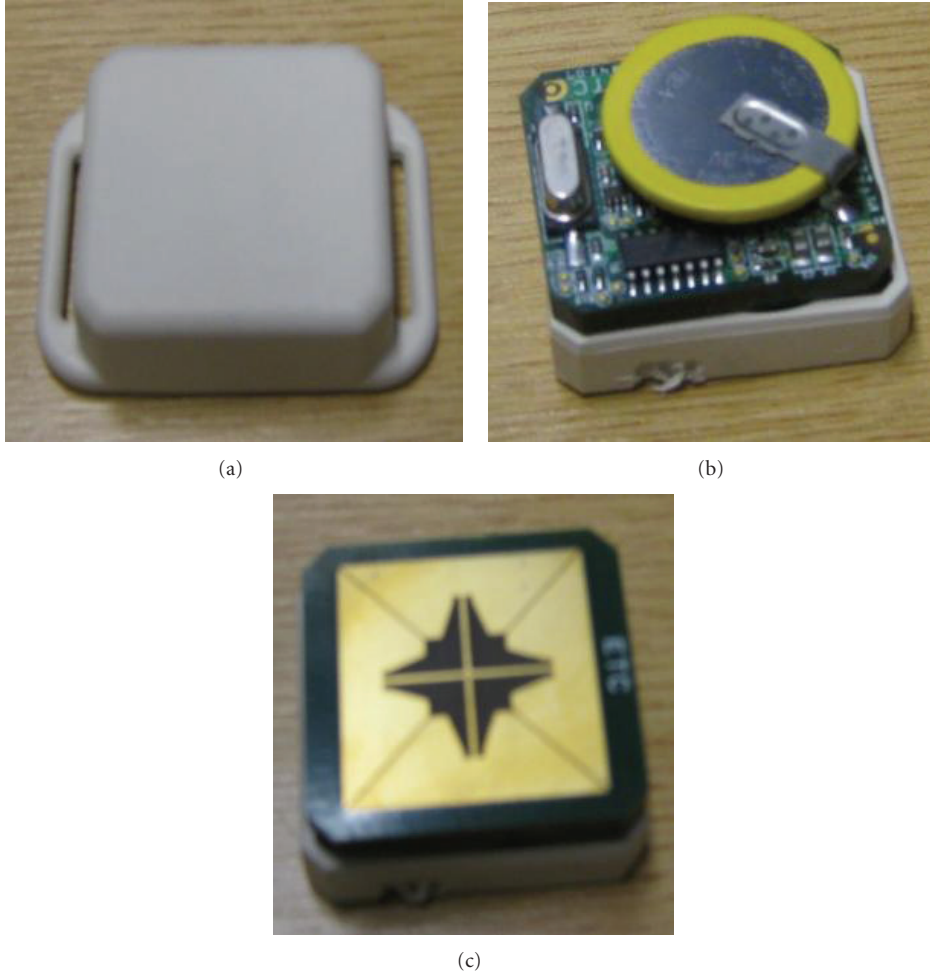


FIGURE 2: (a) UWB active transmitter tag encased inside the plastic housing, (b) tag without plastic housing and bottom view, and (c) top view of the tag showing the transmitter tag antenna.

variations both in the chamber and indoor environment for static and dynamic scenarios of nine different on-body radio channels is compared to well-known distributions as Normal, Lognormal, Nakagami, Rayleigh, Weibull, Gamma, and Rician adopting the Akaike criteria and on the basis of the tested results, lognormal distribution provides the best fits to these measured results (Figure 5). The Akaike information criteria is a method widely used to evaluate the goodness of a statistical fit [3, 22]. The second-order AIC (AIC_c) is defined as

$$AIC_c = -2 \ln(L) + 2k + \frac{2k(k+1)}{n-K-1}, \quad (1)$$

where L is the maximised likelihood, K is the number of parameters estimated for that distribution, and n is the number of samples of the experiment. The seven distributions mentioned above are all two parameter distributions ($K = 2$) except the Rayleigh ($K = 1$). In this measurement, the sample size is ($n = 60$).

The maximised log likelihood has been obtained from the MATLAB estimates. The Akaike information criteria can be used as a relative measure such that the model with the

lowest AIC means better statistical model and the criterion is used to classify models from the best to worse; to facilitate this process, the relative AIC is considered and results are normalized to the lowest value obtained

$$\Delta_i = AIC_c - \min(AIC_c). \quad (2)$$

A zero value indicates the best fitness. Comparison of different distributions adopting AKAI information criteria is shown in Table 1.

Figures 6 and 7 show a comparison of the measured average path loss (μ) and standard deviation (σ) of the fitted lognormal distribution that are applied to model the path loss variations for the nine on-body radio channels, for the static and walking scenarios, respectively.

In the chamber, for both standing and walking cases, the highest path loss is noticed for the receiver to left-ear link, while the lowest is the receiver to left-thigh link (Figure 6). For the reader to left-ear link the communication distance between the reader antenna and the transmitter tag is larger; in addition, due to the different orientation of the tag located on the left ear, non-line-of-sight (NLOS)

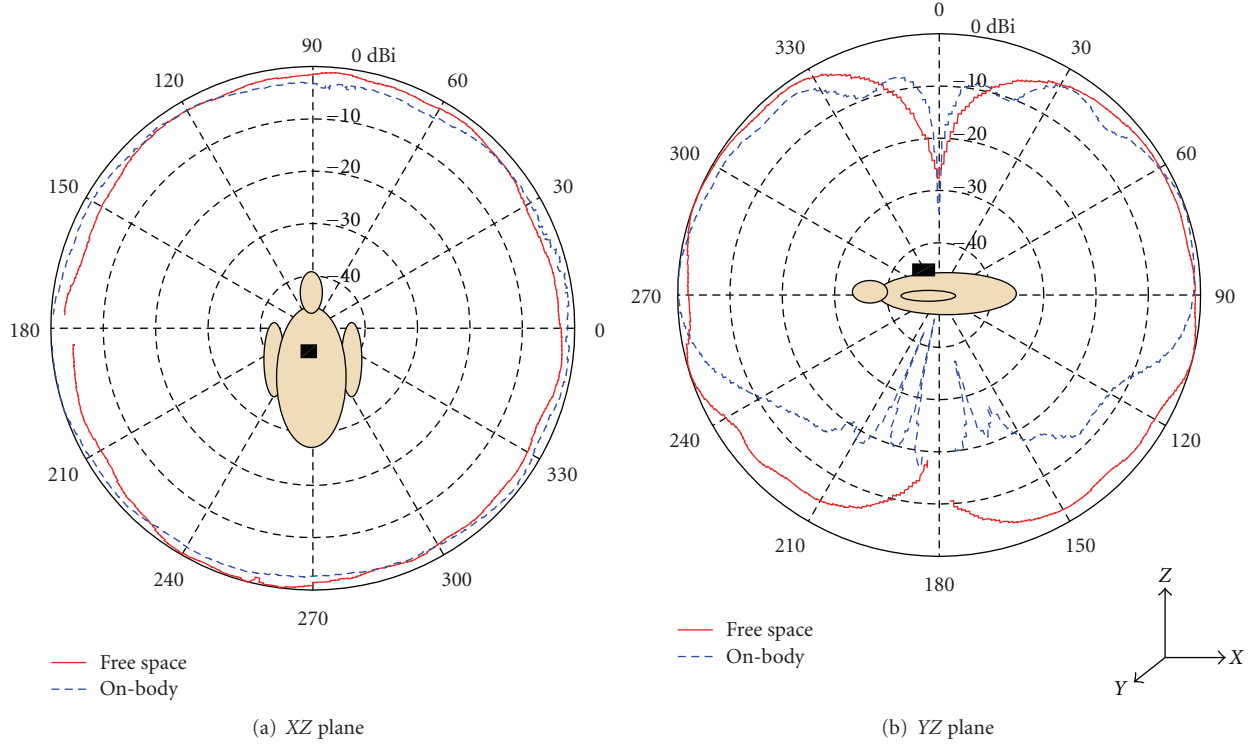


FIGURE 3: Measured free space and on-body radiation patterns at 6.6 GHz of the tags (a) XZ plane and (b) YZ plane.

TABLE 1: Comparison of different distributions adopting AKAI information criteria for nine on-body links measured in the chamber and indoor.

Tag position	Scenario	Normal	Lognormal	Gamma	Nakagami	Rayleigh	Rician	Weibull
L. chest	Chamber	0.286	0	0.080	0.176	324.69	0.276	11.12
	Indoor	0.892	0	0.282	0.282	313.88	0.884	16.74
R. chest	Chamber	0.010	0.078	0.040	0.016	323.22	0	5.268
	Indoor	0.398	0.390	0	0.190	296.31	0.390	12.68
L. thigh	Chamber	1.490	0	0.474	0.970	292.15	1.48	24.48
	Indoor	0.474	0	0.140	0.2980	310.63	0.470	16.40
R. thigh	Chamber	0.994	1.102	1.312	1.142	249.58	0.984	0
	Indoor	0.008	0.420	0.260	0.130	290.26	0	5.450
L. wrist	Chamber	0.530	0	0.120	0.290	203.40	0.520	8.530
	Indoor	0.022	0.160	0.060	0	188.38	0.012	1.700
L. ankle	Chamber	0.830	0	0.240	0.520	264.01	0.820	15.25
	Indoor	2.010	0	0.63	1.30	234.93	2.00	17.37
R. ankle	Chamber	0.490	0	0.110	0.260	220.40	0.480	9.160
	Indoor	0.290	0	0.056	0.142	155.34	0.280	3.780
L. elbow	Chamber	0.820	0	0.250	0.514	241.55	0.812	9.270
	Indoor	0.086	0.014	0	0.014	219.99	0.076	3.232
L. ear	Chamber	0.010	0	0.050	0.0220	288.55	0.096	7.952
	Indoor	0.706	0	0.210	0.4420	250.102	0.696	13.576

communications exist, which cause the highest path loss value for this channel. For this case (the receiver to left-ear link) due to different orientation of the tag located on the left ear, the polarization mismatch occurs between the tag and the reader which also causes the higher path loss value

for this link. For the left-thigh link, there are a clear line-of-sight (LOS) communication and the lowest communication distance between the reader and the transmitter tag.

In the indoor environment due to reflecting area and contributions of multipath reflection the right chest and

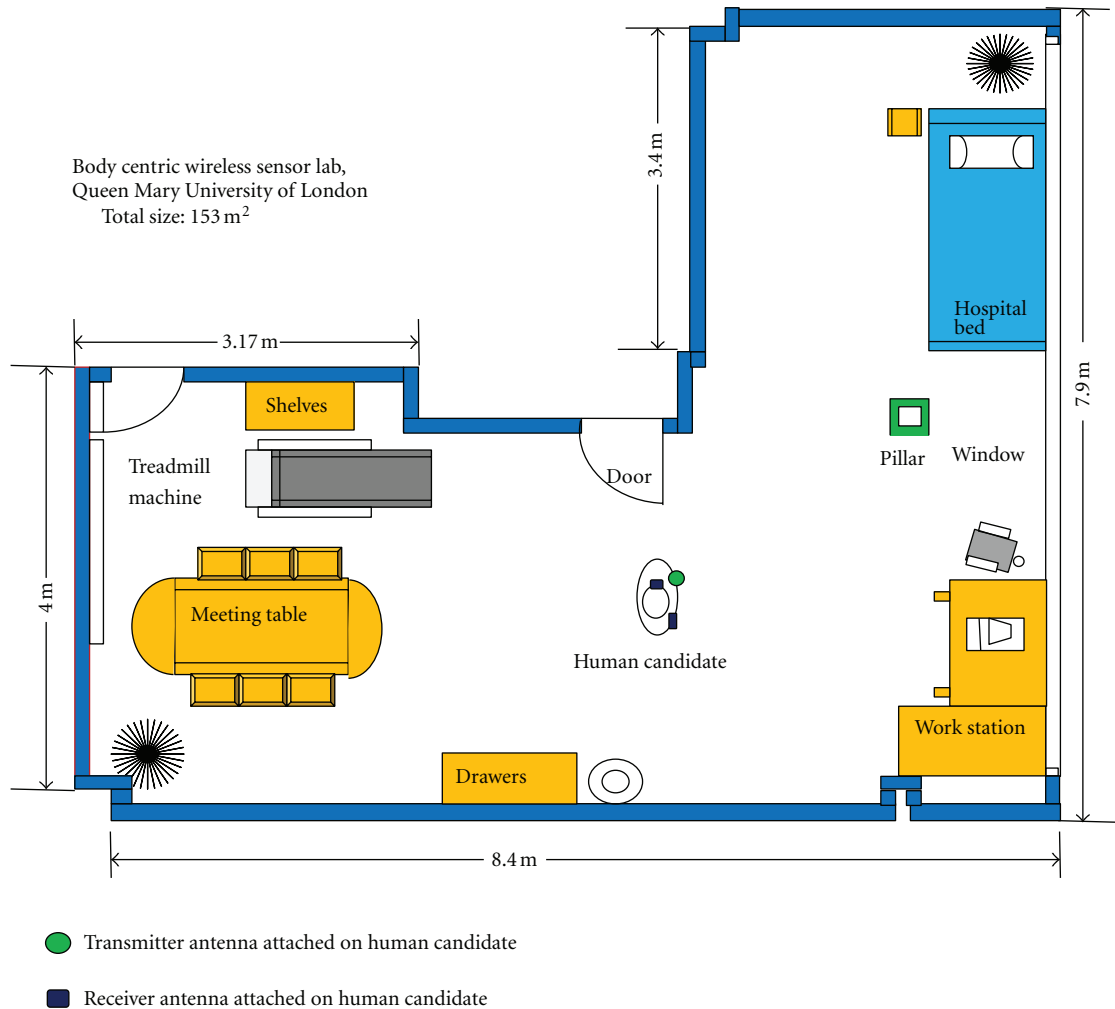


FIGURE 4: Dimensions and geometry of the Body-Centric Wireless Sensor Lab (housed within the Department of Electronic engineering, Queen Mary University of London, London, UK) where the indoor on-body radio propagation measurements for the presented work are performed.

left-ear (for static case) and right thigh and chest channels (for movement cases) experience the highest path loss value, while the left thigh channel experiences the lowest. Most of the on-body channels experience higher path loss value when measurements are made in the chamber, due to the nonreflecting environment. The average path loss of all nine channels in the chamber, for static and walking cases, is 81.44 dB and 80.68 dB, whereas 79.22 dB and 80.00 dB are found in the indoor environment, respectively.

The variation of the path loss for the nine different on-body channels is also compared for standing and walking cases, to study the trend of the changes of path loss for each channel in these two different scenarios. For the two different scenarios (i.e., standing and walking) a maximum of 8.23 dB and 6.88 dB variation of average path loss of a channel is noticed, which occurred for the left wrist channel both in indoor environment and chamber, respectively (Figure 6). During walking scenarios, the tag located on the wrist moves between LOS and NLOS communications scenarios, and the communication distance between the receiver and the

transmitter is also changed greatly, causing the path loss data to vary the most with respect to the standing case for this channel.

The highest standard deviation (σ) value for the dynamic case is noticed for the left wrist and right ankle channels, which are considered the least stable (data spread the most from the average path loss) channels, whereas the lowest is noticed for the left thigh and chest channels; these channels are considered the most stable (see Figure 7). Movement of the human body has the highest effect on the wrist and ankle channels and the least on chest and left thigh channels. In comparison to the chamber, the standard deviation value is found to be higher in the indoor environment due to the effects from the indoor reflecting multipath environment.

3.2. Path Loss versus Distance. Measurements were also performed in order to investigate the propagation along the front part of the whole body; see Figure 8. The same test subject was used for this case as was used for the previous case. The receiver antenna connected to the reader was placed

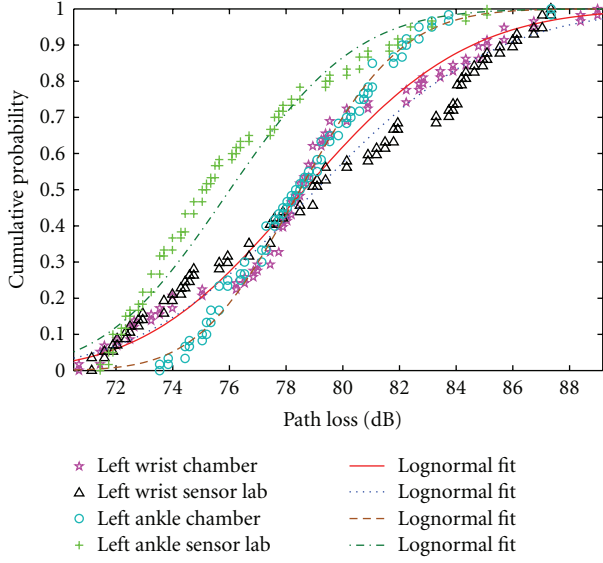


FIGURE 5: Cumulative distribution function of the left wrist and left ankle on-body radio channels when subject was walking measured in the chamber and in indoor environment.

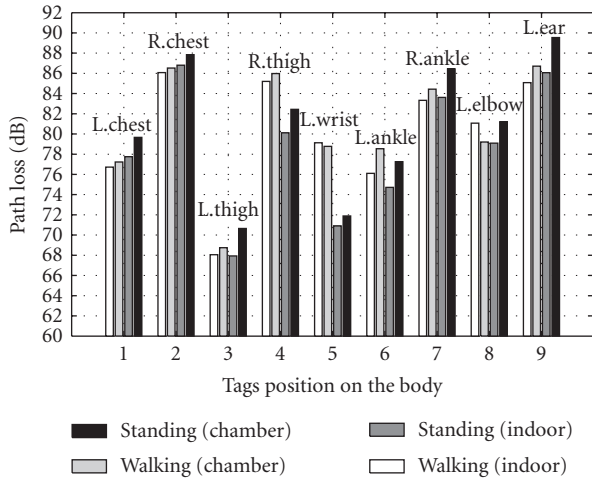


FIGURE 6: Comparison of average path loss of nine UWB on-body radio channels for standing and walking scenarios measured in the chamber and in indoor.

TABLE 2: Path loss parameters for whole body and different body parts.

Body parts	Channels					
	Chamber			Indoor		
	γ	$PL_{dB}(d_0)$	σ	γ	$PL_{dB}(d_0)$	σ
All body	2.53	68	6.01	2.24	67	5.11
Trunk	3.48	66	2.07	2.85	65.8	2.12
Arms	3.46	64	4.35	2.84	65.7	2.19
Legs	2.89	58.3	5.46	2.66	59	6.47

on the left waist, while the transmitter tags were placed on 34 different locations on the front part of the body (trunk,

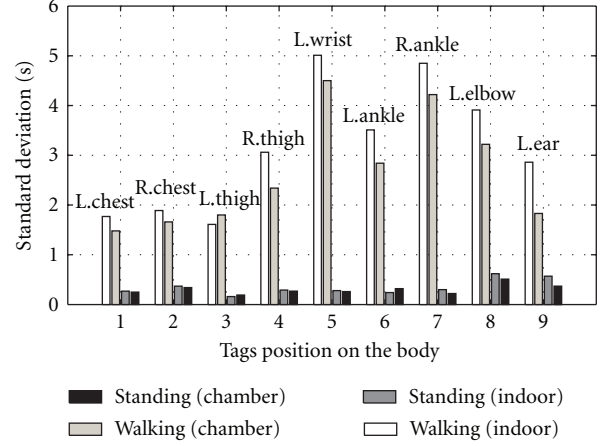


FIGURE 7: Comparison of standard deviation (σ) of nine different on-body radio channels for standing and walking scenarios measured in the chamber and indoor.

arms, legs, and head). In this case, during the measurement, the subject was standing still for 60 seconds, and the data were saved for that period of time for each transmitter tag location.

It is well known that the average received signal decreases logarithmically with distance (for both indoor and outdoor environments).

The path loss can be modeled as a linear function of the logarithmic distance between transmitter and receiver as explained in [23],

$$PL_{dB}(d) = PL_{dB}(d_0) + 10\gamma \log\left(\frac{d}{d_0}\right) + X_\sigma, \quad (3)$$

where d is the distance between transmitter and receiver, d_0 is a reference distance set in measurement (in this study it is set to 10 cm), $PL_{dB}(d_0)$ is the path loss value at the reference distance, and X_σ is the shadowing fading. The parameter γ is the path loss exponent that indicates the rate at which the path loss increases with distance. This parameter γ depends on the structure of environment (chamber or indoor) but also on the type of trajectory (trunk or legs).

A least-square fit technique was performed on the measured path loss for the 34 different transmitter locations, (Figure 8) to extract the path loss exponent. Figure 9 shows the measured value and modelled path loss for on-body channels versus logarithmic Tx-Rx separation distance. The path loss exponent was found to be 2.52 in the chamber and 2.24 in indoor (Table 2). In the indoor environment, the path loss exponent was found to be lower. When measurements are performed indoors, the reflections from surroundings scatters increase the received power, causing reduction in the path loss exponent. A reduction of 11.46% was noticed in indoor compared to the chamber.

X_σ is a zero mean, normal distributed statistical variable, and is introduced to consider the deviation of the measurements from the calculated average path loss. Figure 10 shows the deviation of measurements from the average path loss fitted to a normal distribution for both measurement cases.

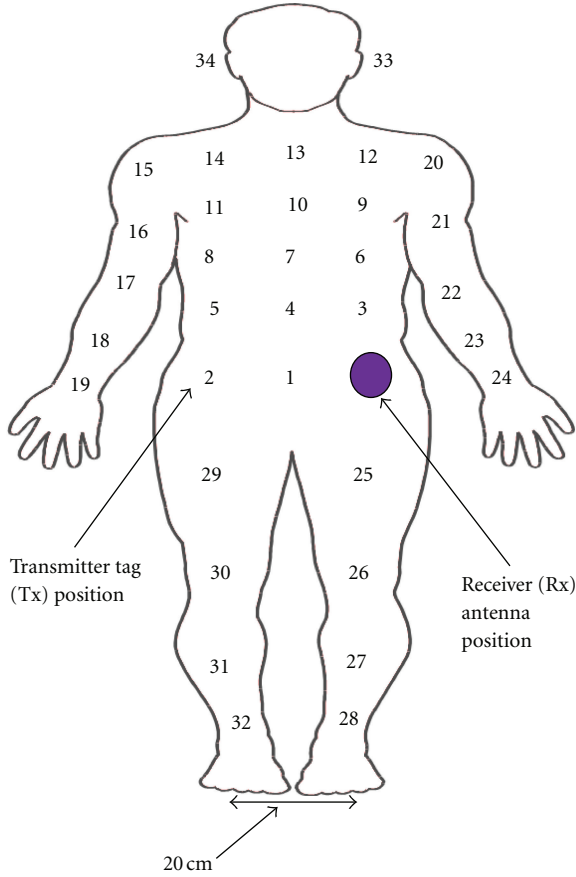


FIGURE 8: Location of the receiver antenna and positions of the 34 transmitter tags on the human subject.

In this case, the standard deviation of the normal distribution is found to be lower in the indoor environment.

The path loss exponent for propagation along different body parts, including trunk, arms, and legs, was extracted for both measurement cases and is summarised in Table 2. Different body parts show different path loss exponent values. The lowest value is found for the legs (2.89), whereas the highest was found for the trunk (3.48). For the trunk, the propagation mechanism is mainly creeping waves, which experience higher signal attenuation, resulting in higher exponent value [19]. In addition, in the trunk, there are higher diffraction and reflection from the human body parts that also increase the path loss exponent. For the arms case, the path loss exponent is higher, as some of the tags located on the arms support NLOS communications. For the legs, the propagation mechanism is mainly free space waves, guided waves and line-of-sight (LOS), which experience lower signal attenuation, resulting in lower path loss exponent. The lowest mean path loss at the reference distance is found for the leg parts in both measurement cases.

4. Second-Order Statistics for Different On-Body Links

The level crossing rate (LCR), average fade duration (AFD), and probability of fade (PF) are commonly applied in radio

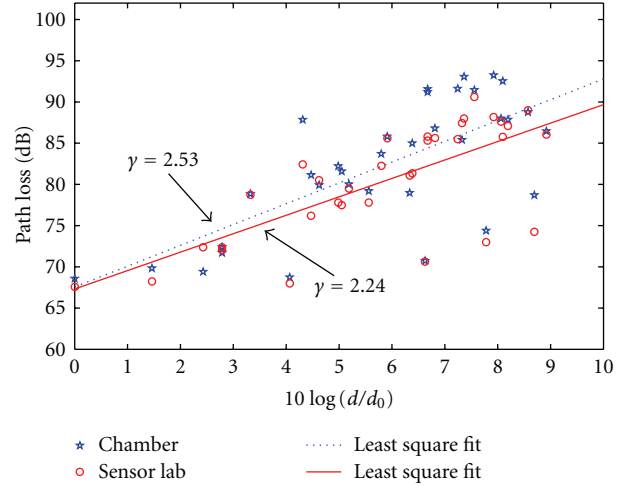


FIGURE 9: Measured and modelled path loss for on-body channel versus logarithmic Tx-Rx separation distance for UWB tags measured in the chamber and in indoor environments.

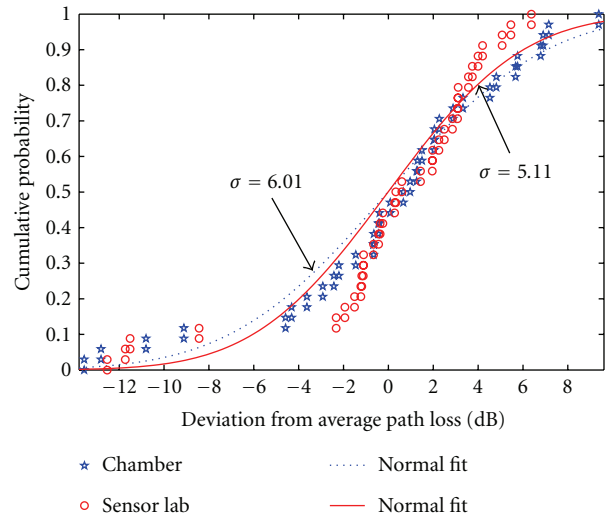


FIGURE 10: Deviation of the measurements from the average path loss fitted to normal distribution for both chamber and indoor measurement scenarios.

channel analysis to describe and investigate the severity of fading [24]. In this study, the second-order statistics are applied on the variation of RSSI due to the movement caused by walking over the measurement period (as shown in Figures 11(a) and 11(b)). Three different on-body radio links have been considered, namely, left waist to left wrist, left waist to left ankle, and left waist to left ear.

4.1. Fade Probability (FP). The probability of fade is the probability that a fading signal remains below the fade level or certain threshold level [24]. Figure 12 shows the comparison of fading probability for left wrist, left ankle, and left ear on-body channels for the walking case, measured in the chamber and in indoor. The fade levels shown in Figure 12 are the RSSI values for walking and normalized

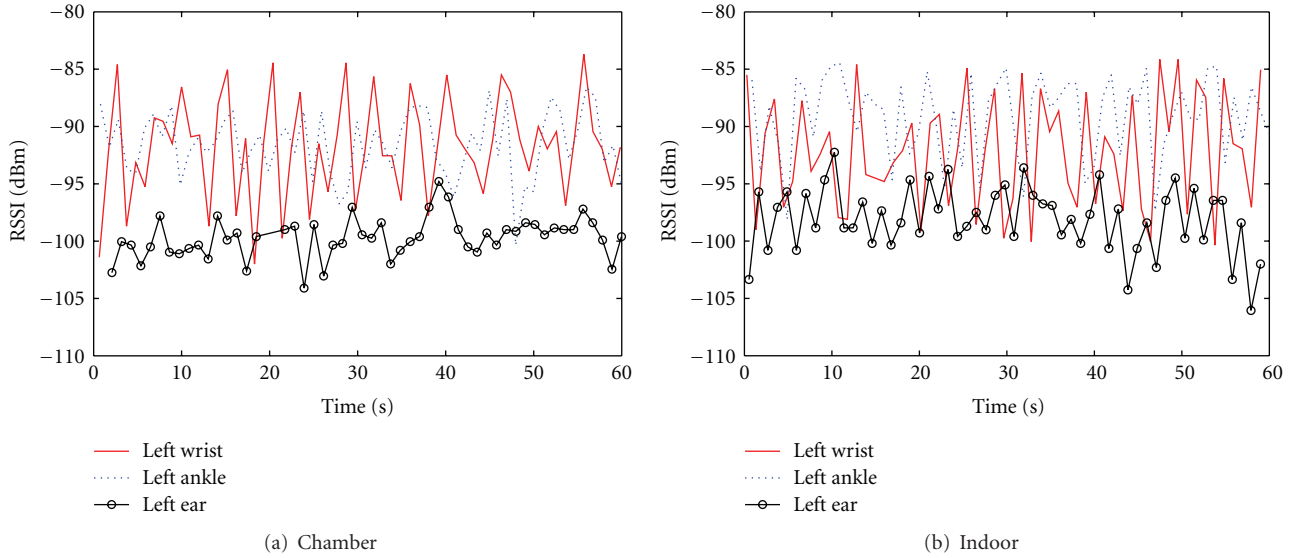


FIGURE 11: Comparison of RSSI level for three different on-body channels as left wrist, left ankle, and left ear when human subject was walking 5 steps ahead and 5 steps backward measured in the (a) chamber, (b) indoor.

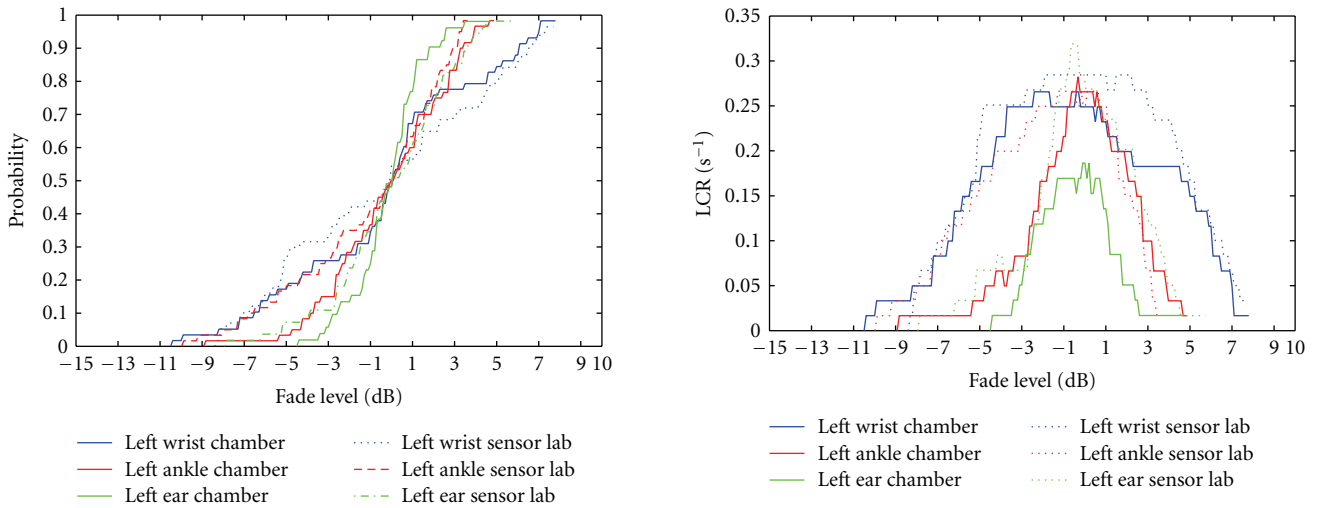


FIGURE 12: Comparison of fading probability (FP) for three different on-body channels as left wrist, left ankle, and left ear when subject was walking 5 steps ahead and back measured in the chamber and in indoor environment.

by the corresponding medians, and for the total fade level the increment of 0.01 dB is considered. The maximum fade level is noticed for the wrist and ankle channels, whereas the lowest is at the ear link. Comparing the two environments, the fade level is higher indoors for the left ear and ankle channels but lower for the wrist channel, which can be the effects of the multipath scattering environment in indoor. The fading probability at -3 dB fade level is found to be higher for all three different on-body links in indoor. At -3 dB fade depth, the fade probability of these three channels is between 7% and 27% in the chamber, while in indoor, it

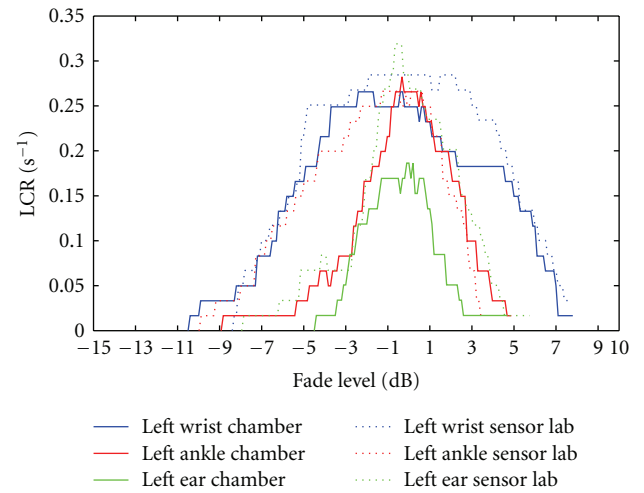


FIGURE 13: Comparison of level crossing rate (LCR) for three on-body channels as left wrist, left ankle, and left ear when subject was walking 5 steps ahead and back measured in the chamber and in indoor environment.

is between 12% and 33%. Out of these three channels, the fade probability at -3 dB is noticed higher for the left wrist channel, with a value of 33% measured in indoor, while the lowest is for the left ear channel, with a value of 7% measured in the chamber. Changing measurement environment does not change the fade probability for left ear link at -3 dB fade depth but which has higher effects for ankle and wrist channels.

4.2. *Level Crossing Rate (LCR)*. The level crossing rate (LCR) for a signal is the number of crossings of the signal with respect to a given threshold or specified fade level in the

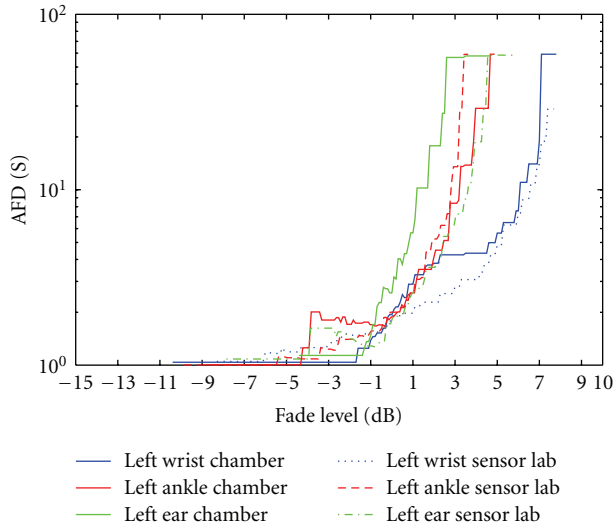


FIGURE 14: Comparison of average fade duration for three on-body channels as left wrist, left ankle, and left ear when subject was walking measured in the chamber and indoor environment.

positive going direction in a unit of time [24]. Figure 13 shows a comparison of the level crossing rate for the three considered links when the subject was walking. At a specified fade depth of -3 dB for the walking case, the LCR for these three on-body channels is mostly found to be higher in indoor. At -3 dB fade depth, the LCR in the chamber for these three channels is in the range of 0.05 s^{-1} – 0.25 s^{-1} while it is 0.07 s^{-1} – 28 s^{-1} in the indoor environments. Both in the chamber and indoor environments, the highest LCR value at -3 dB fade depth is noticed for wrist channel whereas the lowest is for ear channel. The LCR for the ankle link varies greatly in between the chamber and the indoor environments.

4.3. Average Fade Duration (AFD). The average fade duration is the average duration of time during which the fading signal remains below the specified fade level [24]. Figure 14 shows comparison of average fade duration for three different on-body channels, that is, as wrist, ankle, and ear measured in the chamber and in indoor for walking human subject. The AFDs characteristically increase with decreasing of fade depth.

For walking case, the left ankle channel has the highest AFD with the value of 1.9 seconds at the fade depth of -3 dB in the chamber. At -3 dB fade depth, the AFD is higher in the indoor environment for wrist and ear channels, while lower for the ankle. The AFD for all three channels is in the range of 1.1–1.9 seconds.

5. Conclusion

UWB on-body radio propagation channel measurements were performed using ultrawideband (UWB) wireless tags and reader in the chamber and indoor environments. Nine different UWB on-body radio channels were investigated for

static and movement scenarios. Results demonstrated that lognormal distribution provides the best fits for on-body propagation channels path loss model. In this study, left thigh link shows the lowest path loss, whereas the left ear and right chest show the highest. The study shows that due to different scenarios (i.e., standing and walking) an on-body link experiences up to 8.23 dB variations in path loss. Path loss exponent for individual body parts is extracted, where the lowest path loss exponent and the path loss at the reference distance are noticed for the legs part. Second-order channel parameters as (LCR), (FP), and (AFD) for three on-body links are investigated. Results and analysis showed that at a specified fade depth of -3 dB, the fade probability, level crossing rate, and average fade duration are found mostly higher in the indoor as compared to chamber.

Acknowledgments

The authors would like to thank John Dupuy and Sanjoy Mazumdar for their help and assistance with the measurements. Many thanks to Yuri Nechayev (University of Birmingham) for his fruitful discussions.

References

- [1] P. S. Hall and Y. Hao, *Antennas and Propagation For Body-Centric Wireless Communications*, Artech House, Norwood, Mass, USA, 2006.
- [2] J. Foerester, E. Green, S. Somayazulu, and D. Leeper, "Ultra-wideband for short- or medium-range wireless communications," *Intel Technology Journal*, vol. Q2, 2001.
- [3] A. Fort, C. Desset, P. de Doncker, P. Wambacq, and L. van Biesen, "An ultra-wideband body area propagation channel model—from statistics to implementation," *IEEE Transactions on Microwave Theory and Techniques*, vol. 54, no. 4, pp. 1820–1826, 2006.
- [4] Z. H. Hu, Y. I. Nechayev, P. S. Hall, C. C. Constantinou, and Y. Hao, "Measurements and statistical analysis of on-body channel fading at 2.45 GHz," *IEEE Antennas and Wireless Propagation Letters*, vol. 6, pp. 612–615, 2007.
- [5] A. Alomainy, Y. Hao, A. Owadally et al., "Statistical analysis and performance evaluation for on-body radio propagation with microstrip patch antennas," *IEEE Transactions on Antennas and Propagation*, vol. 55, no. 1, pp. 245–248, 2007.
- [6] S. L. Cotton, G. A. Conway, and W. G. Scanlon, "A time-domain approach to the analysis and modeling of on-body propagation characteristics using synchronized measurements at 2.45 GHz," *IEEE Transactions on Antennas and Propagation*, vol. 57, no. 4, pp. 943–955, 2009.
- [7] Y. I. Nechayev, Z. H. Hu, and P. S. Hall, "Short-term and long-term fading of on-body transmission channels at 2.45 GHz," in *Proceedings of the Loughborough Antennas and Propagation Conference (LAPC'09)*, pp. 657–660, Loughborough, UK, November 2009.
- [8] A. Fort, C. Desset, J. Ryckaert, P. de Doncker, L. van Biesen, and P. Wambacq, "Characterization of the ultra wideband body area propagation channel," in *Proceedings of the IEEE International Conference on Ultra-Wideband (ICU'05)*, pp. 22–27, September 2005.
- [9] A. Alomainy, Y. Hao, X. Hu, C. G. Parini, and P. S. Hall, "UWB on-body radio propagation and system modelling for wireless

- body-centric networks,” *IEE Proceedings: Communications*, vol. 153, no. 1, pp. 107–114, 2006.
- [10] Q. H. Abbasi, A. Sani, A. Alomainy, and Y. Hao, “On-body radio channel characterization and system-level modeling for multiband OFDM ultra-wideband body-centric wireless network,” *IEEE Transactions on Microwave Theory and Techniques*, vol. 58, no. 12, pp. 3485–3492, 2010.
- [11] Q. Wang and J. Wang, “Performance of on-body chest-to-waist UWB communication link,” *IEEE Microwave and Wireless Components Letters*, vol. 19, no. 2, pp. 119–121, 2009.
- [12] Q. Wang, T. Tayamachi, I. Kimura, and J. Wang, “An on-body channel model for UWB body area communications for various postures,” *IEEE Transactions on Antennas and Propagation*, vol. 57, no. 4, pp. 991–998, 2009.
- [13] A. Sani and Y. Hao, “Modeling of path loss for ultrawide band body-centric wireless communications,” in *Proceedings of the International Conference on Electromagnetics in Advanced Applications (ICEAA’09)*, pp. 998–1001, Turin, Italy, September 2009.
- [14] T. Zasowski, F. Althaus, M. Stager A, Wittneben, and G. Troster, “UWB for noninvasive wireless body area networks: channel measurements and results,” in *Proceedings of the IEEE Conference on Ultra Wideband Systems and Technologies*, pp. 285–289, November 2003.
- [15] A. Alomainy, Y. Hao, C. G. Parini, and P. S. Hall, “Comparison between two different antennas for UWB on-body propagation measurements,” *IEEE Antennas and Wireless Propagation Letters*, vol. 4, no. 1, pp. 31–34, 2005.
- [16] Q. H. Abbasi, A. Sani, A. Alomainy, and Y. Hao, “Arm movements effect on ultra wideband on-body propagation channels and radio systems,” in *Proceedings of the Loughborough Antennas and Propagation Conference (LAPC’09)*, pp. 261–264, Loughborough, UK, November 2009.
- [17] A. Alomainy, Q. H. Abbasi, A. Sani, and Y. Hao, “System-level modelling of optimal ultra wideband body-centric wireless network,” in *Proceedings of the Asia Pacific Microwave Conference 2009 (APMC’09)*, pp. 2188–2191, Singapore, December 2009.
- [18] A. Sani, G. Palikaras, A. Alomainy, and Y. Hao, “Time domain UWB radio channel characterisation for body-centric wireless communications in indoor environment,” in *Proceedings of the IET Seminar on Wideband and Ultrawideband Systems and Technologies: Evaluating Current Research and Development*, no. 12352, November 2008.
- [19] A. Sani, A. Alomainy, and Y. Hao, “Effect of the indoor environment on the UWB on-body radio propagation channel,” in *Proceedings of the 3rd European Conference on Antennas and Propagation (EuCAP’09)*, pp. 455–458, March 2009.
- [20] A. Alomainy, A. Sani, A. Rahman, J. G. Santas, and Y. Hao, “Transient characteristics of wearable antennas and radio propagation channels for ultrawideband body-centric wireless communications,” *IEEE Transactions on Antennas and Propagation*, vol. 57, no. 4, pp. 875–884, 2009.
- [21] Plus Asset Tag, Reader and SFF Antenna Datasheet/Time Domain, 2009, <http://www.timedomain.com/>.
- [22] K. P. Burnham and D. R. Anderson, *Model Selection and Multimodel Inference: A Practical Information-Theoretic Approach*, Springer, New York, NY, USA, 2002.
- [23] S. S. Gassezadeh, R. Jana, C. W. Rice, W. Turin, and V. Tarohk, “A statistical path loss model for in-home UWB channels,” in *IEEE Conference on Ultra Wideband Systems and Technologies*, pp. 59–64, 2002.
- [24] W. C. Y. Lee, *Mobile Communications Engineering*, Mc-Graw-Hill, New York, NY, USA, 1998.

Research Article

Analysis of Circular Polarization of Cylindrically Bent Microstrip Antennas

Tiiti Kellomäki

Department of Electronics, Tampere University of Technology, P.O. Box 692, 33101 Tampere, Finland

Correspondence should be addressed to Tiiti Kellomäki, tiiti.kellomaki@tut.fi

Received 13 March 2012; Accepted 18 May 2012

Academic Editor: Thomaskutty Mathew

Copyright © 2012 Tiiti Kellomäki. This is an open access article distributed under the Creative Commons Attribution License, which permits unrestricted use, distribution, and reproduction in any medium, provided the original work is properly cited.

When circularly polarized (CP) microstrip antennas are bent, the polarization becomes elliptical. We present a simple model that describes the phenomenon. The two linear modes present in a CP patch are modeled separately and added together to produce CP. Bending distorts the almost-spherical equiphase surface of a linearly polarized patch, which leads to phase imbalance in the far-field of a CP patch. The model predicts both the frequency shifting of the axial ratio band as well as the narrowing of the axial ratio beam. Uncontrolled bending is a problem associated especially with flexible textile antennas, and wearable antennas should therefore be designed somewhat conformal.

1. Introduction

Microstrip antenna, or the patch antenna, is a common choice for wearable antenna topology. The ground plane isolates the antenna from the human body, and as a result, the impedance and radiation characteristics are not significantly affected by the user. In addition, the ground plane reduces radiation into tissue. The low profile makes the antenna easy to integrate into clothing.

For an antenna to be truly wearable, it must be flexible, and its performance must not change significantly because of deformation. Design rules for conformal antennas can to some extent be used in wearable antenna design, but since the shape is subject to change, the antenna designer must ensure operation in many different use cases. Usually this means that the antenna should be designed to be broadband.

Circular polarization (CP) is commonly used in wearable off-body systems. For example, the GPS satellite positioning system uses CP. When a body-worn antenna is moving, its orientation is subject to change, resulting in polarization mismatch loss if linear polarization is used in the system. However, circular polarization requires careful shaping of the antenna, and is easily distorted when the wearable antenna conforms to the user's body.

Cylindrically bent linearly polarized (LP) patches have been thoroughly analyzed in the past. The input impedance

of a cylindrically bent LP patch was derived in [1, 2], and the equations for the radiated fields were also presented in [1]. The equations for the input impedance in [1, 2] do not predict any resonant frequency change for a thin patch because of the approximations used. However, the frequency shift has been reported in many measurements [3–5] as well as simulations [6]. To our knowledge, bent CP patch antennas have only been analyzed on a conical surface [7], but not cylindrical.

In this study we analyze the behavior of a bent CP patch. The radiated fields of the CP antenna are modeled by adding together the fields of two simulated LP patches, one in vertical and one in horizontal polarization. We assume that the circular polarization results from two orthogonal modes excited in a 90-degree phase shift. We then bend the two LP antennas that produce the two modes and model the bent CP antenna by adding the fields of the bent LP antennas.

Proper phasing in the farfield is the key to achieve circular polarization. The equiphase surface of an LP antenna is nearly spherical in the main lobe, and when the fields of two LP antennas are added together, good phasing (good CP) can be retained in a wide angular region. Bending distorts the equiphase surface, and as a result, the axial ratio in the sum field deteriorates.

By modeling the two modes with separate LP patches we aim to dissect the situation into easily understood parts. The

model gives insight into the phenomena associated with bent CP patches: change in input impedance, frequency shift of the axial ratio band, and distortion of the axial ratio beam.

This paper is structured as follows: Section 2 introduces the simulation models. The simulation results for the LP patches are briefly given in Section 3, and in Section 4 they are used to model the CP patch. Section 4.4 comments on the validity of the model, briefly comparing the results with measurements. The results are used to give guidelines for wearable antenna design in Section 5, and 6 concludes the work.

2. Model

Probe-fed LP rectangular patches were simulated using the finite integration technique implemented in the CST software [8]. The patches were 60 mm by 74 mm rectangles, on a 3 mm thick substrate with dielectric constant 2.3, and on a 148 mm square ground plane. The feed probe was inset 18 mm from the long edge of the patch and centered along that edge. The resonant frequencies of the two patches were almost equal, with the resonant frequency of the E-plane bent patch tuned slightly higher to achieve circular polarization. Figure 1 illustrates the structure.

These LP patches were bent in the E- and H-planes, conforming to a cylinder. The bending radii (30 mm to 300 mm, or 0.15 to 1.6 wavelengths) correspond to the curvatures found in the arms of children and adults and the torso. Bending in the E-plane (yz -plane) involves bending the y -directional current flow lines. The bending directions are illustrated in Figure 1.

The radiation patterns of the bent LP patches were simulated, and from the results, the phase centers were calculated. Phase center is the imaginary point from which the radiated spherical wavefront seems to emanate. A unique phase center does not generally exist, but an approximate location can be calculated using the field phase information in the main beam region.

Circular polarization was modeled as a phased sum of two orthogonal LP modes. The phase shifting was adjusted to achieve a 90-degree phase difference in the farfields of the flat antennas. The input impedance of the CP patch is the sum of the input impedances of the LP modes, and the farfield is the sum of the far fields of the LP patches, with the same phase shifting for both the impedance and the fields. The phasing was optimized for the flat antenna, and the same phasing was then used for all the different bending radii and all frequencies to simulate a phase-shifting network.

3. Results for LP Patches

The results for the impedance, detuning, far fields, and semi phase centers of the linearly polarized patches are summarized in this section.

3.1. Impedance and Resonance. Simulations of the LP patches show resonant frequency detuning in the E-plane bending but virtually none in the H-plane bending. E-plane bending

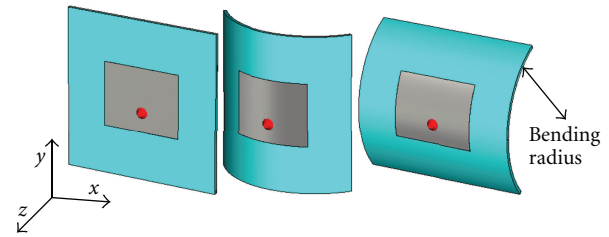


FIGURE 1: Simulated LP patch: flat, bent in H-plane, and in E-plane. Dot marks the feed probe position. H-plane is the xz -plane and E-plane the yz -plane. The main lobe is in the $\theta = 0$ (z -axis) direction.

increases the input impedance, whereas H-plane bending decreases it. Figure 2 shows the simulated impedances and resonant frequencies. The simulated effects of bending the LP antennas are listed in Table 1.

Previous measurements have shown that E-plane bending increases the resonant frequency of an LP patch antenna [3, 4]. The theoretical examination in [1] does not predict the detuning because of the approximations used. According to [1], the input impedance will decrease in H-plane bending and increase in E-plane bending (this was shown for substrate thickness 1.59 mm and dielectric constant 2.32).

The change in impedance magnitude as well as the detuning was repeated in our simulations. Detuning was minor when the E-plane bending radius was very large (100 mm or more, which corresponds to 0.5 wavelengths) and, between radii of 30 and 80 mm a decrease of 1 mm in the radius introduced about 0.9 MHz detuning. Table 2 lists the simulated resonant frequencies of the linearly polarized patch bent in the E-plane.

3.2. Far Field and Semi Phase Centers. The phase center of an antenna is the imaginary point from which the spherical wavefront seems to emanate. Such a point is not guaranteed to exist, but an approximate location can be calculated, for example, in the main beam region. Moreover, separate semi phase centers can be calculated in the principal planes, considering only the field phase in that plane: in the E-plane, the circular (two-dimensional) wavefront seems to emanate from the point P_E . The H-plane semi phase center is denoted by P_H . If the points P_E and P_H coincide, the wavefront is spherical; if not, the phase front is astigmatic, as illustrated in Figure 3.

For the purposes of this study, we calculated the E- and H-plane semi phase centers using the phase information of the pattern in a 60-degree aperture cone around the main lobe. This is approximately the 3dB beam.

The phase center of a flat LP patch lies approximately in the plane of the patch, at the center. The semi phase centers coincide, and the wavefront is approximately spherical.

Bending moves the semi phase centers apart from each other and makes the phase front astigmatic. Figure 4 shows that especially in the E-plane bending the semi phase center locations depend heavily on the bending radius. Figure 5 illustrates the locations of the two semi phase centers in two bending cases.

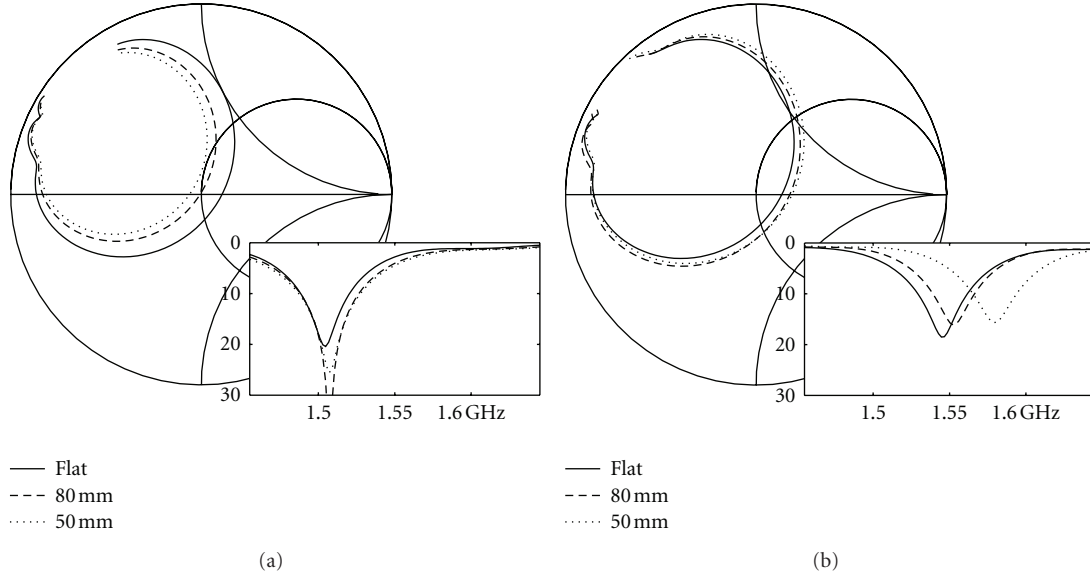


FIGURE 2: Simulated input reflection coefficient of the bent LP patch. (a): bending in the H-plane, (b): E-plane bending. Insets show return loss in dB.

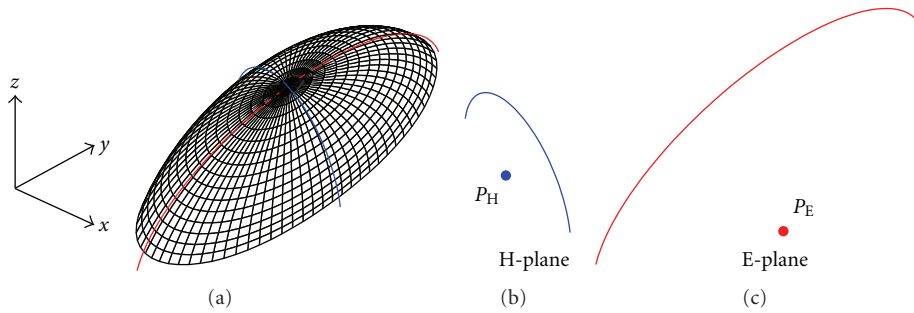


FIGURE 3: How to calculate the semi phase centers from the equiphase surface. (a): The astigmatic (not spherical) wave front. (b): The circular wavefront in the H-plane (xz -plane) emanates from P_H . (c): In the E-plane (yz -plane), P_E is the center of the circular wavefront. P_H and P_E do not coincide.

TABLE 1: Simulated effects of bending LP patch antennas. “+” indicates a strong effect.

	H-plane bending	E-plane bending
Input impedance	Decreases	Increases
Resonant frequency	Constant	Increases
H-plane beamwidth	Increases+	Constant
E-plane beamwidth	Increases	Increases
H-plane phase center	Backward	Forward
E-plane phase center	Backward	Backward+
Cross-polarization	No change	No change

If the antenna is bent in the H-plane, both semi phase centers move behind the antenna, P_H slightly more than the P_E . Bending in the E-plane, on the other hand, moves P_E backward and P_H to the front. Thus the equiphase surface is badly distorted, resembling a donut (flat in the H-plane) rather than a sphere. This is illustrated in Figure 6.

TABLE 2: Detuning caused by bending in the E-plane.

Radius (in wavelengths)	Flat	300 mm (1.6λ)	80 mm (0.4λ)	40 mm (0.2λ)
Resonant frequency	1545 MHz	1548 MHz	1552 MHz	1586 MHz

Within the frequency range of interest the semi phase center locations for each bending radius are quite stable, moving 5 mm at the maximum over the band. Note that the interesting frequency band is narrow, since we are mainly interested in the band where the axial ratio of the modeled CP patch is small.

The semi phase centers also move in the xy -plane (in the plane of the patch), but this movement is much less pronounced than the movement along the z -axis (forward and backward). Gain, cross-polarization level, and efficiency are not significantly affected by bending.

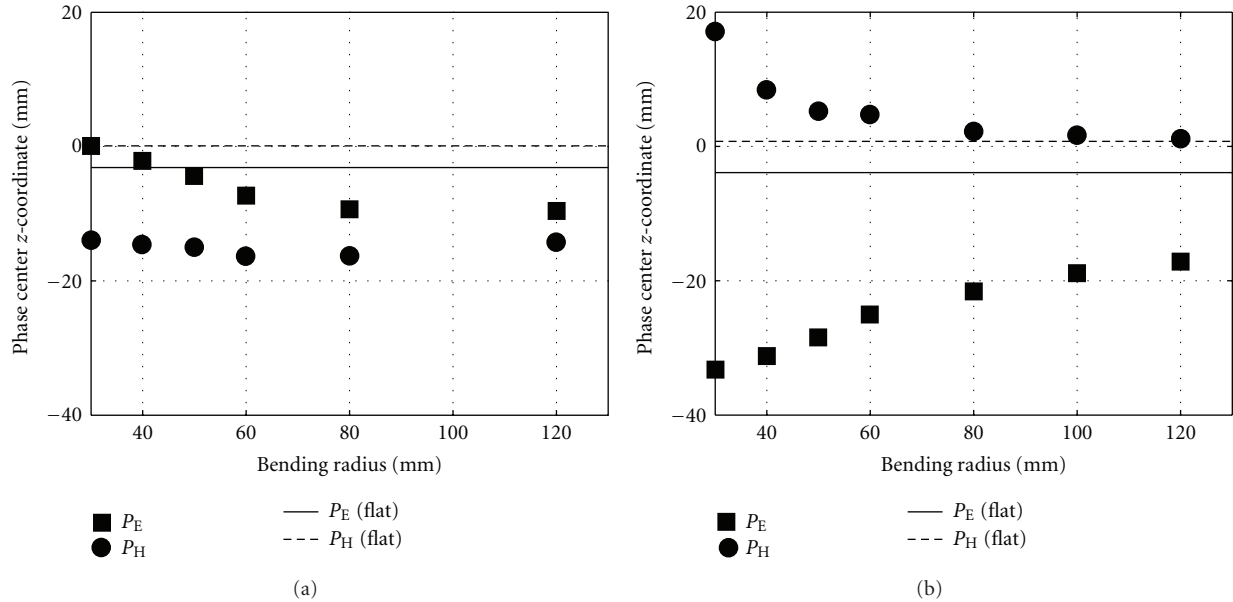


FIGURE 4: Semi phase center z -coordinates. (a): H-plane bending, (b): E-plane bending. Horizontal lines show the location of semi phase centers as calculated for a very large bending radius.

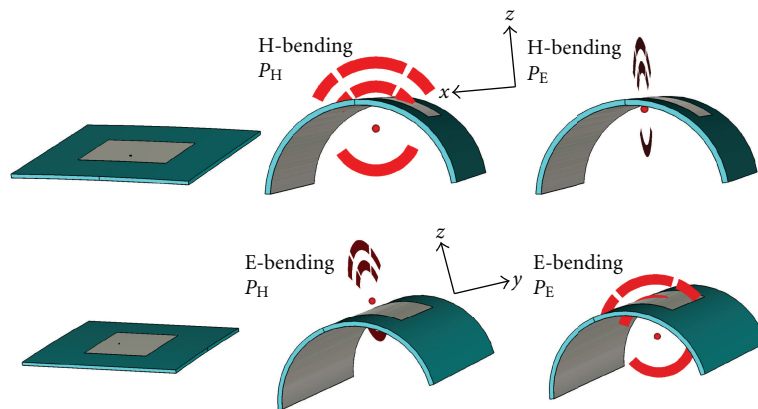


FIGURE 5: Movement of phase centers due to bending. The bending radius is 50 mm. In the case of a flat antenna, both semi phase centers are in the plane of the patch. Left column shows the flat antenna viewed from the same direction.

4. The CP Patch according to the Model

The results for the bent linearly polarized patch antenna will now be used to explain the behavior of a bent circularly polarized antenna. To generate circular polarization, the two linear modes are added together with such a phasing that a 90-degree phase shift is achieved at the target frequency. The same phase shifting is used in the input impedance.

The changes in the input impedance due to bending are discussed first. Then the simulated changes in the far field phase are used to explain the axial ratio in the main lobe (z -axis, $\theta = 0$). We will see that the axial ratio band shifts in frequency. Finally, the angular region of good axial ratio is examined with the help of the semi phase centers P_E and P_H . Using the semi phase centers instead of the full far field phase information allows us to squeeze the information into one

number (semi phase center location) and, hence, to explain the situation intuitively.

4.1. Impedance and Matching. The impedance of a CP patch was modeled as a phased sum of the impedances of the LP patches. Plotted on the Smith chart (Figure 7), the reflection coefficient shows a loop commonly seen in the case of CP antennas. In the reflection coefficient of the bent CP patch (modeled as the sum of the impedances of two bent LP patches), the loop is seen to shift counterclockwise.

In the return loss of the CP patch (inset of Figure 7) we see how the wide notch with two minima turns into two separate notches when the antenna is bent. This might lead to the conclusion that circular polarization is lost, but actually we will still find an axial ratio minimum between the two

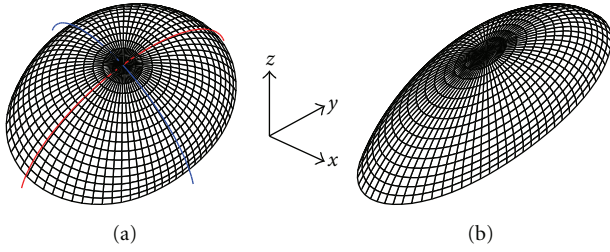


FIGURE 6: Equipphase surfaces. (a): The spherical equipphase surface of the flat patch antenna. Semi phase centers coincide. (b): The astigmatic equipphase surface of the E-plane bent patch antenna. P_H (in the xz -plane) is in front of the antenna, but P_E (in the yz -plane) is behind it. The astigmatism is exaggerated for clarity.

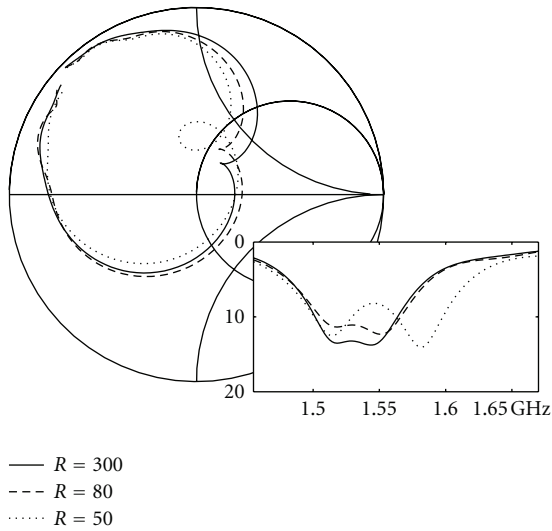


FIGURE 7: Input reflection coefficient of the CP patch modeled as a phased sum of the input impedances of two LP patches. Inset shows return loss in dB.

notches. It is noted that the frequency difference between the pits in the sum (Figure 7) is smaller than the difference of the pits of two modes modeled separately (Figure 2).

4.2. Axial Ratio versus Frequency Using Far Field Phase. To produce a perfect circular polarization, an antenna must radiate two LP modes of equal amplitude in a 90-degree phase shift. Table 3 lists the limits to produce circular polarization with an axial ratio less than 3 dB. From the table it is evident that phase shifting is more critical than amplitude balance.

From the simulation data, we have extracted the field phase differences of the bent LP patches at $\theta = 0$ (z -axis). One of the LP antennas is now bent in its E-plane and the other in its H-plane. The phase differences at the original center frequency are tabulated in Table 4.

When the antenna is bent, the phase difference between the fields at the center frequency grows too large. To reduce the phase difference, we must introduce extra phase difference between the impedances. A larger impedance phase

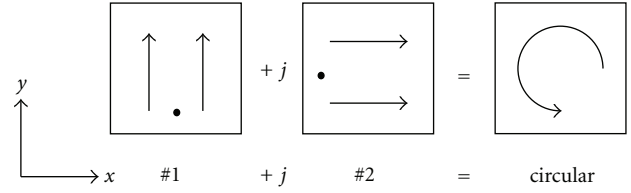


FIGURE 8: CP antenna with two current modes. #1 produces vertical polarization, #2 horizontal, and phased sum yields circular polarization.

TABLE 3: Limits for circular polarization with axial ratio <3 dB.

Amplitude difference	0 dB	1 dB	2 dB	3 dB
Phase difference (min)	70°	72°	75°	90°
Phase difference (max)	110°	108°	105°	90°

TABLE 4: Simulated field phase difference near $\theta = 0$, observed at a constant frequency.

Radius (mm)	flat	80	50	30
Phase difference	90°	96°	112°	124°

difference can be found at a higher frequency. We will now observe a good axial ratio at this higher frequency, provided that the amplitude difference is small enough (see Table 3).

4.3. Axial Ratio in the Main Beam Region Using Semi Phase Centers. Even at the frequency where we have a good axial ratio on the z -axis, the shape of the angular region with AR < 3 dB (“AR beam”) is distorted. For the flat antenna, the AR beam is of the same shape as the main lobe, but bending makes the AR beam narrower.

Consider a CP antenna with two radiating current modes: mode no. 1 producing vertical polarization and mode no. 2 horizontal, as illustrated in Figure 8. The main lobe points toward the z -axis. The horizontal plane is the H-plane for mode no. 1 but the E-plane for no. 2, and vice versa for the vertical plane. When mode no. 2 is set to lead by 90°, the resulting polarization is right-handed circular. We will assume a 90° phase difference on the z -axis.

Now if this antenna is bent, the semi phase centers of the modes #1 and #2 will move apart, especially along the z -axis, as was seen in Figure 4. This results in additional phase shift, which is listed in Table 5. Note that the table only lists values for one bending radius, and as seen from Figure 4, the semi phase center location depends heavily on the bending radius. The amplitudes of the modes do not change much, unless detuning causes a significant mismatch loss.

Bending deforms the angular region of good axial ratio: when one mode produces an equipphase surface nearly spherical and the other of a donut shape, it is clear that the phase difference between the fields will vary even in the main beam region. Sufficiently far away from the z -axis we can use the semi phase centers to give information about the field phase difference.

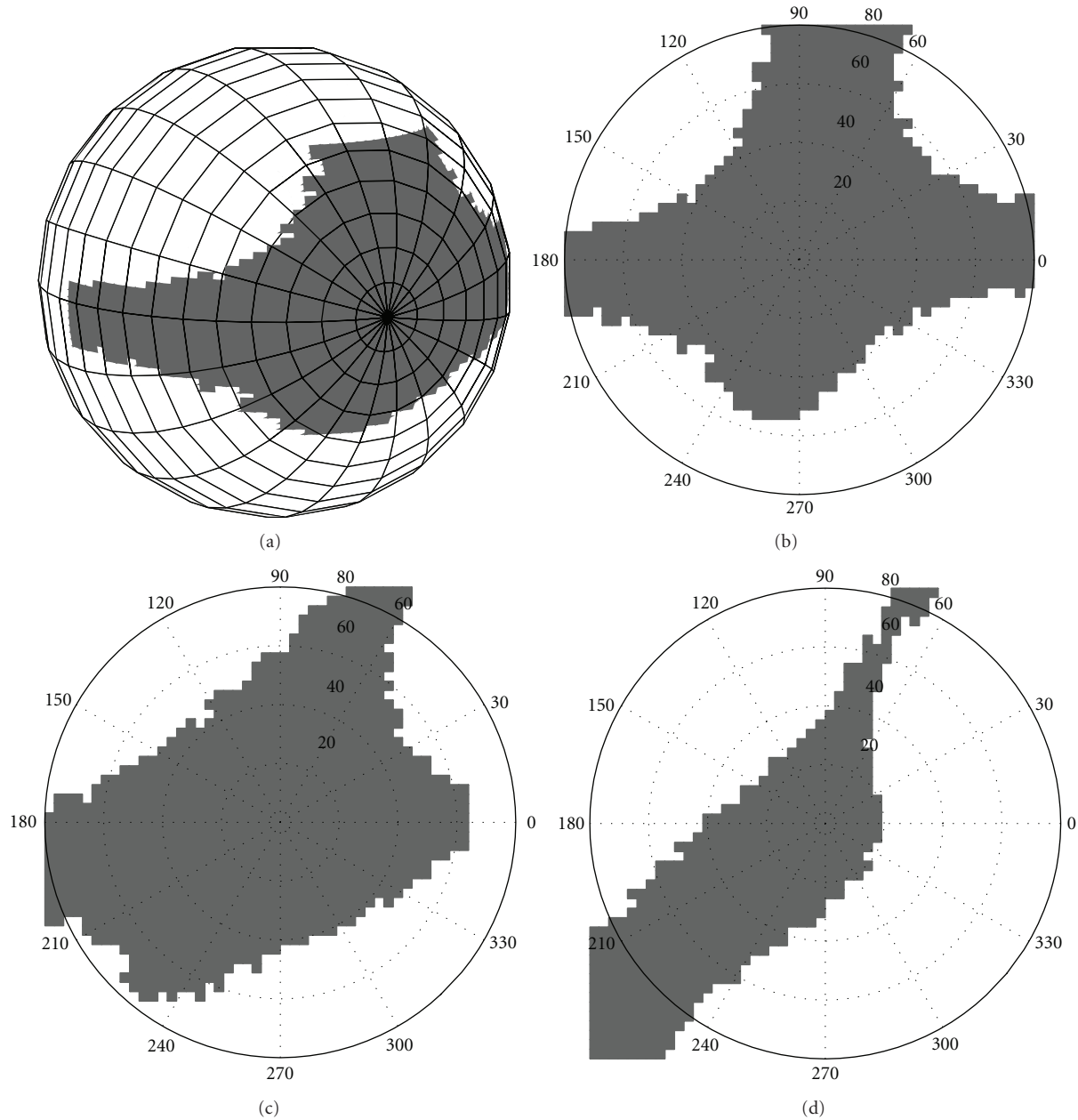


FIGURE 9: The 3dB axial ratio area (shaded) in the main beam. Radial coordinate is $\theta = 0 \cdots 80^\circ$, polar ϕ . Main lobe direction is $\theta = 0$. The figures are best understood as a map of the polar region of the spherical coordinate system. (a): almost flat antenna, shown both 3D and in (θ, ϕ) coordinates. (b): 80 mm and 60 mm radii.

TABLE 5: Semi phase center z -coordinates when the antenna is bent on a 80 mm radius. The semi phase centers lie approximately at $z = 0$ when the antenna is flat. Distance between semi phase centers is also expressed as phase shifting (degrees) at 1515 MHz.

	Horizontal bending		Vertical bending	
	Semi p. c. in horiz. plane	Semi p. c. in vert. plane	Semi p. c. in horiz. plane	Semi p. c. in vert. plane
Mode 1	-16.2 mm	-9.3 mm	+2.8 mm	-21.9 mm
Mode 2	-21.9 mm	+2.8 mm	-9.3 mm	-16.2 mm
Difference	+5.7 mm	-12.1 mm	+12.1 mm	-5.7 mm
Difference in phase	+10.4°	-22.0°	+22.0°	-10.4°

In the horizontal bending (the first two columns in Table 5), the semi phase centers of the modes #1 and #2 are 18 mm apart from each other, which corresponds to a phase difference of 32° , as compared to the case where the semi phase centers coincide. We assumed that the field phase difference at $\theta = 0$ (z -axis) is exactly 90° , but away from the z -axis we now have a phase difference of $90^\circ - 22^\circ = 68^\circ$ in the vertical plane and $90^\circ + 10^\circ = 100^\circ$ in the horizontal plane. This means that circular polarization cannot exist in the vertical plane, and the AR beam is deformed. If the antenna was bent in the vertical plane the situation would be the opposite: no circular polarization in the horizontal plane.

Figure 9 illustrates the axial ratio of a flat and a bent antenna at the same frequency. We see good axial ratio in the $\phi = 0$ plane (horizontal plane in the previous example) even with the bending radius 80 mm. Bending more makes the axial ratio beam very narrow.

The deformation of the AR beam occurs in addition to the frequency shift of the good axial ratio.

4.4. Comments on the Model. The model is suited to describe a dual-feed CP antenna with a 90-degree hybrid splitter between the two ports. We can then assume a good isolation between the ports, and the modes can be treated independently.

The shift of the axial ratio band has been reported, for example, in [9] as well as in our measurements and simulations. In our measurements we validated the model by measuring the input impedance and radiation pattern of a single-feed detached-corner CP patch antenna [10] bent in four planes spaced 45° . A shift of the axial ratio band towards lower frequencies has also been reported, but this phenomenon cannot be explained using this model. However, this very simple model already predicts the shift in impedance and axial ratio and sheds light on the reasons why this happens.

5. Implications to Wearable Antenna Design

During the research it became clear that wearable antennas should be designed somewhat conformal: for example, if the antenna is to be placed on the sleeve of a jacket, it should be designed on a cylindrical surface. A small deviation in the cylinder radius is less harmful than a change from flat to cylindrical shape. This is seen especially in Figure 4: slight bending changes the equiphase surface from spherical to astigmatic.

Particularly CP antennas should be designed as conformal as possible, close to their expected bending radius, and bending those antennas should be limited to relatively large radii only (e.g., minimum 100 mm at 1.5 GHz). CP antennas should therefore be placed on the back rather than on the sleeve of a coat.

Bending makes the main lobe wider and hence lowers the gain. This phenomenon is not harmful in wearable antennas, where all-round coverage is often sought for. The cross-polarization in linearly polarized antennas does not change significantly. We can say that linearly polarized antennas

are, in general, more robust with regard to bending than circularly polarized antennas.

If possible, bending any patch antenna, be it circularly, linearly, or dual polarized, should be limited to the H-plane only. Bending in the E-plane results in a resonant frequency shift which can lead to a strong mismatch loss. This is the most severe effect that bending has on microstrip antennas.

6. Conclusion

A simplified model of a bent CP patch antenna has been described. In the model, the two orthogonal polarization components that together form the circular polarization were treated separately. In simulations, one component was bent in its E-plane and the other in its H-plane. Circular polarization was then modeled by adding these modes together with a proper phase shifting.

The model predicts the frequency shift of the axial ratio band and explains why the angular region with good axial ratio is deformed. Also the change in the input impedance was predicted.

Finally, some guidelines for wearable antenna design and placement were given.

Acknowledgment

This work was supported by the Finnish Cultural Foundation, Pirkanmaa Regional Fund.

References

- [1] K.-M. Luk, K. F. Lee, and J. S. Dahele, "Analysis of the cylindrical-rectangular patch antenna," *IEEE Transactions on Antennas and Propagation*, vol. 37, no. 2, pp. 143–147, 1989.
- [2] G. Amendola, "Analysis of the rectangular patch antenna printed on elliptic-cylindrical substrates," *IEE Proceedings: Microwaves, Antennas and Propagation*, vol. 147, no. 3, pp. 187–193, 2000.
- [3] P. Salonen and Y. Rahmat-Samii, "Wearable antennas: Advances in design, characterization, and application," in *Antennas and Propagation for Body-Centric Wireless Communications*, P. S. Hall and Y. Hao, Eds., pp. 151–188, Artech House, 2006.
- [4] Q. Bai and R. Langley, "Textile antenna bending and crumpling," in *Proceedings of the 4th European Conference on Antennas and Propagation, (EuCAP '10)*, Barcelona, Spain, April 2010.
- [5] T. Kellomäki, J. Heikkinen, and M. Kivikoski, "Effects of bending GPS antennas," in *Proceedings of the Asia-Pacific Microwave Conference (APMC '06)*, pp. 1597–1600, Yokohama, Japan, December 2006.
- [6] Q. Bai and R. Langley, "Wearable EBG antenna bending," in *Proceedings of the 3rd European Conference on Antennas and Propagation, (EuCAP 09)*, pp. 182–185, Berlin, Germany, March 2009.
- [7] R. Shavit, "Circular polarization microstrip antenna on a conical surface," *IEEE Transactions on Antennas and Propagation*, vol. 45, no. 7, pp. 1086–1092, 1997.
- [8] "Computer Simulation Technology," Darmstadt, Germany <http://www.cst.com/>.

- [9] E. Kaivanto, J. Lilja, M. Berg, E. Salonen, and P. Salonen, "Circularly polarized textile antenna for personal satellite communication," in *Proceedings of the 4th European Conference on Antennas and Propagation, (EuCAP '10)*, Barcelona, Spain, April 2010.
- [10] J. Heikkinen, T. Laine-Ma, A. Ruhanen, and M. Kivikoski, "Flexible antennas for GPS reception," in *Proceedings of the European Conference on Antennas and Propagation: (EuCAP '06)*, Nice, France, November 2006.